Evaluation of Properties of Triply Periodic Minimal Surface Structures Using ANSYS

by

Faisal Raja

A Dissertation Presented in Partial Fulfillment
of the Requirement for the Degree
Master of Science

Approved April 2019 by the
Graduate Supervisory Committee:

Patick Phelan, Chair
Dhruv Bhate
Konrad Rykaczewski

ARIZONA STATE UNIVERSITY

May 2019

ABSTRACT

The advancements in additive manufacturing have made it possible to bring life to designs that would otherwise exist only on paper. An excellent example of such designs are the Triply Periodic Minimal Surface (TPMS) structures like Schwarz D, Schwarz P, Gyroid, etc. These structures are self-sustaining, i.e. they require minimal supports or no supports at all when 3D printed. These structures exist in stable form in nature, like butterfly wings are made of Gyroids. Automotive and aerospace industry have a growing demand for strong and light structures, which can be solved using TPMS models. In this research we will try and understand some of the properties of these Triply Periodic Minimal Surface (TPMS) structures and see how they perform in comparison to the conventional models. The research was concentrated on the mechanical, thermal and fluid flow properties of the Schwarz D, Gyroid and Spherical Gyroid Triply Periodic Minimal Surface (TPMS) models in particular, other Triply Periodic Minimal Surface (TPMS) models were not considered. A detailed finite element analysis was performed on the mechanical and thermal properties using ANSYS 19.2 and the flow properties were analyzed using ANSYS Fluent under different conditions.

ACKNOWLEDGMENTS

I would like to extend my profound gratitude to Dr. Patrick Phelan, Dr. Drhruv Bhate and Dr. Konrad Rykaczewski for being part of my thesis committee. I would specially like to thank Dr. Phelan for his guidance and providing me this opportunity to work on this project.

Special thanks to Dr. Huei-Ping Huang for his advice and insights regarding the CFD analysis done in this research. I would also like to thank my peers Vishakha Singal, Rajagopalan Ramesh, Aravind Kommineni, and Benjamin Obeng for their constant support and contributions to this research. They guided me and motivated me to always perform better and achieve more.

TABLE OF CONTENTS

Page

CHAPTER Page

LIST OF TABLES

Table Page

Table Page

LIST OF FIGURES

Figure Page

Figure Page

Figure Page

Figure Page

Figure Page

Figure Page

Figure Page

Figure Page

Figure Page

Figure Page

Chapter 1

INTRODUCTION

There has been a growing demand for light and strong structures in the automotive and aerospace industries [6, 13, 16, 28, 36]. Researchers are developing architectured cellular structures to solve this problem [5, 10, 20, 31]. Nature has many structures which are light, strong, highly porous and have high inter-connectivity [3, 6, 15, 32]. This research focuses on analyzing the Triply Periodic Minimal Surface (TPMS) models. The mechanical, thermal and fluid flow properties of these models will be analyzed using finite element software packages like ANSYS and compared to the conventional models.

1.1 Triply Periodic Minimal Surface Structures

A minimal surface is a surface in R^3 (three dimensions) which has a mean curvature (H) of zero at all points, where mean curvature is given by H = (k1+k2)/2 and k1 and k2 are the principal curvatures [11]. When a surface is free of self-intersections, i.e. their edges never cross each other, it is said to be embedded. A minimal surface, periodic in three independent directions and may be built up by its symmetry elements is called triply periodic minimal surface (TPMS). There are many TPMS that exist in natural and man-made state, but there are just a few which are free of any self-interaction. In 1865, Hermann Schwarz identified five infinite periodic minimal surfaces free of self-interaction, in terms of the Weierstrass parameterization for minimal surfaces [9, 29]. Which Cohen named Schwarz D (Figure 1.1a) , because of the symmetric similarity to that of a diamond crystal and Schwarz P (primitive surface) (Figure 1.1b), because of the symmetric similarity to that of a primitive cubic lattice.

These minimal surface coordinates are represented by Enneper – Weierstrass parameterization as follows [14]: -

$$x = e^{i\theta} Re \int \omega_0 \omega (1 - \tau^2) R(\tau) d\tau \tag{1.1a}$$

$$y = e^{i\theta} Re \int \omega_0 \omega i (1 + \tau^2) R(\tau) d\tau \tag{1.1b}$$

$$z = e^{i\theta} Re \int \omega_0 \omega 2\tau R(\tau) d\tau \tag{1.1c}$$

Where $i^2 = -1$ and $\tau = \tau_\mathrm{a} + i\tau_\mathrm{b}$, is associated with $\mathrm{R}(\tau)$ (the Weierstrass function) a unique surface $\mathrm{r}(\tau_\mathrm{a}, \tau_\mathrm{b})$ which is guaranteed to be minimal and θ is the Bonnet angle. The coordinates are expressed as real parts (Re) of the contour integrals, integrated from a fixed point ω_0 to ω (a variable point). Which can be simplified to the following forms.

Schwarz D

$$\sin x \sin y \sin z + \sin x \cos y \cos z + \cos x \cos y \cos z + \cos x \cos y \sin z = 0 \tag{1.2}$$

Schwarz P

$$\cos x + \cos y + \cos z = 0 \tag{1.3}$$

In 1970 Schoen, while studying the Schwarz identified TPMS, further identified 12 more surfaces free of self-intersections, but only one was an explicit solution to the 1760's Lagrange 'Plateau's Problem', this surface was named gyroid or G [29]. A simplified form of the gyroid representation as given by Wohlgemuth et al.[34] is as follows.

$$F_{SG}(x, y, z) = t \tag{1.4a}$$

$$\sin\left(\frac{2\pi}{L}x\right)\cos\left(\frac{2\pi}{L}y\right) + \sin\left(\frac{2\pi}{L}y\right)\cos\left(\frac{2\pi}{L}z\right) + \sin\left(\frac{2\pi}{L}z\right)\cos\left(\frac{2\pi}{L}x\right) = t \tag{1.4b}$$

Where L is the cell length and t=0 for minimal surface gyroid. In this study the following alternative equation will be used.

$$\sin x \cos y + \sin y \cos z + \sin z \cos x = 0 \tag{1.5}$$

The above equations are further modified to develop the minimal surface geometries as required

1.2 Fused Deposition Modelling

Rapid prototyping was the first-form of creating a three-dimensional object layer by layer, it was developed in the 1980's to help realize what engineers had in mind. One of the earlier additive manufacturing (AM) processes allowed the creation of parts, not just models. Rapid prototyping has many major advantages over conventional manufacturing techniques such as - reduction in time and cost of product development, possibility to create almost any shape, that would be otherwise difficult to machine [7].

It can be seen in Fig 1.2 rapid prototyping creates models faster and saves a lot of time, making it possible to test more models. The various additive manufacturing processes are shown in Figure 1.3.

Fused deposition modelling (Figure 1.4) is an additive manufacturing process in which a thin plastic filament is fed to a printer, where a nozzle head melts and extrudes the filament in a thickness of 0.25mm typically [35]. Materials only available as filaments can be printed using the FDM printers and are mostly plastic in nature. Most commonly available materials are poly carbonate (PC), acrylonitrile butadiene styrene (ABS), PC-ABS blends, poly carbonate carbon fiber (PCCF), polylactic acid (PLA). A commercially available FDM printer can be seen in Figure 1.5

The main advantages of this additive manufacturing process are the machines are less expensive than other conventional manufacturing machines, the materials are cheap and easily available, no chemical resins are used and hence no curing is required, the spare parts like nozzle heads can be easily replaced and the support is of the same material as the main model - all this resulting in a cost effective process

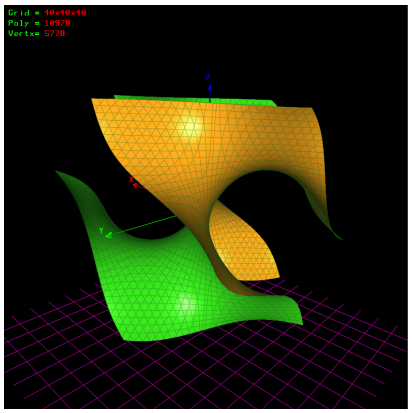

(a)

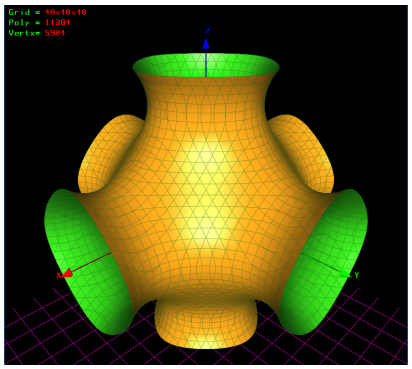

(b)

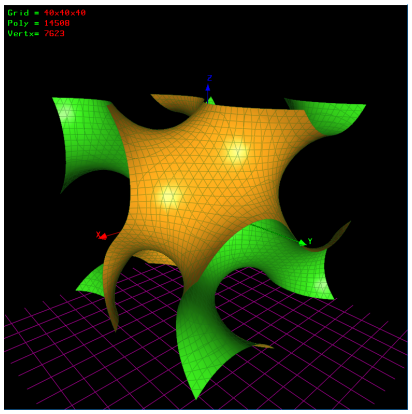

(c)

Figure 1.1: Triply Periodic Minimal Surface Unit Cells as Modelled in MathMod (a) - Schwarz D, (b) - Schwarz P, (c) - Gyroid.

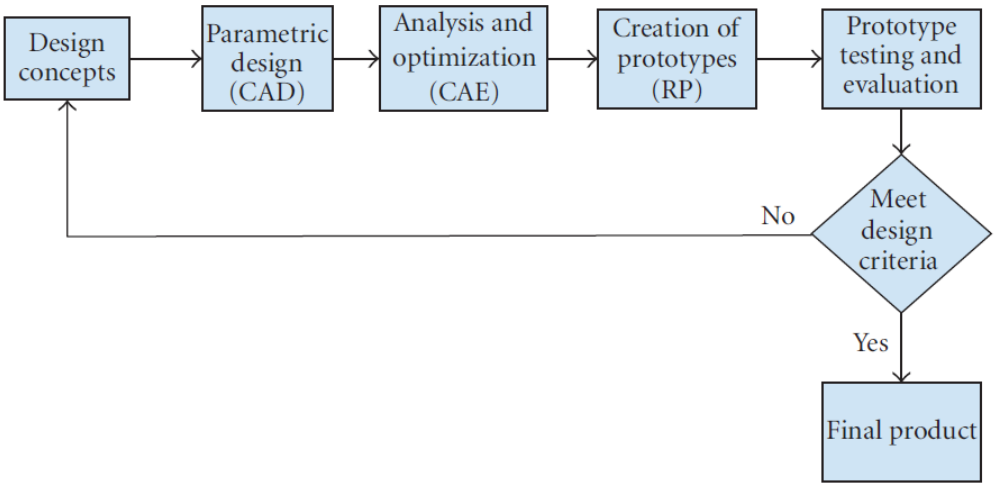

Figure 1.2: Product Development Cycle [25].

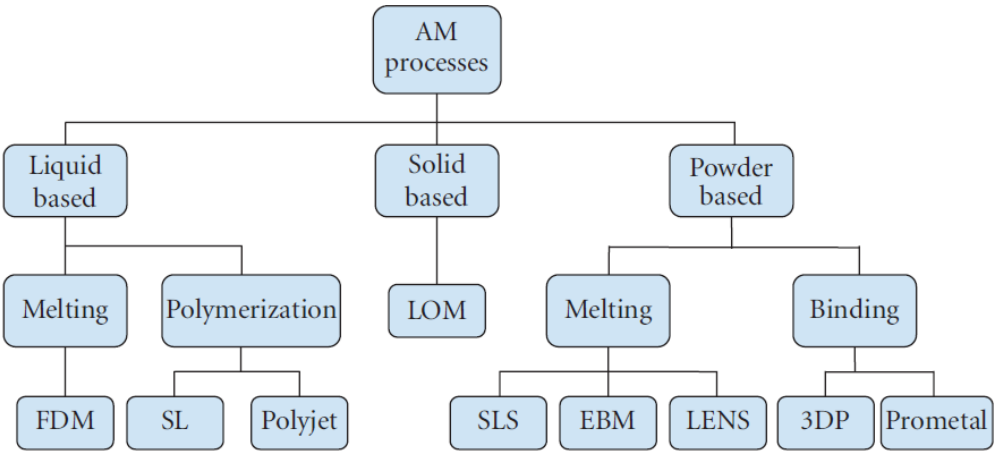

Figure 1.3: Additive Manufacturing Processes [21, 35].

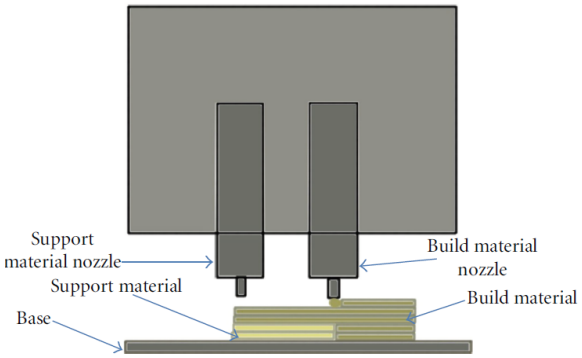

Figure 1.4: Fused Deposition Modelling [35].

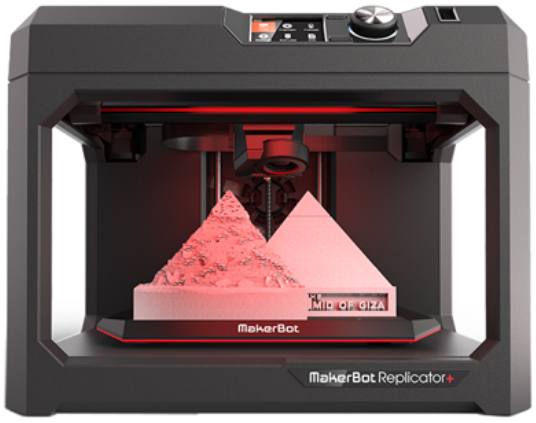

Figure 1.5: FDM Printer by MakerBot Industries - MakerBot Replicator+ [1].

[8, 25].

The disadvantages are, if the model is complex, supports may be needed which maybe difficult to remove depending on the complexity of the model. The resolution on the z axis is low, obtaining a smooth finish requires a finishing process, hence increasing the time and printing big and complex models takes a lot of time, sometimes even taking days to complete.

1.3 Finite Element Method

Various engineering problems are generally described in terms of differential equations based on continuum mechanics models. Solving these differential equations under complex initial and boundary conditions can be very difficult, especially if the model is very complex and understanding the conditions are even harder. In such cases, numerical methods are adopted to obtain approximate solutions for differential equations.The most popular numerical method used to solve such differential equations is finite element method [30].

Finite element method (FEM) is the most used tool for analyzing complex engineering structures, which would be impossible to examine using conventional numerical methods. In FEM, a complex structure is broken down into a finite number of smaller pieces (elements), the governing equations are formulated, based on the principles of conservation of mass, conservation of momentum, conservation of energy,etc. These elements are then assembled to model the behaviour of the structure [24].

The breaking down of the complex structure into finite number of smaller pieces (elements) is called discretization or meshing.The types of elements commonly used in FEM are shown in Figure 1.6. A unique number identifies each element and node in the domain.The shape function (Figure 1.7) decides the type of element and the number of elements that is to be used for the meshing. Also, the shape functions should be reliable, i.e. as the mesh becomes more refined, the approximate solution must converge to the exact solution monotonically as shown in Figure 1.8. A monotonically convergent solution is preferred over an oscillatory convergence, because its more reliable and decreases the chances of error with a refined mesh [23].

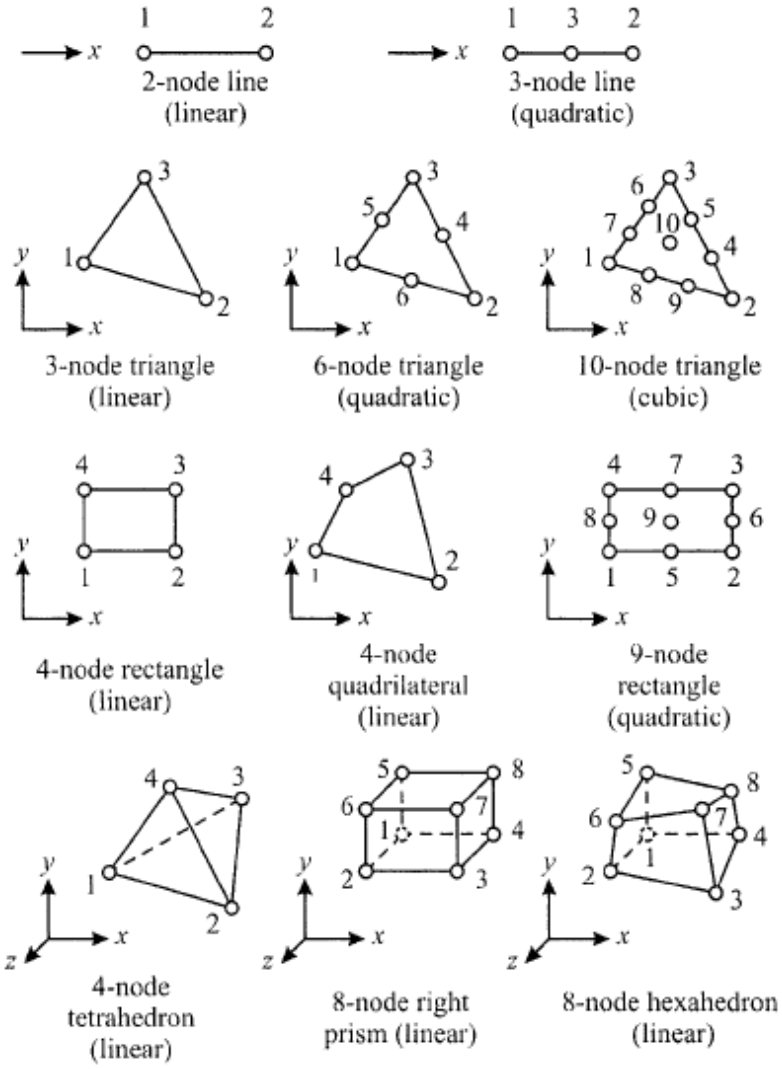

Figure 1.6: Types of Elements Commonly Used in One-, Two-, and Three-Dimensional Finite Elements [23].

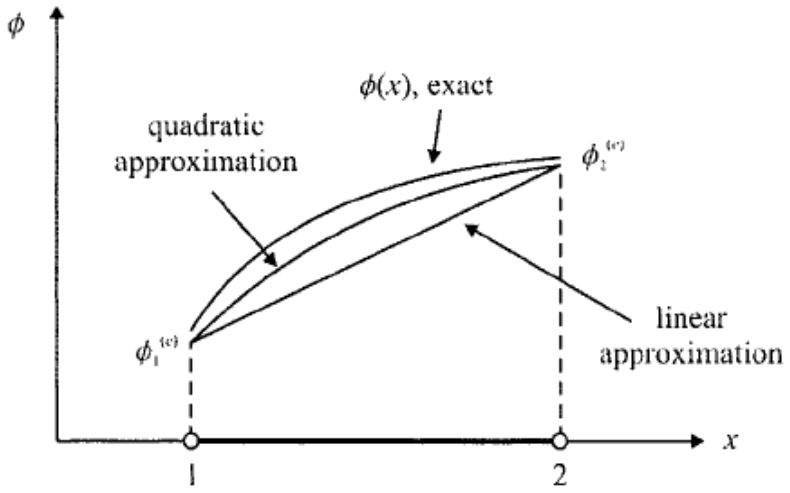

Figure 1.7: Shape Functions [23].

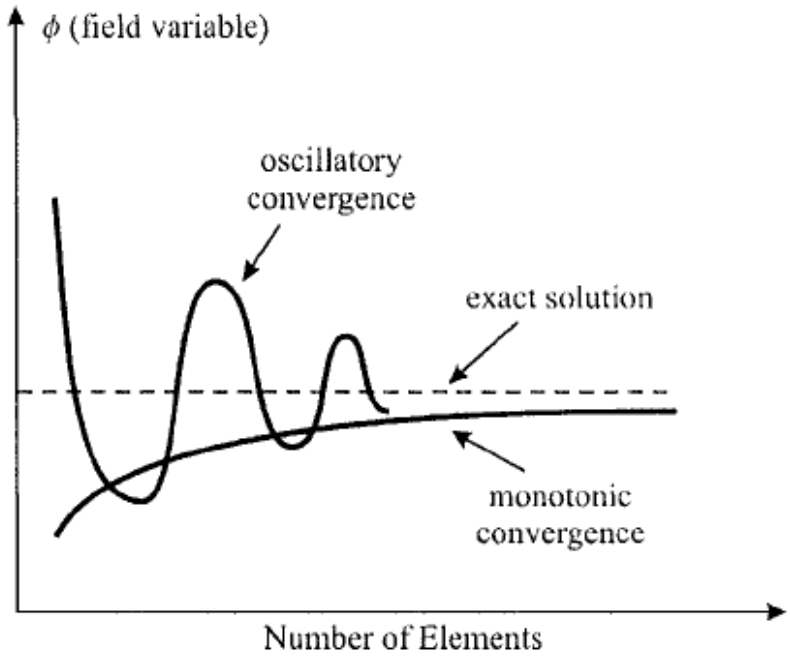

Figure 1.8: Oscillatory and Monotonic Convergence of Shape Functions [23].

1.4 Computational Fluid Dynamics

There are three methods by which approximations to partial differential equations are developed these are (i) Finite Element method, (ii) Finite Difference method, (iii) Finite Volume method. Computational fluid dynamics (CFD) utilizes Finite Difference and Finite Volume methods, making it easier to solve fluid dynamics problems. Fluid dynamics is a scientific method which involves governing equations in integral and partial differential form, solving such equations numerically is an onerous task and requires deep knowledge of differential calculus. Sometimes the problems can be further complicated by having multiple boundary and initial conditions. Solving the same problems computationally using tools like CFD, a solution can be obtained quicker, with less percentage of error.

The integral form of the fluid-flow equations are obtained directly by applying the fundamental physical principles to a finite control volume. The partial differential equations of the governing equations can be obtained by some manipulation of the integral forms. Integral or partial differential form of governing equations obtained from finite control volume fixed in space (Figure 1.9a), are called conservation form of governing equation. Equations obtained from the finite control volume model where the finite control volume is assumed to be moving with the fluid (Figure 1.9b) are called nonconservation form of the governing equations [4].

Partial differential forms of the governing equations can be obtained directly by applying the fundamental principles to the infinitesimal fluid element itself. Also, the partial differential equations obtained from the fluid element fixed in space Figure 1.10a are called the conservation form of the governing equations and the equations obtained from the moving fluid element Figure 1.10b are called the non-conservation form of the equations [4].

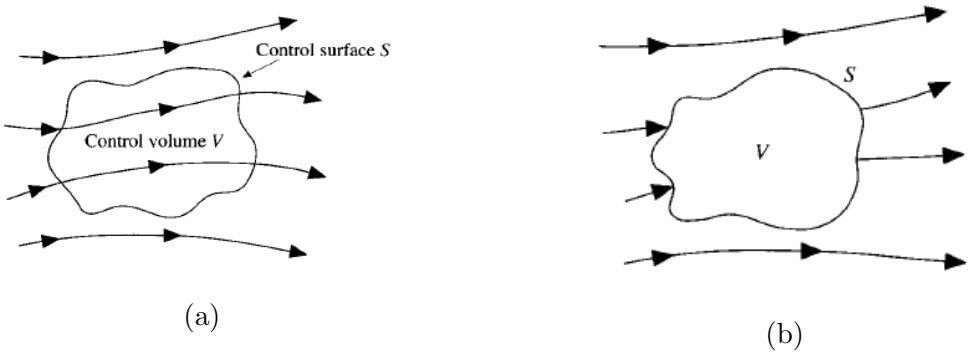

Figure 1.9: Finite Volume Approach (a) - Finite Control Volume Fixed in Space with Fluid Moving Through It, (b) - Finite Control Volume Moving with the Fluid Such That the Same Fluid Particles Are Always in the Same Control Volume [4].

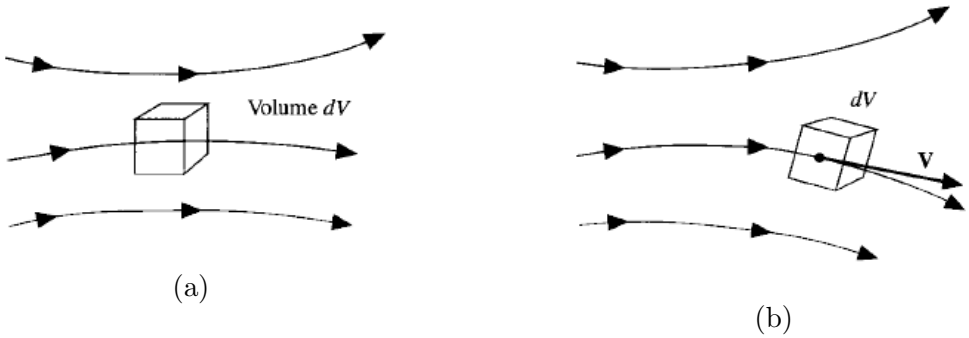

Figure 1.10: Infinitesimal Element Approach (a) - Infinitesimal Fluid Element Fixed in Space with Fluid Moving Through It, (B) - Infinitesimal Fluid Element Moving along a Streamline with the Velocity V Equal to the Local Flow Velocity at Each Point [4].

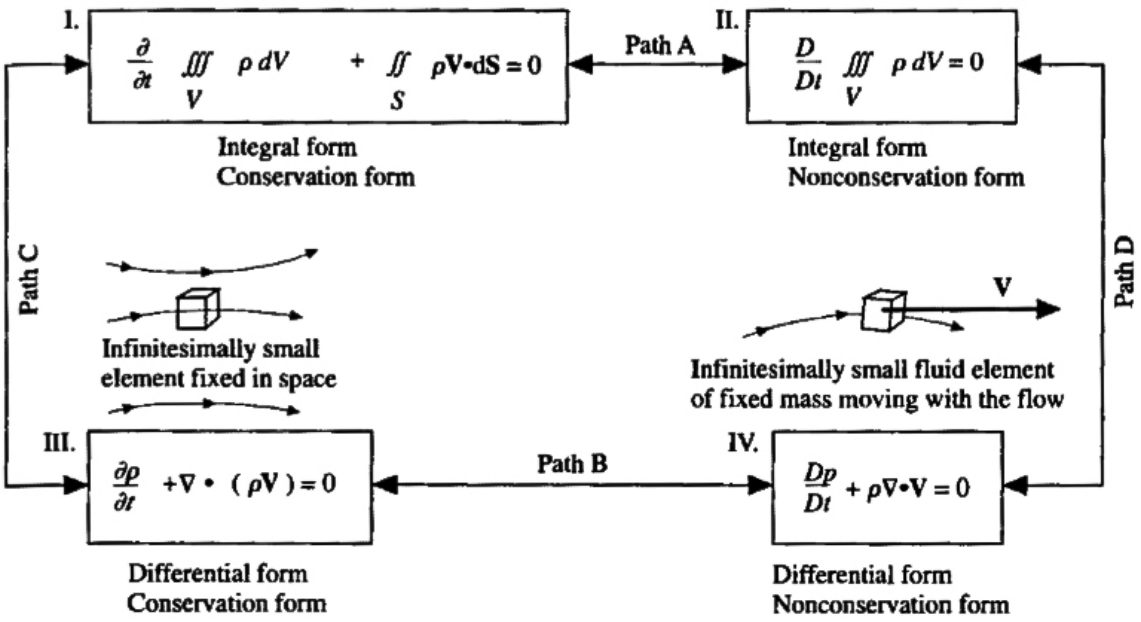

Figure 1.11: The Different Forms of the Continuity Equation and the Schematic Model Showing That All Four Are Same, and How They Can Be Obtained from the Other [4].

John D. Anderson in his book [4] describes a small difference between the integral form of the equations and the differential form. The integral form of the governing equations allows for the presence of discontinuities in the fixed control volume, whereas the differential form of the governing equations assumes the flow to be continuous. He even goes further and says " the integral form of the equations can be considered to be more fundamental than the differential form of the governing equations" [4, pg no 60].

Chapter 2

LITERATURE REVIEW

Cellular/Lattice structures have better specific properties (porosity, structural strength, surface area to volume ratio, large surface area) than their bulk counterparts [18, 19]. An introduction to cellular structures was given in Chapter 1. This chapter will provide a summary on the recent research done in the field and the applications of TPMS cellular structures.

2.1 Mechanical Properties of 3D Printed Gyroid Cellular Structures.

Diab W. Abueidda et. al. 3D printed Gyroid cellular structures using selective laser sintering (SLS), with polyamide 12 based thermo plastic. The structures were desgined using Solidworks, a CAD software. The specimens were designed with specification of 4 unit cell in each length, resulting in a 4 x 4 x 4 configuration, cells were of 2 x 2 x 2 cm^3. Also the structures were printed with relative density ranging from 7% to 46% [2].

An FEA analysis was performed on the specimens under tensile and compressive loading conditions. The tensile loading condition was 0.0066 s^{-1} strain rate applied until failure and the compressive test condition, strain rate of 0.01 s^{-1}applied until densification and the finite element analysis model used was Arruda-Boyce model.

As can be seen from Figure 2.1, as the relative density of the Gyroid structure is increased, the strength of the Gyroid structure increases. Also, each hump in Figure 2.1 represents the collapse of a layer in the direction of compression, and the number of humps directly represents the number of layers in the direction of compression [2].

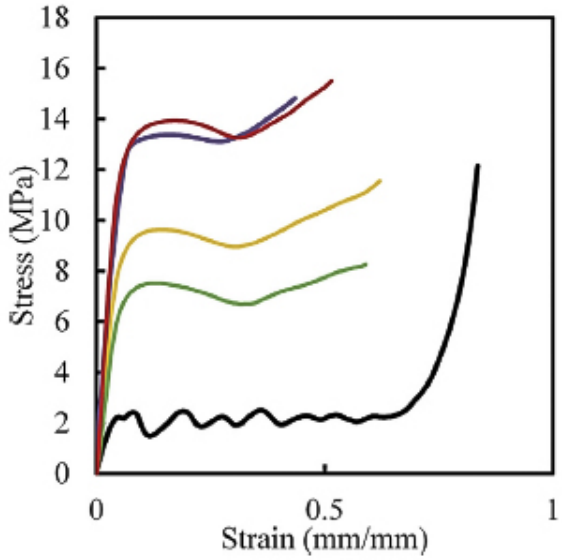

Figure 2.1: Stress - Strain Curves at Different Relative Densities of the Gyroid Structure [2].

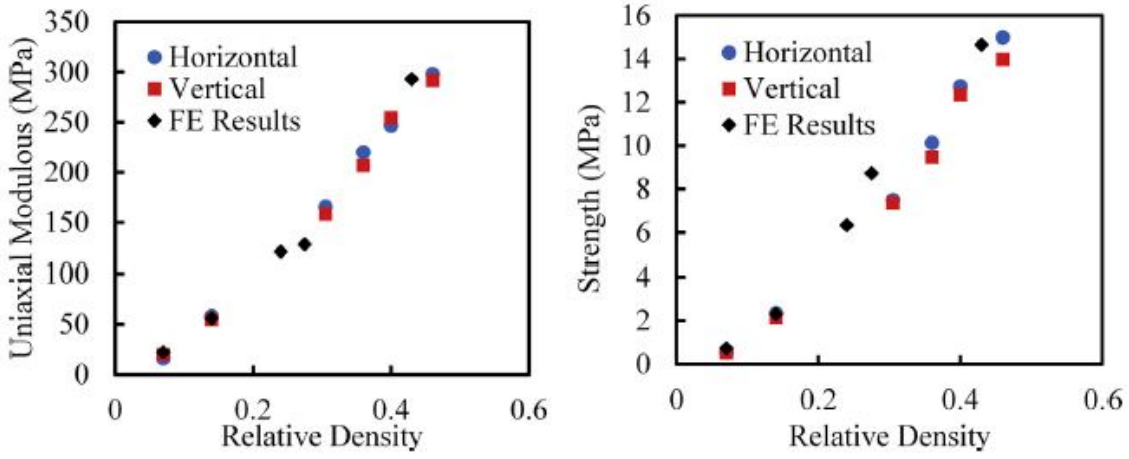

Figure 2.2: Computational and Experimental Results of Uni-axial Compressive Modulus and Compressive Strength of the Gyroid Structures at a Strain Rate Of .01 s^{-1} [2].

Also, mechanical testing was performed and results were compared to the FEA analysis. A compression test was performed at room temperature and a strain rate

of 0.01 s^{-1} was applied using the Instron 4400 machine (Instron, Norwood, Massachusetts, U.S.A.), following the ASTMD695-15 standard. The compressive uniaxial modulus and the compressive strength of the gyroid structures, computed both experimentally and computationally were plotted against each other, and as can be seen in Figure 2.2 the experimental and computational are in good agreement with each other [2].

2.2 Design Optimization of Gyroid-based Cellular Structures

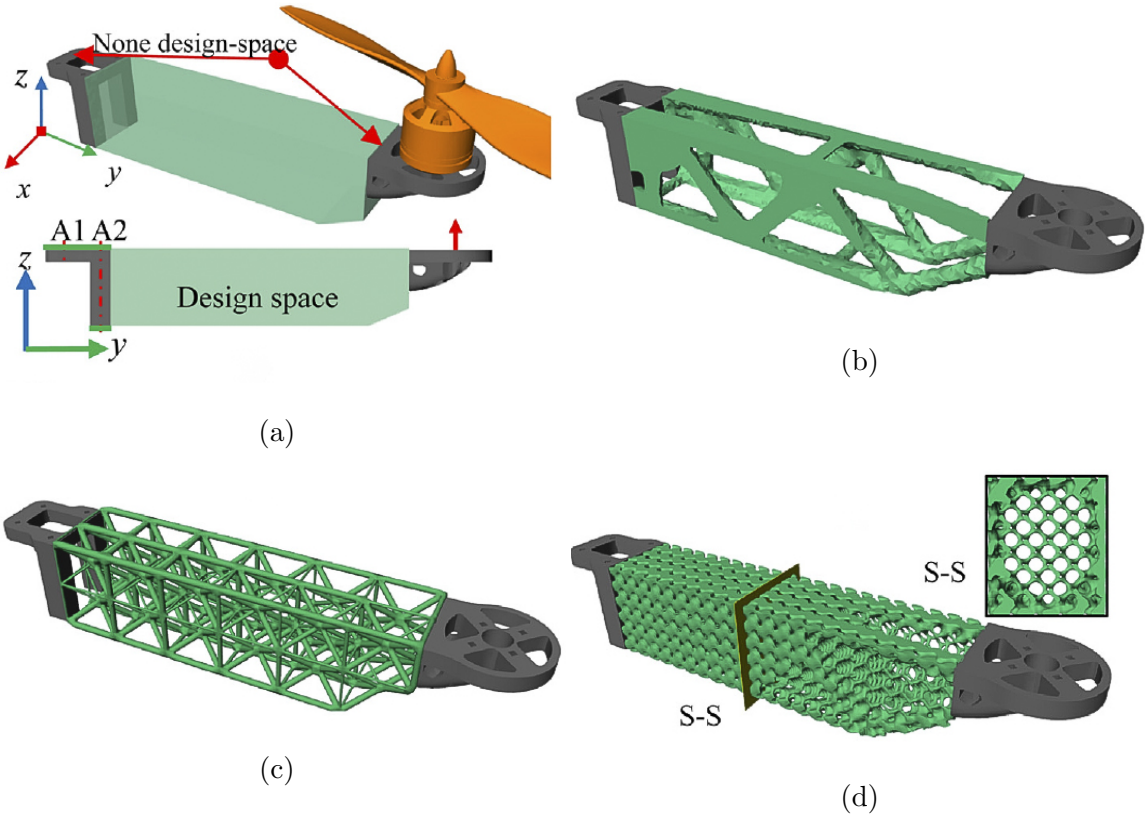

Figure 2.3: Topology Optimization of Quadcopter Arm: (a) - Initial Shape, (b) - Standard Topology Optimization Result, (c) - Traditional Truss Based Design, (d) - Gyroid Based Topology Optimization [22].

Dawei Li et. al. did a topology optimization of a quadcopter arm using Gyroid

based cellular structure and compared that to a traditional truss design quadcopter arm. The material used was ABS, with the following material properties - Young's modulus, E = 2070 MPa, Poisson's ratio, $\nu = 0.35$ and yield stress is 38 MPa [22].The topology optimization was done using a MATLAB code, and the FEA analysis was performed using OptiStruct 2017 software.

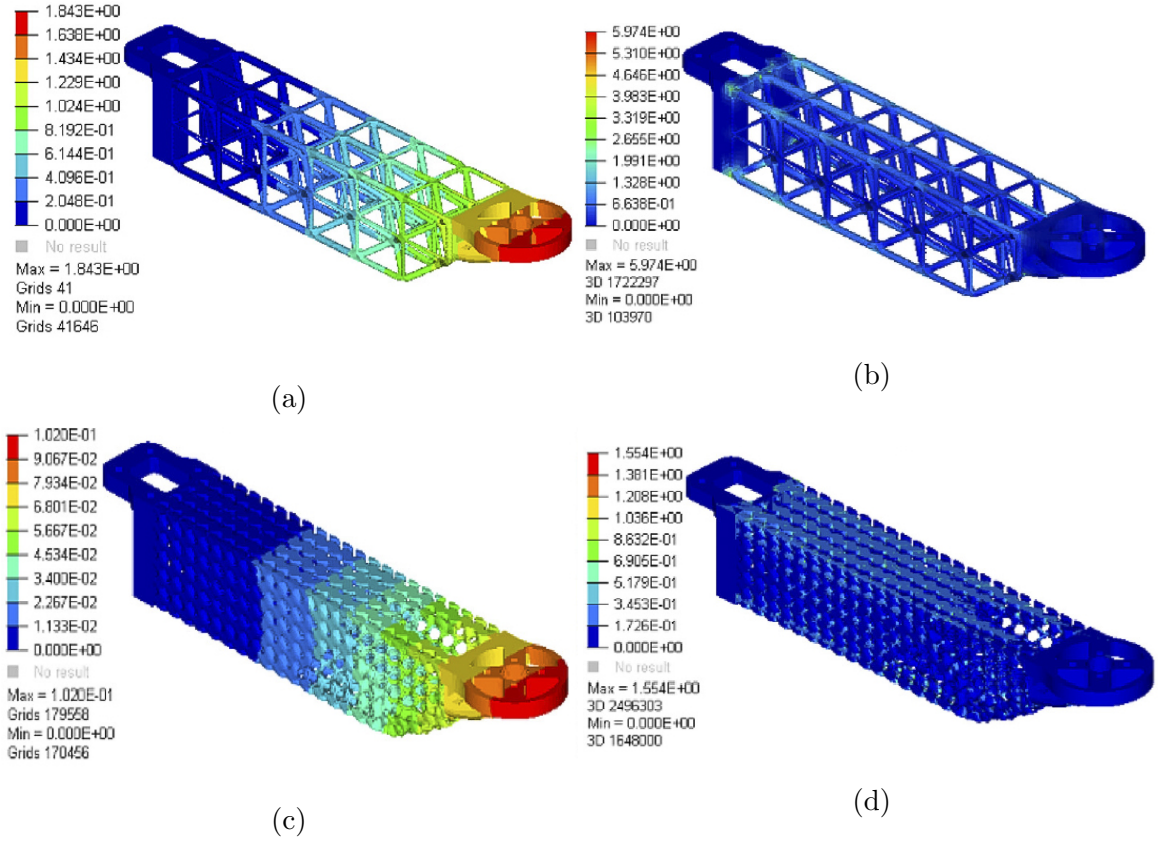

Figure 2.4: FEA Analysis Results of the Truss Design Quadcopter Arm and Gyroid - Based Topology Optimized Quadcopter Arm: (a) and (b) Displacement and Stress Contour of Traditional Truss Design Element; (c) and (d) Displacement and Stress Contour of Gyroid Based Topology Optimized Quadcopter Arm [22].

According to Dawaei Li et. al. the Gyroid based optimized qaudcopter arm had displacement 44.7% less than that of the traditional truss design arm for the

same load and boundary conditions. Hence, they concluded that Gyroid - based topology optimization can significantly improve the structural properties compared to the traditional design elements like the truss design element in the quadcopter arm [22]

2.3 3D Printing of High Surface Area Media for Use in Wastewater Treatment

Olivia Elliott et. al. designed and manufactured a spherical gyroid with high Specific Surface Area (SSA) to increase the performance of Moving-bed bioreactors (MBBR) systems in wastewater treatment. MBBR use carrier media to promote the growth of biofilm on their surfaces which in turn helps with the wastewater treatment [26].

A MBBR carrier media needs to have high surface area per unit volume while being light to be buoyant in the flowing fluid [26]. Some commercially available carrier media can be seen in Figure 2.5.

The performance of these carrier media is essentially a function of SSA, which is the ratio of the total surface area to the bulk volume (units are m^{-1}) [17]. However, these high SSA carrier media would be very difficult to manufacture using conventional manufacturing methods.

Elliott et. al. designed spherical gyroids of different diameters and pore sizes. After evaluating the different aspects in regarding with the media (eg:- overall size, manufacturability, choking, etc), they chose a gyroid based media with a diameter of 19 mm and a wall thickness of 500 μm to avoid clogging. The spherical gyroid based media were modelled in Mathematica, MB3 has the highest SSA, 604 m^2/m^3 [27] of the commercially available carrier media. Whereas, the spherical gyroid based media had a SSA of 1168 m^2/m^3, which is almost an increase of 93.37% over the MB3 carrier media. The model surface area and volume were measured using Netfabb® software

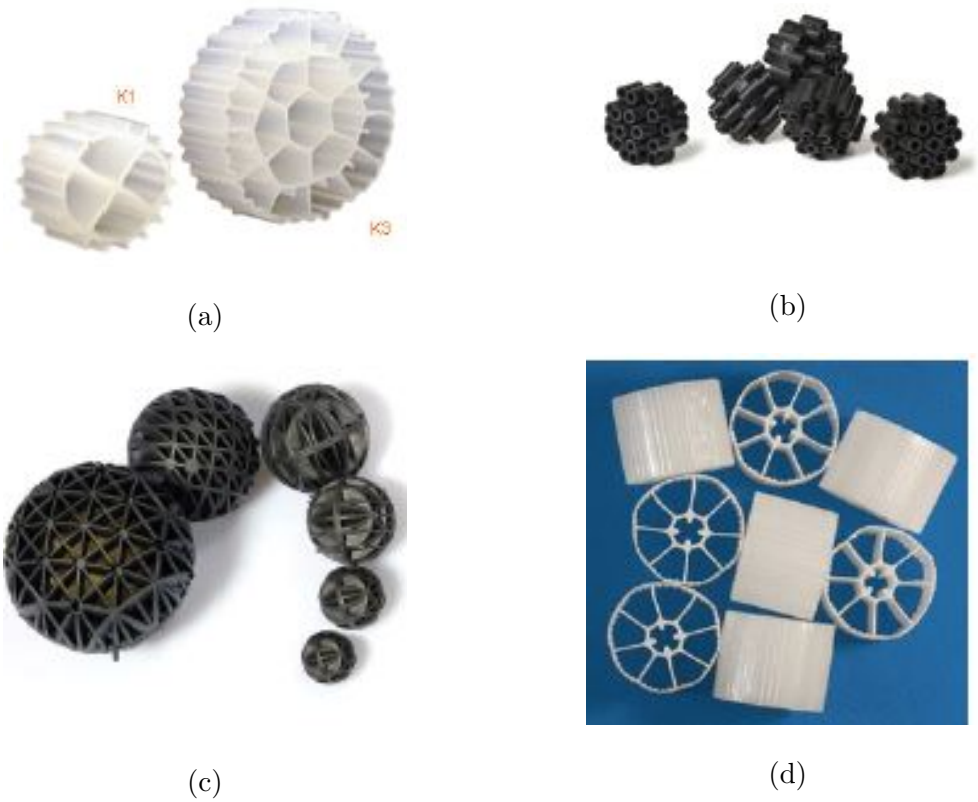

Figure 2.5: Commercially Available MBBR Carrier Media: (a) - K1, K3, (b) - Atlantic Bio-balls, (c) - Honeycomb Bio-balls, and (d) - MB3 Media [26].

(Autodesk, Mill Valley, California) [12].

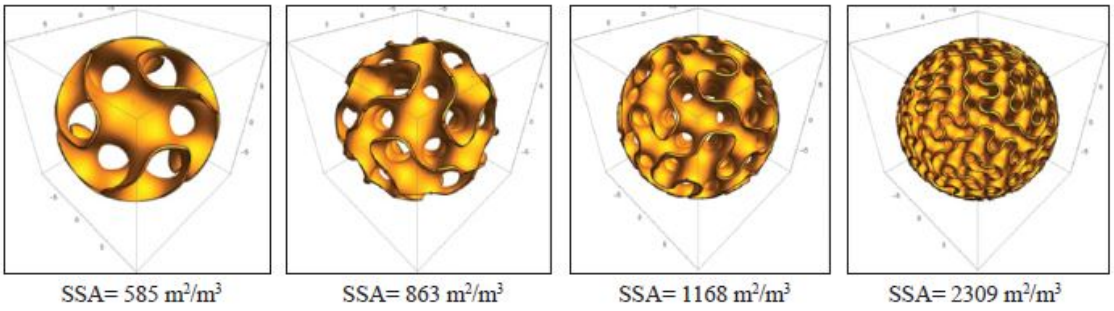

Figure 2.6: Specfic Surface Area of Modelled Spherical Gyroid Based Media [12].

The spherical gyroid based carrier media were 3D printed using a jet type 3D printer (Objet30, Stratasys®, Eden Prairie, MN) and the material was a acrylate

based monomer resin [12].

Adsorption tests were performed to compare the ammonia and nitrate concentration (in mg/L) levels K1 Kaldnes and spherical gyroid based carrier media. The analysis was performed using an EcoSense 9500 photometer (YSI, Yellow Springs, Ohio). The test was done in a 5-gallon reservoir containing three gallons of tilapia wastewater from North Auburn Fisheries, and it was being kept aerated constantly. Samples of 250 mL were taken everyday to measure the nutrient levels, and every three days 25% of the water was removed and replaced with freshwater [12].

It was found that the NH_3 removal rates for spherical gyroid and K1 Kaldnes, were 1.620 and 0.710 ppm/day, respectively [12].

Chapter 3

APPROACH

Strong and light structures are in a lot of demand in the automotive and aerospace industries. In recent years lot of research has been done on the use of TPMS structures like Schwarz D and gyroids for such applications, a brief introduction to some of these researches was given in Chapter 2. This has been made possible with the recent developments in additive manufacturing, considering these structures would be impossible to manufacture using conventional methods. The aim of this research is to prove that TPMS structures like Schwarz D and Gyroids not only have better mechanical properties like compressive strength, but also have better heat and mass transfer rates.

This chapter will explain how these models can be modelled and imported into any commercially available FEA packages like ANSYS 19.2 and Abaqus.

3.1 Designing and Development of the Models

TPMS models like Schwarz D and Gyroids are mathematical models, i.e. they are modelled using mathematical equations as explained in Section 1.1. The models were designed in an opensource software called MathMod-8.0, this software has many pre-stored models for which the equations are readily available. The equations can be modified as needed and also the number of unit cells can be modified according to need as seen in Figure 3.1

The equations for Schwarz D and Gyroid models that were used for this thesis are as follows:-

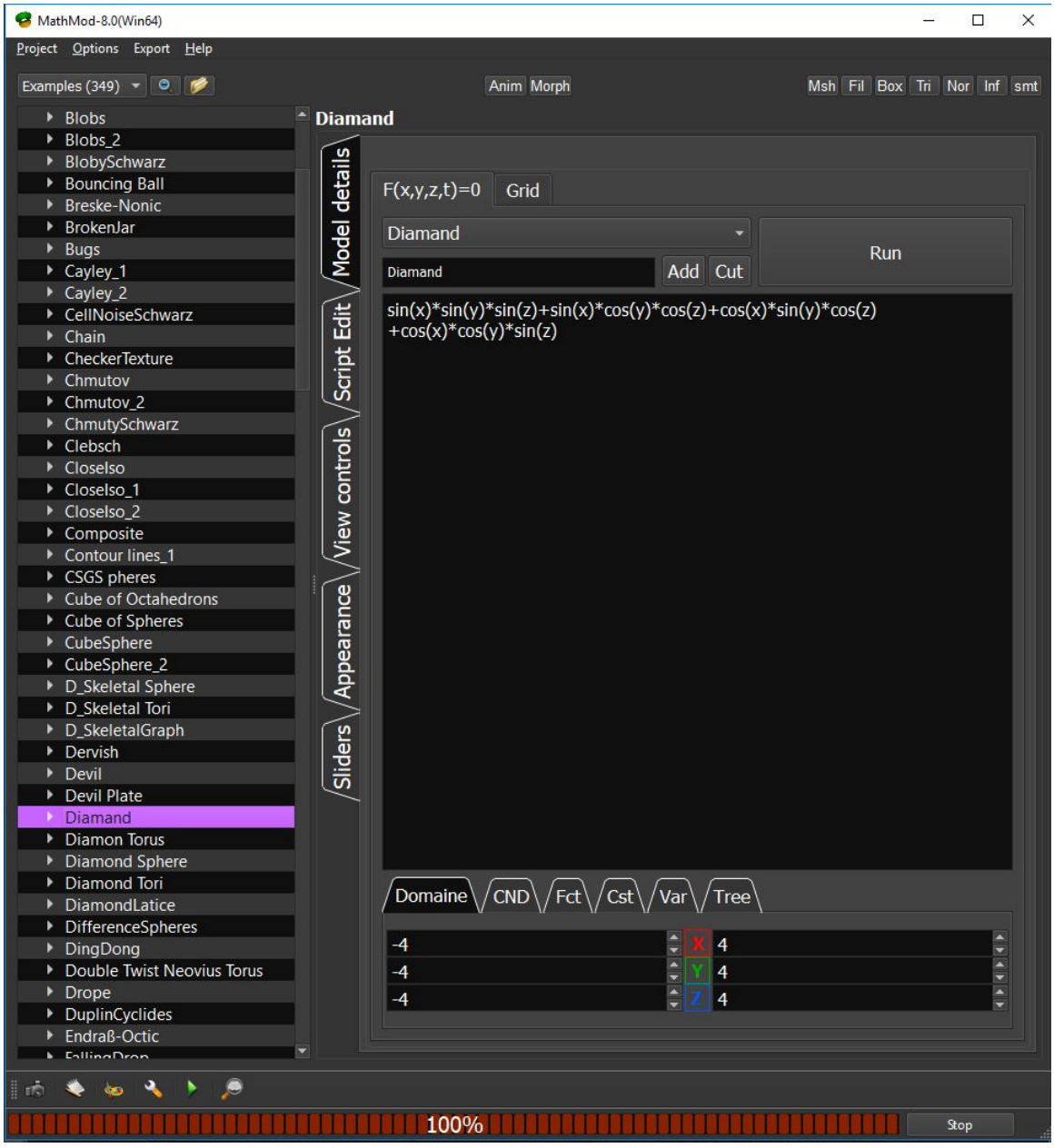

Figure 3.1: Opensource MathMod Software Package That Has Many TPMS Models and Other Structures Readily Available, and Provides the Option to Modify as Required.

Gyroid

$$\cos x * \sin y + \cos y * \sin z + \cos z * \sin x = 0 \tag{3.1}$$

Schwarz D

$$\sin x * \sin y * \sin z + \sin x * \cos y * \cos z + \cos x * \sin y * \cos z + \cos x * \cos y * \sin z = 0 \tag{3.2}$$

The above Gyroid equation was further modified to transform the Gyroid into a spherical gyroid, the final equation is given below.

Spherical Gyroid

$$(\cos x * \sin y + \cos y * \sin z + \cos z * \sin x)^2 - 0.6 + exp((x^2 + y^2 + z^2 - 64)/2) \tag{3.3}$$

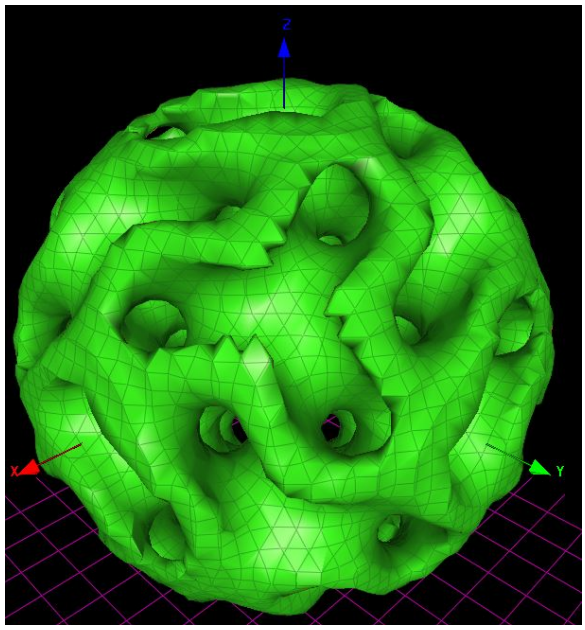

Figure 3.2: Spherical Gyroid Surface Model as Seen in MathMod

Equation (3.3) was imported into MathMod and a surface model of the spherical gyroid was developed as seen in Figure 3.2

Gyroid and Schwarz D models of 10, 15, 20, and 25 unit cells were exported as .OBJ (Triangle Wavefront) mesh files. FEA analysis packages like ANSYS don't read

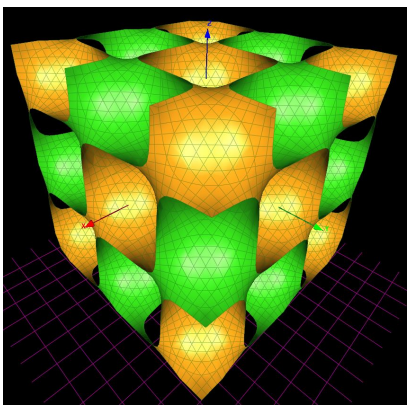

(a)

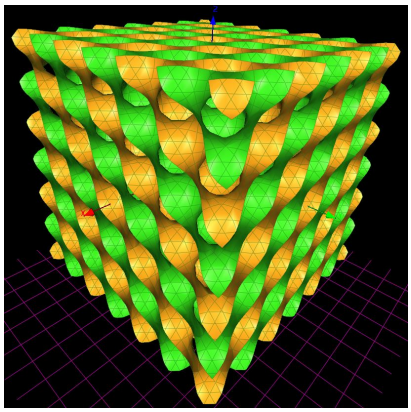

(b)

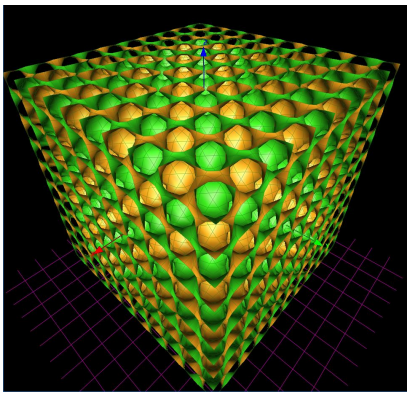

(c)

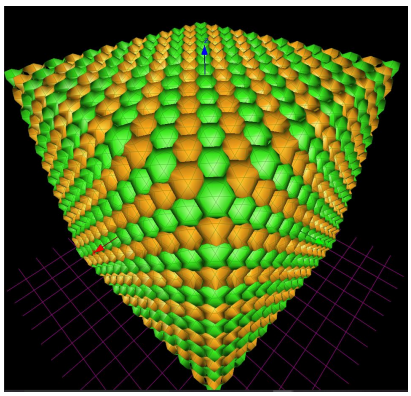

(d)

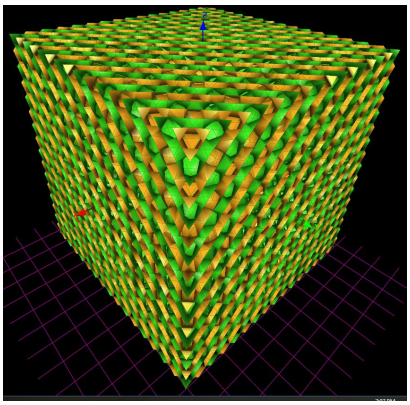

(e)

Figure 3.3: Schwarz D Surface Models of Different Number of Unit Cells as Seen in MathMod: (a) - 4, (b) - 10, (c) - 15, (d) - 20, (e) - 25.

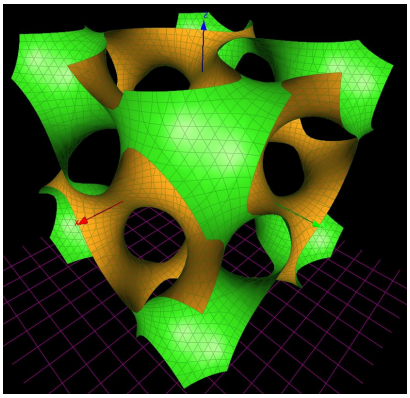

(a)

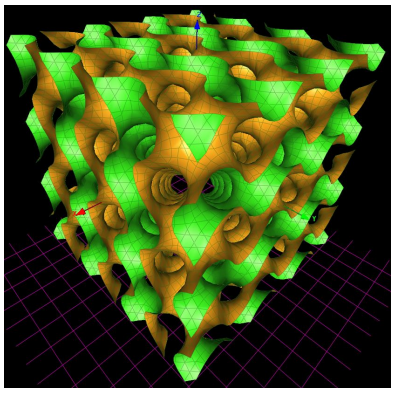

(b)

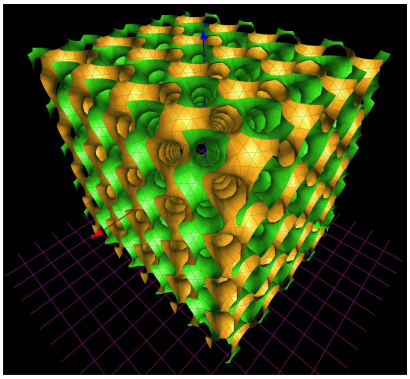

(c)

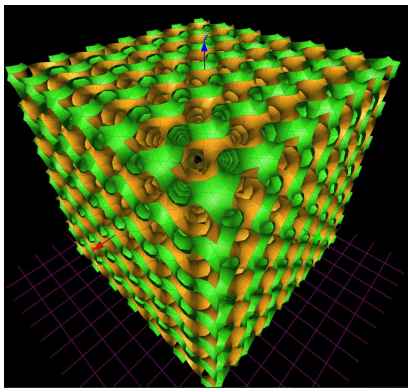

(d)

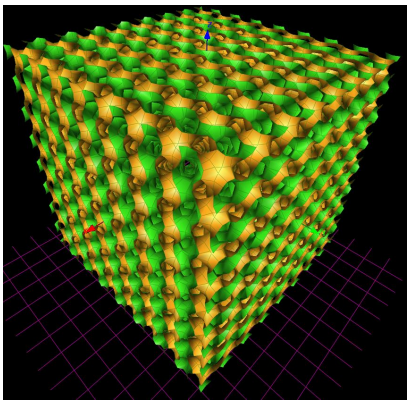

(e)

Figure 3.4: Gyroid Surface Models of Different Number of Unit Cells as Seen in MathMod: (a) - 4, (b) - 10, (c) - 15, (d) - 20, (e) - 25.

mesh file formats such as .OBJ and .STL. So, the .OBJ file was imported into CAD modelling software Autodesk Fusion 360 to be converted into a solid. The models developed in MathMod were 70 cm in size, and had to be scaled down in Fusion 360 for them to be additively manufactured successfully; in this research all the Schwarz D and Gyroid models are of 70 cm x 70 cm x 70 cm and the spherical gyroid was scaled down to 70 cm in diameter.

CAD modelling softwares have a tool called "Mesh to BRep" that can be used to convert mesh models into solid surface models, but Fusion 360 can only convert mesh files with 18000 - 20000 triangles or lesser depending on the complexity of the model. The surface models developed using MathMod had face triangles more than 50000, hence the "Mesh to BRep" wouldn't work. For Fusion 360 to be able to perform "Mesh to BRep" command successfully, the number of triangles in the models had to be reduced in Fusion 360. The converted files were exported into formats readily readable by ANSYS and other FEA packages like .sat, .stp, .igs, etc.

Also, for the purpose of validation and comparison of analysis and codes a random crosshatch structure (Figure 3.5a), a solid cube (Figure 3.5b), and a cube with pipes model (Figure 3.5c) of similar dimensions (70 mm x 70 mm x 70 mm) were created using the CAD modelling software Autodesk Inventor.

3.2 Area of Cross Section

The TPMS structures are so complicated that measuring the cross section by conventional means is not possible. The Cross-sectional area was required to calculate the thermal resistance as explained in Section 3.3.2. So the models developed were imported into Autodesk additive manufacturing package called Autodesk Netfabb, and the models were sliced in the software every $1/10^{\text{th}}$ of a mm, i.e 700 images for a 70 mm high model. The sliced images of the models were exported as .BMP files.

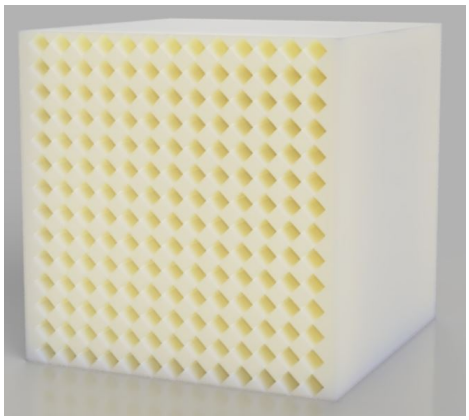

(a)

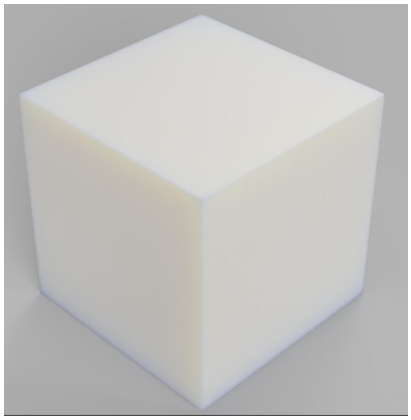

(b)

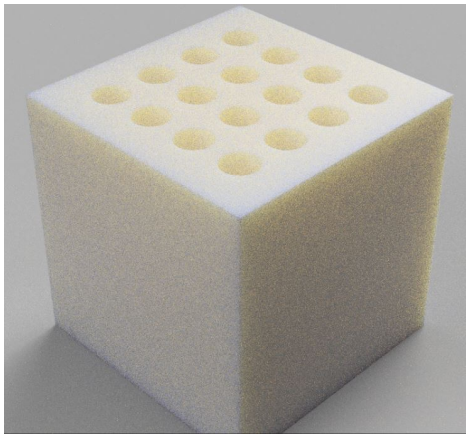

(c)

Figure 3.5: Random Structures Modelled in Autodesk Inventor for the Purpose of Validation and Comparison of the Analysis and Matlab Codes: (a) - Crosshatch, (b) - Solid Cube and (c) - Cube with Pipes.

The .BMP files were imported into MATLAB and the images were analyzed, as can be seen in Figure 3.6, the black area is the solid area and white is the void area. The images were imported into MATLAB and the percentage of black area was measured. Since, MATLAB sees an image in binary terms as 0 and 1, black is 0 and white is 1, so we can measure the pixels that are black and the ones that are white, giving us the percentage of black (see Appendix A). The cross section of these TPMS

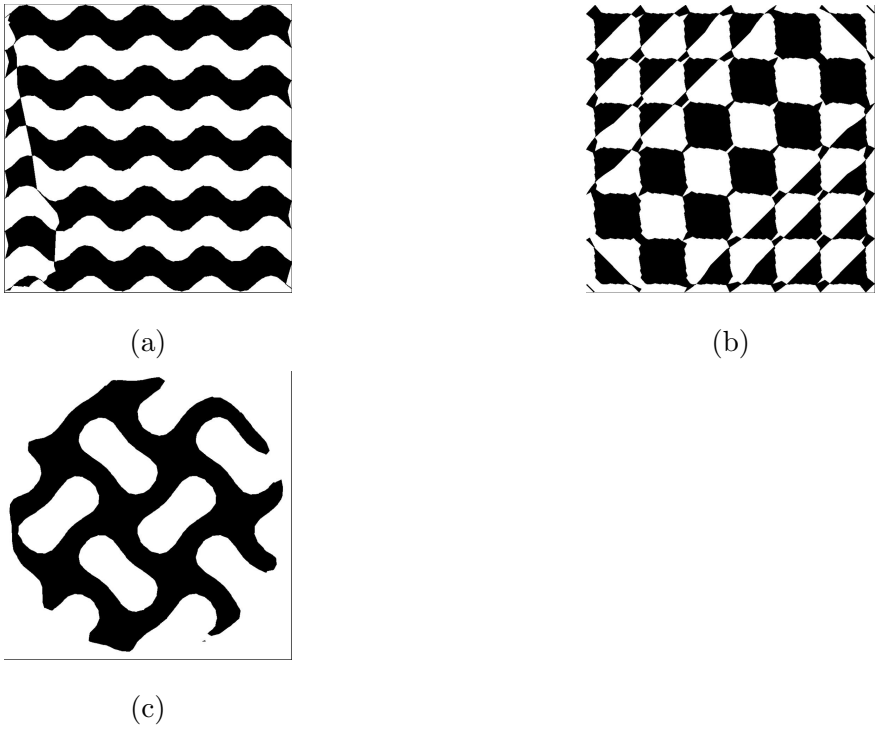

(a) (b)

(c)

Figure 3.6: Sliced Images of the TPMS Modelled as Exported from Autodesk Netfabb: (a) - Gyroid (10 Unit Cell), (b) - Schwarz D (10 Unit Cell), (c) - Spherical Gyroid.

models is not constant and varies layer to layer, as can be seen in Figure 3.7. So an average of the percentage black was calculated and this average percentage black was then multiplied by the area of the image which in this case was 70 mm x 70 mm = 4900 mm^2 to find an average cross sectional area for the model.

3.3 Finite Element Analysis

This section will explain the various loads, boundary conditions, materials and solver model under which the models were tested. Two kinds of FEA analysis were done (i) Compressive strength analysis and (ii) Thermal analysis, both were done at steady state conditions. The compressive and thermal analysis were performed in

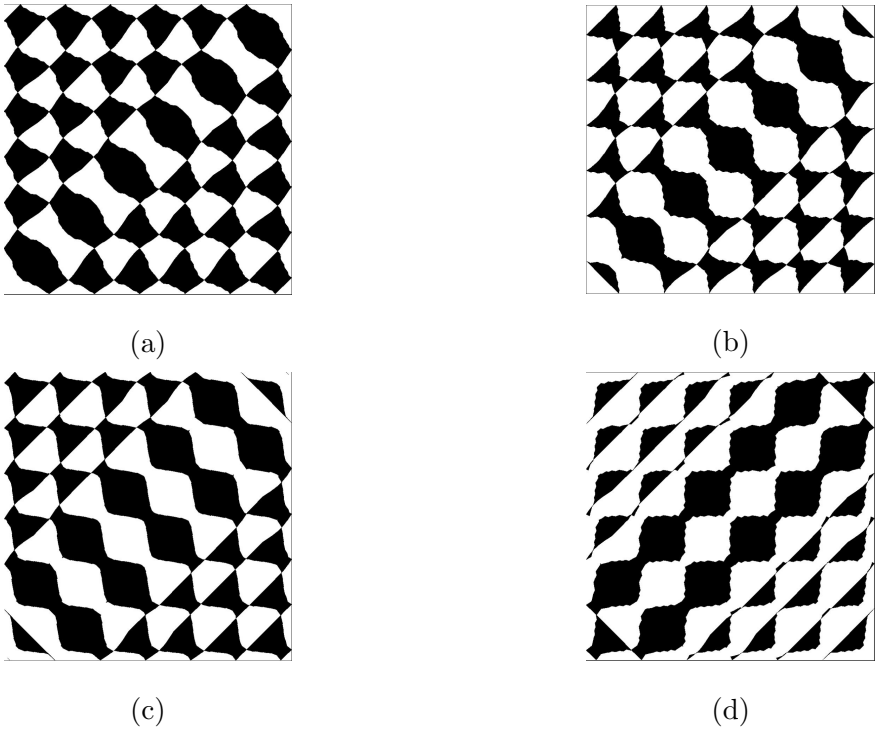

Figure 3.7: Sliced Images of the Developed Schwarz D Structure (10 Unit Cells) as Exported from Netfabb at Random Intervals: (a) - 6.3 mm, (b) - 13.7 mm, (c) - 18.3 mm and (d) - 19 mm.

ANSYS 19.2.

3.3.1 Compressive Strength Analysis

For the compressive analysis the model was fixed on the bottom and a force was applied on the top (Y axis) as seen in Figure 3.8. The material applied was Aluminium NL (non-linear), a non-linear model of bi-linear isotropic hardening was used so that a stress-strain curve could be plotted to be able to better understand the structure, by representing the real behaviour more accurately. The properties of the material were readily available in ANSYS 19.2. A static structural solver of ANSYS 19.2 was used to obtain the maximum principal stress and user defined result of EPTO was used.

Some of the user defined results available in ANSYS 19.2 are EPPL for plastic strain, EPEL for elastic strain and EPTO for plastic, elastic and creep strain combined. Also, for this analysis the large deformation option was turned ON in the analysis setting.

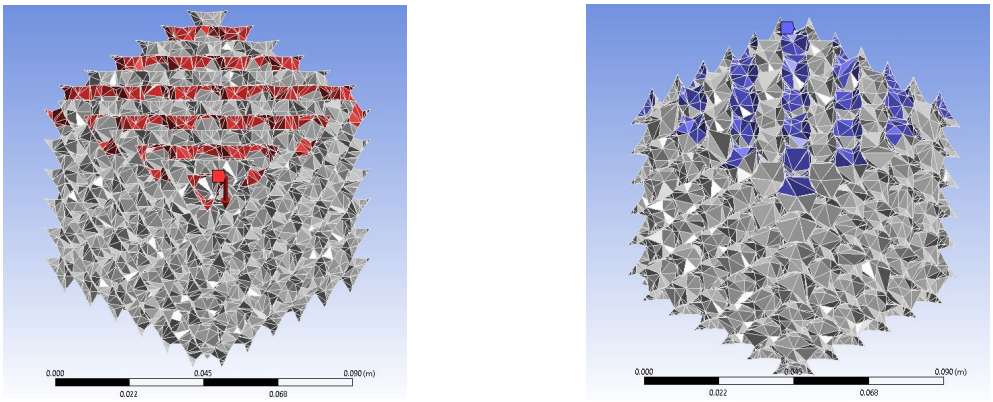

(a) (b)

Figure 3.8: Loading Conditions as Applied on a Schwarz D Model (10 Unit Cell and 1 Mm Wall Thickness) in ANSYS 19.2: (a) - a Force Was Applied on the Top in the Downward Direction (-Y Axis) and (b) - the Bottom of the Model Was Fixed Using Fixed Support in ANSYS 19.2. Similar Conditions Were Applied on All Other Models.

ANSYS 19.2 can't perform analysis on a surface model, and the solid models obtained from Fusion 360 are solid but surface models. So, a wall thickness was given in ANSYS 19.2, for the compressive analysis the Gyroid and Schwarz D were given a thickness of 1mm, 5mm and 10 mm. A ratio of the Young's modulus of the model (obtained from the slope of the linear portion of the stress v/s strain curve obtained from ANSYS) to the Young's modulus of the material (as applied in ANSYS) was calculated to measure and compare the stiffness of these TPMS models. .Also, an analysis was done on a solid cube (Figure 3.5b) of similar dimensions and

the crosshatch (Figure 3.5a) to compare and validate the results. The mesh sizes were restricted due to the ANSYS licence limitations, hence mesh refinement was not performed. The force that was applied for the corresponding models and thickness is shown in Table 3.1.

Model	**No. of Unit Cell**	**Thickness**	**Compressive Load**
Gyroid	10	1 mm	100 x 10^3 N
		5 mm	1 x 10^6 N
		10 mm	2.5 x 10^6 N
Schwarz D	10	1 mm	135 x 10^3 N
		5 mm	500 x 10^3 N
		10 mm	2 x 10^6 N
Solid Cube	1	NA	1.4 x 10^6 N
Crosshatch	1	NA	500 x 10^3 N

Table 3.1: Compressive Loads Applied on the Developed TPMS Models of Various Wall Thickness, a Random Crosshatch and Solid Cube Structure in ANSYS 19.2.

3.3.2 Thermal Analysis

A steady state thermal analysis of the developed TPMS and the random crosshatch (Figure 3.5a) and solid cube (Figure 3.5b) structures was performed using the Static Thermal model in ANSYS 19.2. Only conduction was considered, the material properties of ABS Plastic, Aluminum Alloy, Copper Alloy, Gray Cast Iron, Magnesium Alloy, and Stainless Steel were used for the thermal simulations performed. The wall thickness of the models were taken as 0.8 mm. No convection or radiation was con-

sidered, it was assumed that ANSYS 19.2 considers the voids to be vacuum and to confirm this assumption a thermal analysis was performed on the crosshatch as well, as the heat flux and temperature difference can me measured analytically. Temperature difference of 25°C (Hot face was given as 50°C and cold face was given as 25°C) given as an input, and the heat flux and the temperature distribution given as the output in ANSYS 19.2.

Also, the effective thermal resistance (R_{th}, with units of K/W) of the TPMS, crosshatch and solid cube structures will be calculated and compared using the average heat flux obtained from ANSYS 19.2. The following equation was used to calculate the thermal resistance.

$$Q = q * A_s \tag{3.4a}$$

$$R_{th} = \Delta T / Q \tag{3.4b}$$

Where the q is the heat flux (W/m^2) obtained from ANSYS, ΔT is the temperature difference applied and A_s is the cross-sectional area of the models. Also,thermal resistance was calculated using the area of cross-section including the voids having units of m^2K/W. The following sets of equations were used for calculating the $R_{th,\ new}$ using the cross-sectional area including the voids and $R_{th,\ new,\ m^2K/W}$ correspondingly.

$$Q_{new} = q * A_{s,\ including\ the\ voids} \tag{3.5a}$$

$$R_{th,\ new} = \Delta T / Q_{new} \tag{3.5b}$$

$$Q = q * A_s \tag{3.6a}$$

$$q_{new} = Q / A_{s,\ including\ the\ voids} \tag{3.6b}$$

$$R_{th,m^2K/W} = \Delta T / q_{new} \tag{3.6c}$$

The equations that were used to calculate the heat flux of the crosshatch analytically to validate the thermal analysis are as follows.

$$R = L/kA_{\mathrm{s}} \tag{3.7a}$$

$$Q = \Delta T/R \tag{3.7b}$$

$$q = Q/A_{\mathrm{s}} \tag{3.7c}$$

where R is the thermal resistance, L the length of the crosshatch, k the thermal conductivity of ABS, A_{s} the cross-sectional area in the direction of heat flow and q the heat flux.

A geometric characteristic number $L_{\mathrm{effective}}$ was introduced for the Gyroid and Schwarz D TPMS models of different cells, in the following way:

$$R_{\mathrm{th}} = L_{\mathrm{eff}}/kA_{\mathrm{s}} \tag{3.8a}$$

$$R_{\mathrm{th,\ simulation}} = \Delta T/qA_{\mathrm{s}} \tag{3.8b}$$

$$L_{\mathrm{eff}} = k * \Delta T/q \tag{3.8c}$$

where L_{eff} is the effective length of the models, q is the heat flux obtained from ANSYS 19.2, A_{s} is the cross sectional area of the models, ΔT is the temperature difference applied across the faces, and k is the thermal conductivity of the material used.

3.4 Computational Fluid Dynamics Analysis

A steady state, laminar flow simulation was performed on the Spherical gyroid structure. Commercial CFD packages like ANSYS Fluent or Altair Hyperworks cannot perform flow simulations on surface models. The "Mesh to BRep" command in

Fusion 360 was used to convert the mesh files into surface models readable by ANSYS 19.2, but they are not yet solid, they are hollow inside. So, a boundary fill command was used to try and convert the hollow models to Fusion 360, but because of the models being too complex Fusion 360 was only able to perform the command successfully on the spherical gyroid TPMS model. Even the thicken command in Solidworks was not able to handle these complicated structures. Also, a random structure of a cube with pipes Figure 3.5c was modelled in Autodesk Inventor to compare the flow simulations.

The solid spherical gyroid model was imported into ANSYS Fluent, pressure-based, relative solver model was used. An enclosure of 200 mm x 200 mm x 200 mm dimensions was created around the model, to act as a fluid domain. A boolean operation was performed to subtract the spherical gyroid TPMS model from the fluid domain. The inlet was specified as velocity-inlet and the outlet was given as outflow. The models were given as aluminium, the properties are readily available in ANSYS database. The simulation was performed for various velocities,and also for both air and water as fluids. The pressure and velocity were obtained as results for both inlet and outlet.

To check whether the flow was laminar or turbulent the flowing equation was used [33]

$$Re = \frac{VL}{\nu} \tag{3.9}$$

where Re is the Reynolds number, V is the flow velocity, L the length of the model and ν the kinematic viscosity of the fluid.

Chapter 4

RESULTS AND DISCUSSIONS

The analysis were performed as discussed in Chapter 3 and the various results obtained. In this chapter some the results will be shown and their significance discussed.

4.1 Cross Sectional Area and Surface Area to Volume Ratio

Table 4.1 shows the cross section area of the various developed TPMS models. Also, the surface area and volume of the developed models was measured using Netfabb and their ratio (see Section 2.3) was calculated. The surface area to volume ratio of the developed models is shown in Table 4.2

Table 4.1 shows the cross-sectional area of the developed TPMS models, the data was validated by using the same code to measure the cross-section of a known structure, in this case the crosshatch model. As can be seen in Table 4.1 gyroid TPMS of 15 unit cells has the largest cross-sectional area of all the TPMS and so can have better stress and temperature distribution characteristics.

Where as, Schwarz D TPMS of 20 unit cells has the highest Surface area/volume ratio amongst the TPMS structures as can be seen in Table 4.2, and even a little higher than the developed random crosshatch surface. So for adsorption or other porosity intensive applications the Schwarz D model with 20 unit cell would perform better than the others.

4.2 Compressive Strength Analysis

The results obtained from the compressive strength analysis will be shown and discussed in this section. As explained in Section 3.3.1 a non-linear material model

Model	**No. of Unit Cell**	**Percentage of Black**	**Cross-sectional Area (mm^2)**
Gyroid	10	0.5048	2.4735×10^3
	15	0.5056	2.4774×10^3
	20	0.4945	2.4231×10^3
	25	0.5021	2.4601×10^3
Schwarz D	10	0.3735	1.8302×10^3
	15	0.4295	2.1048×10^3
	20	0.4667	2.2869×10^3
	25	0.4690	2.2979×10^3
Spherical Gyroid	1	0.2533	1.241×10^3
Crosshatch	1	0.5478	2.6841×10^3

Table 4.1: Cross Sectional Area of the Developed TPMS Models and Crosshatch as Calculated Using the MATLAB Code.

was used, for ANSYS to be able to plot the stress-strain curves of the models.

Figure 4.1 and Figure 4.2 show the stress v/s strain curves of Gyroid and Schwarz D TPMS models of different thickness. As can be seen from the figures Gyroid TPMS has the ability to take more load without significant deformation. The 1 mm wall thickness versions of the Schwarz D and Gyroid is parabolic curve, this confirms what Abueidda et. al. [2] found that the thin wall TPMS models can absorb more load. This is possible because they deform layer by layer, hence absorbing more load with less significant deformation. This can be further explained by comparing the young's modulus of the TPMS models to Young's modulus of the material, and as can be seen

Model	**No. of Unit Cell**	**Surface Area (cm^2)**	**Volume (cm^3)**	**Surface Area/Volume (cm^{-1})**
Gyroid	10	976.567	171.785	5.6848
	15	957.283	171.799	5.5721
	20	1175.207	170.797	6.8807
	25	1175.203	170.797	6.8807
Schwarz D	10	978.754	126.171	7.7574
	15	1404.59	145.086	9.6810
	20	1809.43	156.95	11.5287
	25	1783.741	157.819	11.3024
Spherical Gyroid	1	399.965	86.165	4.6418
Crosshatch	1	2050.425	183.738	11.1595

Table 4.2: Surface Area to Volume Ratio of the Developed TPMS Models and Crosshatch as Obtained from Netfabb.

in Table 4.3 the Gyroid TPMS of 10 unit cells and 1 mm thickness has the highest ratio of 1.105, where as the crosshatch and the solid cube have the lowest of 0.335.

The compressive non-linear material analysis was validated by performing an analysis of a crosshatch and solid cube under same load and boundary conditions. As the stress-strain curves of the crosshatch and solid cube structures are as expected, it was concluded that the compressive analysis was comparable and assumed to be acceptable.

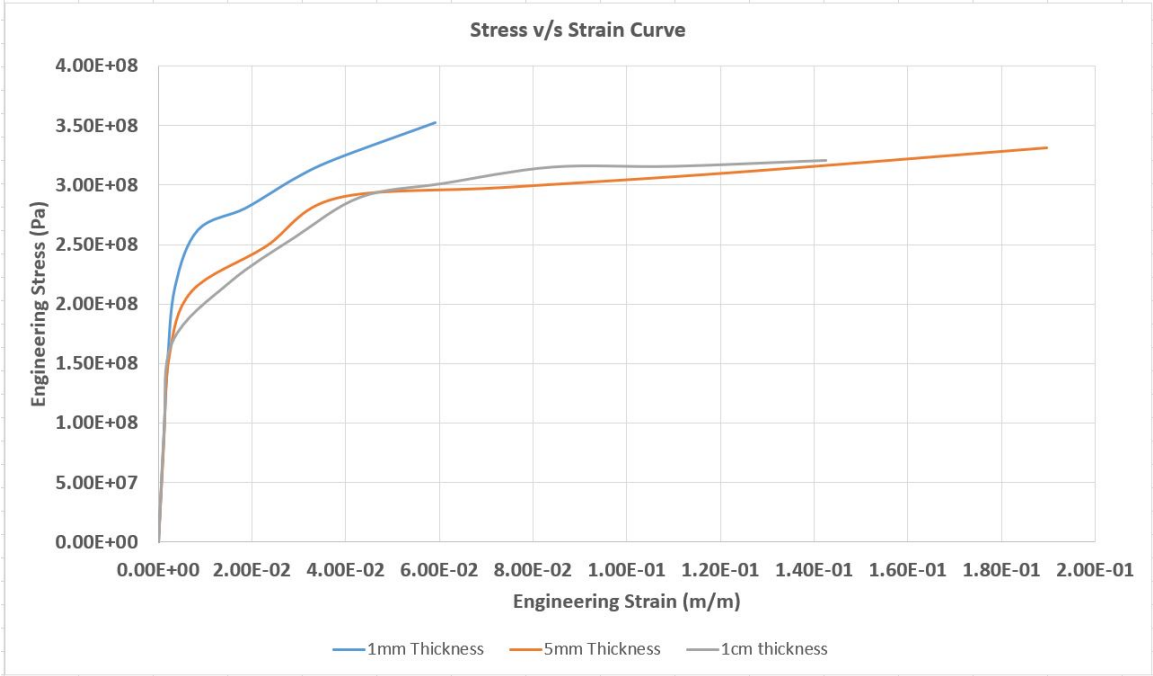

Figure 4.1: Stress V/S Strain Curve of Gyroid TPMS Model (10 Unit Cell) of Various Wall Thickness Plotted Against Each Other. For Individual Stress V/S Strain Curves Refer Appendix B.

4.3 Thermal Analysis

The results obtained from the thermal analysis will be presented and discussed in this section. As explained in Section 3.3.2 a conduction only analysis was done, and the effective thermal resistance was calculated as described in Section 3.3.2. The calculated thermal resistance of the TPMS models were compared to each other and the developed crosshatch and solid cube structures. Only the thermal resistance and the heat flux are shown and discussed in this section, for more complete results refer Appendix C

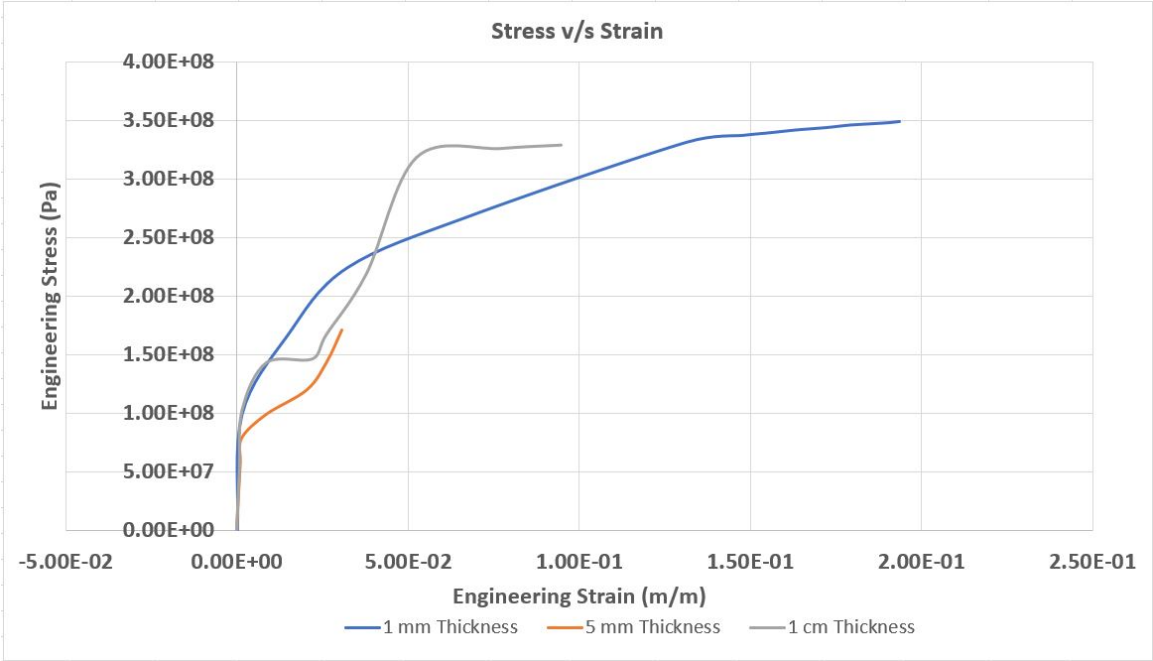

Figure 4.2: Stress V/S Strain Curve of Schwarz D TPMS Model (10 Unit Cell) of Various Wall Thickness Plotted Against Each Other. For Individual Stress V/S Strain Curves Refer Appendix B.

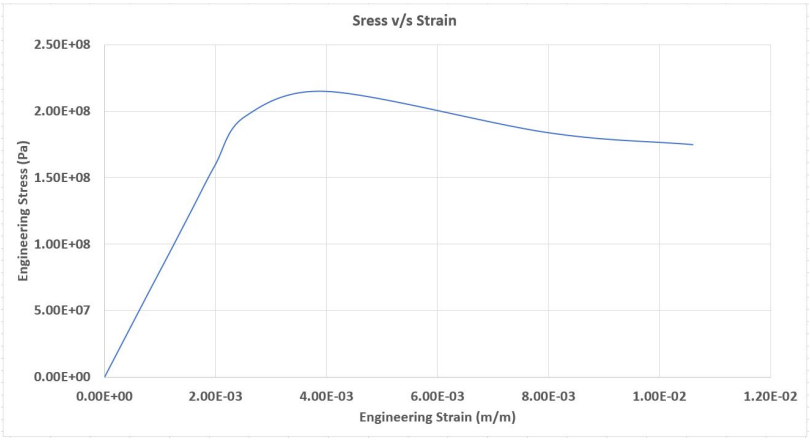

Figure 4.3: Stress V/S Strain Curve of a Crosshatch Structure of Similar Dimensions to the TPMS Models to Validate the Compressive Analysis.

Model	**No. of Unit Cell**	**Thickness**	**E**	**E***	**E*/E**
Schwarz D	10	1 mm	7.1 x 10^{10}	7.429 x 10^{10}	1.046
		5 mm	7.1 x 10^{10}	5.477 x 10^{10}	0.771
		10 mm	7.1 x 10^{10}	6.465 x 10^{10}	0.911
Gyroid	10	1 mm	7.1 x 10^{10}	7.842 x 10^{10}	1.105
		5 mm	7.1 x 10^{10}	7.476 x 10^{10}	1.053
		10 mm	7.1 x 10^{10}	7.748 x 10^{10}	1.091
Solid Cube	1	NA	7.1 x 10^{10}	2.377 x 10^{10}	0.335
Crosshatch	1	NA	7.1 x 10^{10}	8 x 10^{10}	0.335

Table 4.3: The Ratio of the Young's Modulus of the TPMS Models (E*) to the Young's Modulus of the Material (E) as Explained in Section 3.3.1.

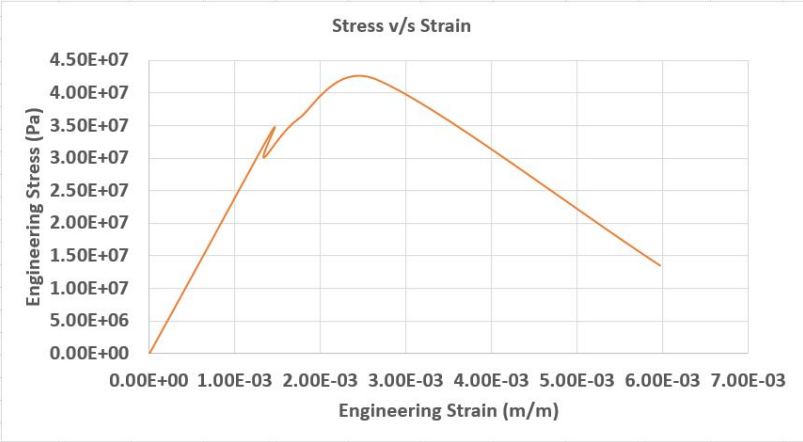

Figure 4.4: Stress V/S Strain Curve of a Solid Cube Structure of Similar Dimensions to the TPMS Models to Validate the Compressive Analysis.

Model	**No. of Unit Cell**	**ΔT(K)**	**Cross-sectional area (m^2)**	**Heat Flux (W/m^2)**	**R_{th} (K/W)**
Gyroid	10	25	2.4785×10^{-3}	66.473	152.05
	15	25	2.4774×10^{-3}	69.387	145.43
	20	25	2.4231×10^{-3}	68.662	150.26
	25	25	2.4601×10^{-3}	159.36	63.77
Schwarz D	10	25	1.8302×10^{-3}	67.03	203.79
	15	25	2.1048×10^{-3}	68.618	173.097
	20	25	2.2869×10^{-3}	56.445	193.67
	25	25	2.2979×10^{-3}	66.552	163.47
Spherical Gyroid	1	25	1.241×10^{-3}	140.08	143.81
Crosshatch	1	25	2.6841×10^{-3}	92.143	101.083
Solid Cube	1	25	4900×10^{-6}	92.143	55.37

Table 4.4: Thermal Resistance (K/W) of the TPMS Models, Crosshatch and Solid Cube with the Material Properties of ABS Plastic Applied in ANSYS 19.2, as Explained In Section 3.3.2.

Model	**No. of Unit Cell**	**ΔT(K)**	**Cross-sectional area (m^2)**	**Heat Flux (W/m^2)**	**R_{th} (K/W)**
Gyroid	10	25	2.4785×10^{-3}	38696	0.2607
	15	25	2.4774×10^{-3}	40845	0.2471
	20	25	2.4231×10^{-3}	40419	0.2553
	25	25	2.4601×10^{-3}	93814	0.1083
Schwarz D	10	25	1.8302×10^{-3}	36741	0.3718
	15	25	2.1048×10^{-3}	40393	0.2941
	20	25	2.2869×10^{-3}	33227	0.3290
	25	25	2.2979×10^{-3}	39982	0.2721
Spherical Gyroid	1	25	1.241×10^{-3}	68907	0.2924
Crosshatch	1	25	2.6841×10^{-3}	54241	0.1724
Solid Cube	1	25	4900×10^{-6}	54241	0.0941

Table 4.5: Thermal Resistance (K/W) of the TPMS Models, Crosshatch and Solid Cube with the Material Properties of Aluminum Alloy Applied in ANSYS 19.2, as Explained In Section 3.3.2.

Model	**No. of Unit Cell**	**ΔT(K)**	**Cross-sectional area (m^2)**	**Heat Flux (W/m^2)**	**R_{th} (K/W)**
Gyroid	10	25	2.4785×10^{-3}	1.021×10^{5}	0.0988
	15	25	2.4774×10^{-3}	1.079×10^{5}	0.0936
	20	25	2.4231×10^{-3}	1.067×10^{5}	0.0967
	25	25	2.4601×10^{-3}	2.477×10^{5}	0.0410
Schwarz D	10	25	1.8302×10^{-3}	97008	0.1408
	15	25	2.1048×10^{-3}	1.067×10^{5}	0.1114
	20	25	2.2869×10^{-3}	87730	0.1246
	25	25	2.2979×10^{-3}	1.056×10^{5}	0.1031
Spherical Gyroid	1	25	1.241×10^{-3}	1.819×10^{5}	0.1107
Crosshatch	1	25	2.6841×10^{-3}	1.432×10^{5}	0.0653
Solid Cube	1	25	4900×10^{-6}	1.432×10^{5}	0.0356

Table 4.6: Thermal Resistance (K/W) of the TPMS Models, Crosshatch and Solid Cube with the Material Properties of Copper Alloy Applied in ANSYS 19.2, as Explained In Section 3.3.2.

Model	**No. of Unit Cell**	**ΔT(K)**	**Cross-sectional area (m^2)**	**Heat Flux (W/m^2)**	**R_{th} (K/W)**
Gyroid	10	25	2.4785×10^{-3}	13245	0.7616
	15	25	2.4774×10^{-3}	13985	0.7216
	20	25	2.4231×10^{-3}	13839	0.7455
	25	25	2.4601×10^{-3}	32120	0.3164
Schwarz D	10	25	1.8302×10^{-3}	12580	1.0858
	15	25	2.1048×10^{-3}	13830	0.8588
	20	25	2.2869×10^{-3}	11376	0.9610
	25	25	2.2979×10^{-3}	13688	0.7948
Spherical Gyroid	1	25	1.241×10^{-3}	23589	0.8540
Crosshatch	1	25	2.6841×10^{-3}	18571	0.5034
Solid Cube	1	25	4900×10^{-6}	18571	0.2747

Table 4.7: Thermal Resistance (K/W) of the TPMS Models, Crosshatch and Solid Cube with the Material Properties of Gray Cast Iron Applied in ANSYS 19.2, as Explained In Section 3.3.2.

Model	**No. of Unit Cell**	**$\Delta T(K)$**	**Cross-sectional area (m^2)**	**Heat Flux (W/m^2)**	**R_{th} (K/W)**
Gyroid	10	25	2.4785×10^{-3}	39374	0.2539
	15	25	2.4774×10^{-3}	41955	0.2405
	20	25	2.4231×10^{-3}	41516	0.2485
	25	25	2.4601×10^{-3}	96359	0.1055
Schwarz D	10	25	1.8302×10^{-3}	37739	0.3620
	15	25	2.1048×10^{-3}	41490	0.2863
	20	25	2.2869×10^{-3}	34129	0.3203
	25	25	2.2979×10^{-3}	41064	0.2649
Spherical Gyroid	1	25	1.241×10^{-3}	70766	0.2847
Crosshatch	1	25	2.6841×10^{-3}	55714	0.1678
Solid Cube	1	25	4900×10^{-6}	55714	0.0916

Table 4.8: Thermal Resistance (K/W) of the TPMS Models, Crosshatch and Solid Cube with the Material Properties of Magnesium Alloy Applied in ANSYS 19.2, as Explained In Section 3.3.2.

Model	**No. of Unit Cell**	**ΔT(K)**	**Cross-sectional area (m^2)**	**Heat Flux (W/m^2)**	**R_{th} (K/W)**
Gyroid	10	25	2.4785×10^{-3}	3846	2.6227
	15	25	2.4774×10^{-3}	4061	2.4849
	20	25	2.4231×10^{-3}	4018.6	2.5674
	25	25	2.4601×10^{-3}	9327	1.0895
Schwarz D	10	25	1.8302×10^{-3}	3652.9	3.7394
	15	25	2.1048×10^{-3}	4016	2.9576
	20	25	2.2869×10^{-3}	3303.6	3.3091
	25	25	2.2979×10^{-3}	3974.8	2.7371
Spherical Gyroid	1	25	1.241×10^{-3}	6849.8	2.9410
Crosshatch	1	25	2.6841×10^{-3}	5392.9	1.7336
Solid Cube	1	25	4900×10^{-6}	5392.9	0.9461

Table 4.9: Thermal Resistance (K/W) of the TPMS Models, Crosshatch and Solid Cube with the Material Properties of Stainless Steel Applied in ANSYS 19.2, as Explained In Section 3.3.2.

Model	**No. of Unit Cell**	**$\Delta T(K)$**	**Cross-sectional area including the voids (m^2)**	**Heat Flux (W/m^2)**	**$R_{th,\ new}$ (K/W)**
Gyroid	10	25	4900×10^{-6}	66.473	76.7536
	15	25	4900×10^{-6}	69.387	73.5302
	20	25	4900×10^{-6}	68.662	74.3066
	25	25	4900×10^{-6}	159.36	32.0158
Schwarz D	10	25	4900×10^{-6}	67.03	76.1158
	15	25	4900×10^{-6}	68.618	74.3543
	20	25	4900×10^{-6}	56.445	90.3896
	25	25	4900×10^{-6}	66.552	76.6625
Spherical Gyroid	1	25	3.8485×10^{-3}	140.08	46.3738
Crosshatch	1	25	4900×10^{-6}	92.143	55.3709
Solid Cube	1	25	4900×10^{-6}	92.143	55.3709

Table 4.10: Thermal Resistance (K/W) of the TPMS Models, Crosshatch and Solid Cube Including the Voids Cross-sectional Area with the Material Properties of ABS Plastic Applied in ANSYS 19.2, as Explained In Section 3.3.2.

Model	**No. of Unit Cell**	**$\Delta T(K)$**	**Cross-sectional area including the voids (m^2)**	**Heat Flux (W/m^2)**	**$R_{th,\ new}$ (K/W)**
Gyroid	10	25	4900×10^{-6}	38696	0.1318
	15	25	4900×10^{-6}	40845	0.1249
	20	25	4900×10^{-6}	40419	0.1262
	25	25	4900×10^{-6}	93814	0.0544
Schwarz D	10	25	4900×10^{-6}	36741	0.1384
	15	25	4900×10^{-6}	40393	0.1263
	20	25	4900×10^{-6}	33227	0.1536
	25	25	4900×10^{-6}	39982	0.1276
Spherical Gyroid	1	25	3.8485×10^{-3}	68907	0.0943
Crosshatch	1	25	4900×10^{-6}	54241	0.0941
Solid Cube	1	25	4900×10^{-6}	54241	0.0941

Table 4.11: Thermal Resistance (K/W) of the TPMS Models, Crosshatch and Solid Cube Including the Voids Cross-sectional Area with the Material Properties of Aluminum Alloy Applied in ANSYS 19.2, as Explained In Section 3.3.2.

Model	**No. of Unit Cell**	**ΔT(K)**	**Cross-sectional area including the voids (m^2)**	**Heat Flux (W/m^2)**	**$R_{th,\ new}$ (K/W)**
Gyroid	10	25	4900×10^{-6}	1.021×10^5	0.05
	15	25	4900×10^{-6}	1.079×10^5	0.0473
	20	25	4900×10^{-6}	1.067×10^5	0.0478
	25	25	4900×10^{-6}	2.477×10^5	0.0206
Schwarz D	10	25	4900×10^{-6}	97008	0.0526
	15	25	4900×10^{-6}	1.067×10^5	0.0478
	20	25	4900×10^{-6}	87730	0.0582
	25	25	4900×10^{-6}	1.056×10^5	0.0483
Spherical Gyroid	1	25	3.8485×10^{-3}	1.819×10^5	0.0357
Crosshatch	1	25	4900×10^{-6}	1.432×10^5	0.0356
Solid Cube	1	25	4900×10^{-6}	1.432×10^5	0.0356

Table 4.12: Thermal Resistance (K/W) of the TPMS Models, Crosshatch and Solid Cube Including the Voids Cross-sectional Area with the Material Properties of Copper Alloy Applied in ANSYS 19.2, as Explained In Section 3.3.2.

Model	**No. of Unit Cell**	**$\Delta T(K)$**	**Cross-sectional area including the voids (m^2)**	**Heat Flux (W/m^2)**	**$R_{th,\ new}$ (K/W)**
Gyroid	10	25	4900×10^{-6}	13245	0.3852
	15	25	4900×10^{-6}	13985	0.3648
	20	25	4900×10^{-6}	13839	0.3687
	25	25	4900×10^{-6}	32120	0.1588
Schwarz D	10	25	4900×10^{-6}	12580	0.4056
	15	25	4900×10^{-6}	13830	0.3689
	20	25	4900×10^{-6}	11376	0.4485
	25	25	4900×10^{-6}	13688	0.3727
Spherical Gyroid	1	25	3.8485×10^{-3}	23589	0.2754
Crosshatch	1	25	4900×10^{-6}	18571	0.2747
Solid Cube	1	25	4900×10^{-6}	18571	0.2747

Table 4.13: Thermal Resistance (K/W) of the TPMS Models, Crosshatch and Solid Cube Including the Voids Cross-sectional Area with the Material Properties of Gray Cast Iron Applied in ANSYS 19.2, as Explained In Section 3.3.2.

Model	**No. of Unit Cell**	**$\Delta T(K)$**	**Cross-sectional area including the voids (m^2)**	**Heat Flux (W/m^2)**	**$R_{th,\ new}$ (K/W)**
Gyroid	10	25	4900×10^{-6}	39374	0.1296
	15	25	4900×10^{-6}	41955	0.1216
	20	25	4900×10^{-6}	41516	0.1229
	25	25	4900×10^{-6}	96359	0.0529
Schwarz D	10	25	4900×10^{-6}	37739	0.1352
	15	25	4900×10^{-6}	41490	0.1230
	20	25	4900×10^{-6}	34129	0.1495
	25	25	4900×10^{-6}	41064	0.1242
Spherical Gyroid	1	25	3.8485×10^{-3}	70766	0.0918
Crosshatch	1	25	4900×10^{-6}	55714	0.0916
Solid Cube	1	25	4900×10^{-6}	55714	0.0916

Table 4.14: Thermal Resistance (K/W) of the TPMS Models, Crosshatch and Solid Cube Including the Voids Cross-sectional Area with the Material Properties of Magnesium Alloy Applied in ANSYS 19.2, as Explained In Section 3.3.2.

Model	**No. of Unit Cell**	**ΔT(K)**	**Cross-sectional area (m^2)**	**q (W/m^2)**	**Q (W)**	**q_{new} (W/m^2)**	**R_{th} (m^2K/W)**
Gyroid	10	25	2.4785×10^{-3}	66.473	0.1648	33.6231	0.7435
	15	25	2.4774×10^{-3}	69.387	0.1719	35.0815	0.7126
	20	25	2.4231×10^{-3}	68.662	0.1664	33.9541	0.7363
	25	25	2.4601×10^{-3}	159.36	0.392	80.0085	0.3125
Schwarz D	10	25	1.8302×10^{-3}	67.03	0.1227	25.0364	0.9985
	15	25	2.1048×10^{-3}	68.618	0.1444	29.4749	0.8482
	20	25	2.2869×10^{-3}	56.445	0.1291	26.3437	0.9490
	25	25	2.2979×10^{-3}	66.552	0.1529	31.2102	0.8010
Spherical Gyroid	1	25	1.241×10^{-3}	140.08	0.1738	45.1707	0.5535
Crosshatch	1	25	2.6841×10^{-3}	92.143	0.2473	50.4737	0.4953
Solid Cube	1	25	4900×10^{-6}	92.143	0.4515	92.1430	0.2713

Table 4.15: Thermal Resistance (m^2K/W) of the TPMS Models, Crosshatch and Solid Cube Including the Voids Cross-sectional Area with the Material Properties of ABS Plastic Applied in ANSYS 19.2, as Explained in Section 3.3.2

Model	**No. of Unit Cell**	**ΔT(K)**	**Heat Flux (W/m^2)**	**K (W/mK)**	**L_{eff} (m)**
Gyroid	10	25	66.473	0.258	0.097
	15	25	69.387	0.258	0.093
	20	25	68.662	0.258	0.094
	25	25	159.36	0.258	0.040
Schwarz D	10	25	67.03	0.258	0.096
	15	25	68.618	0.258	0.094
	20	25	56.445	0.258	0.114
	25	25	66.552	0.258	0.097

Table 4.16: Effective Length ($L_{effective}$) of the Gyroid and Schwarz D TPMS Models with the Material Properties and Heat Flux of ABS Plastic Applied in ANSYS 19.2, as Explained In Section 3.3.2.

The thermal resistance of the Gyroid model with 25 unit cell is the most comparable to that of a solid cube when only conduction is considered. The thermal resistance of the Gyroid with 25 unit cells was 63.77 K/W as compared to the 55.37 K/W of the solid cube, as can be seen in Table 4.16. If the thermal resistance of the models considering the cross-sectional area including the voids, the Gyroid model with 25 unit cells performs better than the solid cube in terms of the conduction performance with the Gyroid having 32.016 K/W and the solid cube having 55.37 K/W as can be seen in Table 4.10. According to R_{th} (m^2K/W) the solid cube performs better than the Gyroid 25 unit cells model by 29.66 %, if only conduction is considered (see Table 4.15). The L_{eff} was the lowest for Gyroid TPMS model with 25 unit cells and highest for Schwarz D TPMS model with 20 unit cells.

The heat flux of the crosshatch obtained analytically was 92.143 K/W exactly what the thermal analysis in ANSYS provided. Hence, it was confirmed that the assumptions taken were correct and the results acceptable.

4.4 Computational Fluid Dynamics

The results obtained from the CFD simulations performed in ANSYS Fluent on the TPMS and other models are presented and discussed in this section. As described in Section 3.4 a simple steady state, laminar flow simulation was done with a velocity-inlet and outflow conditions. The velocity and pressure at the inlet and outlet were obtained and compared for the different models. The complete results including the velocity profiles and the continuity curves can be found in Appendix D

The Reynolds Number equation (Equation (3.9)) was used to verify that the flow systems to be analysed were laminar in nature, the Reynolds Number for the flow simulation setups are shown in Table 4.17

As can be seen from Table 4.18 the outlet velocity and pressure are comparable to a conventional model like the Cube with pipes model, used in this research. Also, there was no pressure drop across the spherical gyroid model, and the inlet and outlet velocities were comparable indicating no choking of the flow in the model. The convergence achieved for the 0.1 m/s air flow was within acceptable limit, but the convergence achieved for other conditions were not within acceptable limit. This discrepancy could be due to various reasons like the meshes used were not refined and the boundary conditions given were not exact. The continuity curves and velocity profiles are included in Appendix D.

Model	**Fluid**	ν(**kg/ms**)	**Inlet Velocity (m/s)**	**Length (m)**	**Reynolds Number**
Spherical Gyroid	Air	1.4607 x 10^{-5}	0.1	0.07	479.222
		1.4607 x 10^{-5}	0.3	0.07	1437.666
	Water	1.005 x 10^{-6}	0.01	0.07	696.52
		1.005 x 10^{-6}	0.02	0.07	1393.03
Cube with pipes	Air	1.4607 x 10^{-5}	0.1	0.07	479.222
		1.4607 x 10^{-5}	0.3	0.07	1437.666
	Water	1.005 x 10^{-6}	0.01	0.07	696.52
		1.005 x 10^{-6}	0.02	0.07	1393.03

Table 4.17: Reynolds Number for Different Velocities and Fluids for Spherical Gyroid and Cube with Pipes Models.

Model	**Fluid**	**Inlet Velocity (m/s)**	**Outlet Velocity (m/s)**	**Inlet Pressure (Pa)**	**Outlet Pressure (Pa)**
Spherical Gyroid	Air	0.1	0.1001452	101325	101325
		0.3	0.3004542	101325	101325
	Water	0.01	0.01001549	101325	101325
		0.02	0.02003065	101325	101325
Cube with pipes	Air	0.1	0.1000675	101325	101325
		0.3	0.300333	101325	101325
	Water	0.01	0.0100068	101325	101325
		0.02	0.02003623	101325	101325

Table 4.18: Velocity and Pressure Data Both at the Inlet and Outlet as Obtained from ANSYS Fluent for Spherical Gyroid and the Cube with Pipes Models.

Chapter 5

CONCLUSION

The TPMS structures like Gyroid, Schwarz D and Spherical Gyroids are self-supporting in nature, i.e. they don't require any additional supports. Due to this self-sustaining nature of the TPMS models they are mostly additively manufactured, as these structures would be very difficult to manufacture using the conventional methods.

The Gyroid TPMS model performed better in terms of the stress sustained without significant deformation. The Gyroid (10 unit cell) of 1 mm thickness gave a strain of 0.006 m/m where as the Schwarz D (10 unit cell) of 1 mm wall thickness gave a strain of 0.2 m/m, which is almost 32.33 times of the Gyroid strain. The stress v/s strain curves of the conventional random models like the solid cube were exactly as expected and same as the real stress, so the engineering stress and strain obtained from ANSYS were assumed to be acceptable and comparable to the real stress and strain. The Gyroid models have better compressive strength as compared to Schwarz D and can sustain larger loads and stresses before they deform significantly. The TPMS can be used for high load and high stress applications as they are both light and strong.

The Gyroid (25 unit cell) TPMS model had the lowest thermal resistance (K/W) as can be seen in **??** of 32.016 where as even the solid cube had a thermal resistance of 55.37 K/W, which is almost 73% more than the Gyroid (25 unit cell) thermal Resistance. The Schwarz D (25 unit cell) had a thermal resistance of 76.662, almost 1.4 times of the Gyroid (25 unit cell). The Gyroid (25 unit cell) had the lowest L_{eff} of, and hence has the least thermal resistance and the best option for heat conduction

applications. The Schwarz D (20 unit cell) had the highest L_{eff}, hence the highest thermal resistance and the best option for insulation applications.

The flow through the TPMS model, the Spherical Gyroid was very comparable to the conventional model of Cube with pipes, the inlet and outlet velocities didn't vary a lot, specifically within .15% of the inlet velocity for air and water flow. The conventional model has less deviation than Spherical Gyroid for 0.1 m/s and 0.01 m/s velocities and were within 0.07% of each other and for 0.3 m/s and 0.02 m/s flow velocities they were within .18% of each other. It can be understood from this that the flow through the TPMS Spherical Gyroid was more consistent than the Cube with pipes model. Hence, these TPMS models can be used for applications which requires air or fluid flow through them like heat sink applications in microchip packaging or electronics packaging.

Chapter 6

FUTURE WORK

Firstly in this thesis only the compressive strength of the Gyroid and Schwarz D TPMS models was studied. A better understanding of the mechanical properties could be achieved if a tensile strength could be studied. Also, instead of only studying the Gyroid and the Schwarz D TPMS models, other models like the Schwarz P, Schwarz H and Neovius structure could be studied as well, and the properties of each compared. That could provide a better understanding of the mechanical behaviour of these TPMS, and help us understand how they behave under various load and stress distributions.

Secondly a better comparison of the thermal properties could be made if convection and radiation could be considered along with conduction. Also, if a heat flux input instead of a simple temperature difference was given as input, a better understanding of the thermal behaviour of these TPMS models could be achieved. If a forced convection study of these models could be made along with the simple flow simulation, a better and more informed decision could be made. A turbulent flow analysis also, would help us to understand these structures better.

An experimental study can be conducted in accordance with the FEA and CFD simulations and the results could be compared. This would help us understand the various unknown variables and the unknown assumptions that ANSYS and other FEA software packages make.

Another important aspect that could be studied is to design the existing the models used in the industry like the wing of a car, or a heat sink used in a laptop with these TPMS structures. Such designs would be of very high demand and importance

in many modern industries. If experimental and FEA simulations of such designs were performed and their mechanical and thermal performance studied and compared to the conventional designs, it would help us understand these structures better and a more informed decision on whether the conventional models can be replaced with these TPMS optimized design.

BIBLIOGRAPHY

[1] "Fused deposition modelling (fdm) printers by makerbot industries - makerbot replicator+", URL https://store.makerbot.com/3d-printers/printers/replicator/bundles/rep/ (2019).

[2] Abueidda, D. W., M. Elhebeary, C.-S. A. Shiang, S. Pang, R. K. A. Al-Rub and I. M. Jasiuk, "Mechanical properties of 3d printed polymeric gyroid cellular structures: Experimental and finite element study", Materials & Design **165**, 107597 (2019).

[3] Abueidda, D. W., F. A. Sabet and I. M. Jasiuk, "Modeling of stiffness and strength of bone at nanoscale", Journal of biomechanical engineering **139**, 5, 051006 (2017).

[4] Anderson, J. D. and J. Wendt, *Computational fluid dynamics*, vol. 206 (Springer, 1995).

[5] Ashby, M., "The properties of foams and lattices", Philosophical Transactions of the Royal Society A: Mathematical, Physical and Engineering Sciences **364**, 1838, 15–30 (2005).

[6] Ashby, M. F., H. Shercliff and D. Cebon, *Materials: engineering, science, processing and design* (Butterworth-Heinemann, 2018).

[7] Ashley, S., "Rapid prototyping systems", Mechanical Engineering-CIME **113**, 4, 34–36 (1991).

[8] Cooper, K., *Rapid prototyping technology: selection and application* (CRC press, 2001).

[9] Darboux, G., *Leçons sur la théorie générale des surfaces et les applications géométriques du calcul infinitesimal: Généralités, coordonées curvilignes, surfaces minima* (Gauthier Villars, 1887).

[10] Deshpande, V. S., N. A. Fleck and M. F. Ashby, "Effective properties of the octet-truss lattice material", Journal of the Mechanics and Physics of Solids **49**, 8, 1747–1769 (2001).

[11] Do Carmo, M. P., *Differential Geometry of Curves and Surfaces: Revised and Updated Second Edition* (Courier Dover Publications, 2016).

[12] Elliott, O., S. Gray, M. McClay, B. Nassief, A. Nunnelley, E. Vogt, J. Ekong, K. Kardel, A. Khoshkhoo, G. Proaño *et al.*, "Design and manufacturing of high surface area 3d-printed media for moving bed bioreactors for wastewater treatment", Journal of Contemporary Water Research & Education **160**, 1, 144–156 (2017).

[13] Fleck, N., V. Deshpande and M. Ashby, "Micro-architectured materials: past, present and future", Proceedings of the Royal Society A: Mathematical, Physical and Engineering Sciences **466**, 2121, 2495–2516 (2010).

[14] Gandy, P. J. and J. Klinowski, "Exact computation of the triply periodic g (gyroid') minimal surface", Chemical Physics Letters **321**, 5-6, 363–371 (2000).

[15] Gibson, L. J., "Biomechanics of cellular solids", Journal of biomechanics **38**, 3, 377–399 (2005).

[16] Gibson, L. J. and M. F. Ashby, *Cellular solids: structure and properties* (Cambridge university press, 1999).

[17] Guerdat, T. C., T. M. Losordo, J. J. Classen, J. A. Osborne and D. P. DeLong, "An evaluation of commercially available biological filters for recirculating aquaculture systems", Aquacultural engineering **42**, 1, 38–49 (2010).

[18] Hertzberg, R., "Deformation and fracture mechanics of engineering materials. usa: John willey & sons", (1996).

[19] Khaderi, S., V. Deshpande and N. Fleck, "The stiffness and strength of the gyroid lattice", International Journal of Solids and Structures **51**, 23-24, 3866–3877 (2014).

[20] Krödel, S., T. Delpero, A. Bergamini, P. Ermanni and D. M. Kochmann, "3 d auxetic microlattices with independently controllable acoustic band gaps and quasi-s tatic elastic moduli", Advanced Engineering Materials **16**, 4, 357–363 (2014).

[21] Kruth, J.-P., "Material incress manufacturing by rapid prototyping techniques", CIRP annals **40**, 2, 603–614 (1991).

[22] Li, D., W. Liao, N. Dai, G. Dong, Y. Tang and Y. M. Xie, "Optimal design and modeling of gyroid-based functionally graded cellular structures for additive manufacturing", Computer-Aided Design **104**, 87–99 (2018).

[23] Madenci, E. and I. Guven, *The finite element method and applications in engineering using ANSYS®* (Springer, 2015).

[24] Moatamedi, M. and H. A. Khawaja, *Finite Element Analysis* (CRC Press, 2018).

[25] Noorani, R., *Rapid prototyping: principles and applications* (John Wiley & Sons Incorporated, 2006).

[26] Ødegaard, H., B. Gisvold and J. Strickland, "The influence of carrier size and shape in the moving bed biofilm process", Water Science and Technology **41**, 4-5, 383–391 (2000).

[27] Pfeiffer, T. J. and P. S. Wills, "Evaluation of three types of structured floating plastic media in moving bed biofilters for total ammonia nitrogen removal in a low salinity hatchery recirculating aquaculture system", Aquacultural engineering **45**, 2, 51–59 (2011).

[28] Rashed, M., M. Ashraf, R. Mines and P. J. Hazell, "Metallic microlattice materials: A current state of the art on manufacturing, mechanical properties and applications", Materials & Design **95**, 518–533 (2016).

[29] Schoen, A. H., "Infinite periodic minimal surfaces without self-intersections", (1970).

[30] Stolarski, T., Y. Nakasone and S. Yoshimoto, *Engineering analysis with ANSYS software* (Butterworth-Heinemann, 2018).

[31] Ullah, I., J. Elambasseril, M. Brandt and S. Feih, "Performance of bio-inspired kagome truss core structures under compression and shear loading", Composite Structures **118**, 294–302 (2014).

[32] Valdevit, L., A. J. Jacobsen, J. R. Greer and W. B. Carter, "Protocols for the optimal design of multi-functional cellular structures: from hypersonics to micro-architected materials", Journal of the American Ceramic Society **94**, s15–s34 (2011).

[33] White, F. M., *Fluid mechanics* (McGraw-Hill Book Company, New York, 1986).

[34] Wohlgemuth, M., N. Yufa, J. Hoffman and E. L. Thomas, "Triply periodic bicontinuous cubic microdomain morphologies by symmetries", Macromolecules **34**, 17, 6083–6089 (2001).

[35] Wong, K. V. and A. Hernandez, "A review of additive manufacturing", ISRN Mechanical Engineering **2012** (2012).

[36] Xiong, J., R. Mines, R. Ghosh, A. Vaziri, L. Ma, A. Ohrndorf, H.-J. Christ and L. Wu, "Advanced micro-lattice materials", Advanced Engineering Materials **17**, 9, 1253–1264 (2015).

APPENDIX A

MATLAB CODE FOR CALCULATING AREA OF CROSS-SECTION

The MATLAB code that was used to calculate the cross-sectional area of the TPMS models is shown below.

```
clc
srcFile=dir('<Path to your BMP Files>\*.bmp');
percentageBlack=zeros(1,length(srcFile));
sum=0;
for i=1:length(srcFile)
    filename=strcat('<Path to your BMP Files>\',srcFile(i).
        name);
    I=imread(filename);
    percentageBlack(1,i)=((1-nnz(I)/numel(I)));
    sum=sum+percentageBlack(1,i);
end

sum_avg=sum/length(srcFile)
area=sum_avg*70*70
```

APPENDIX B

COMPLETE RESULTS OF THE COMPRESSIVE STRENGTH ANALYSIS OF THE TPMS MODELS PERFORMED USING ANSYS 19.2.

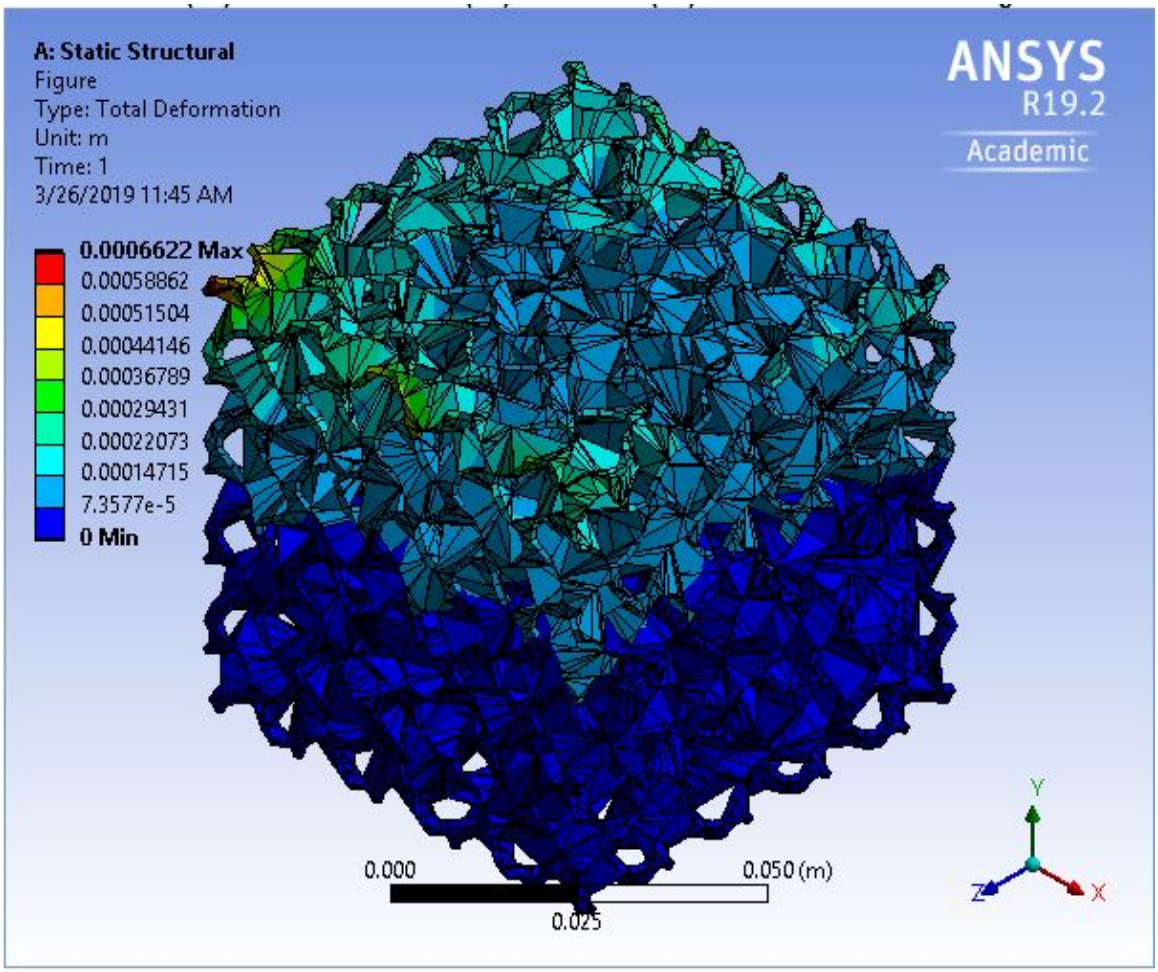

Figure B.1: Total Deformation of the Gyroid (10 Unit Cell) of 1 mm Wall Thickness under 100 kN of Load as Obtained from ANSYS 19.2. .

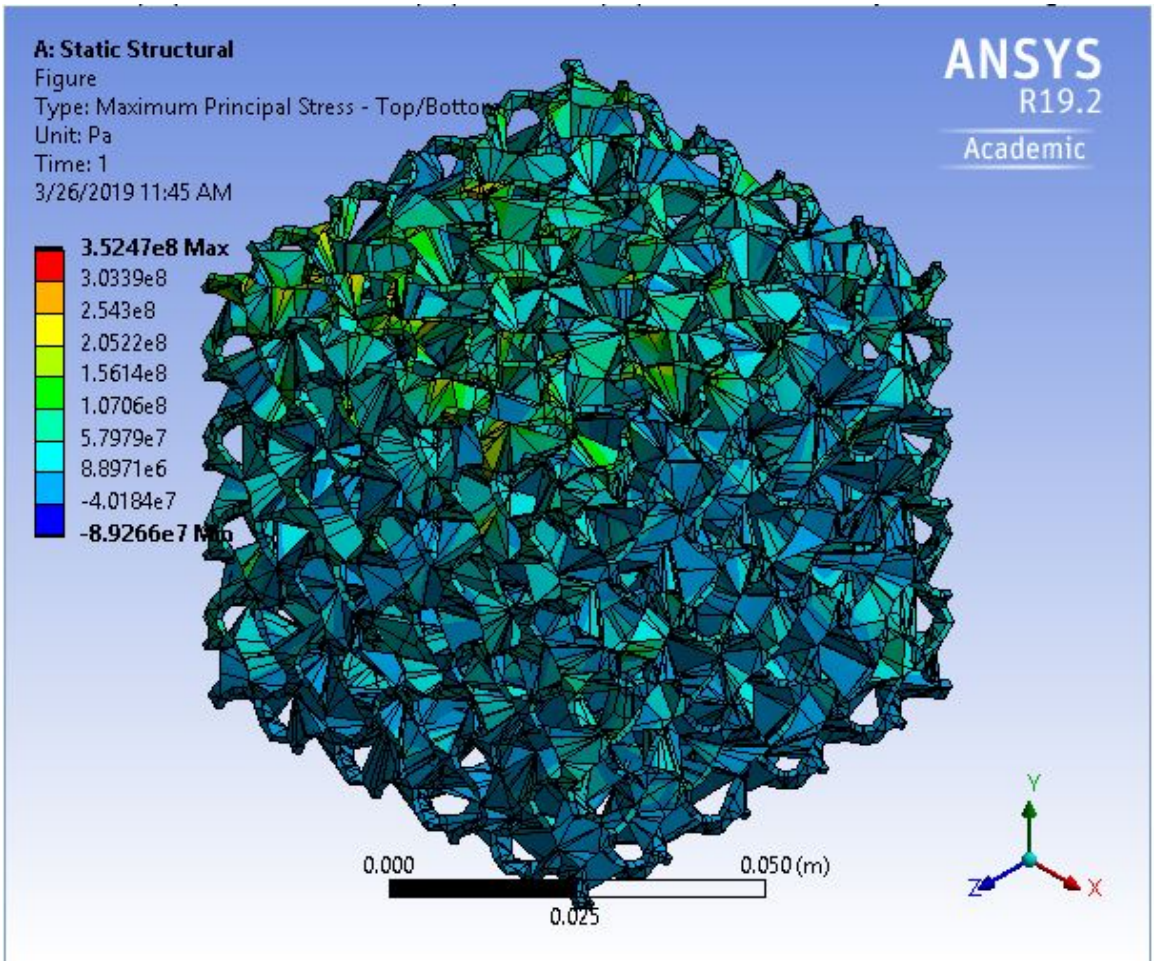

Figure B.2: Maximum Principal Stress of the Gyroid (10 Unit Cell) of 1 mm Wall Thickness under 100 kN of Load as Obtained from ANSYS 19.2 .

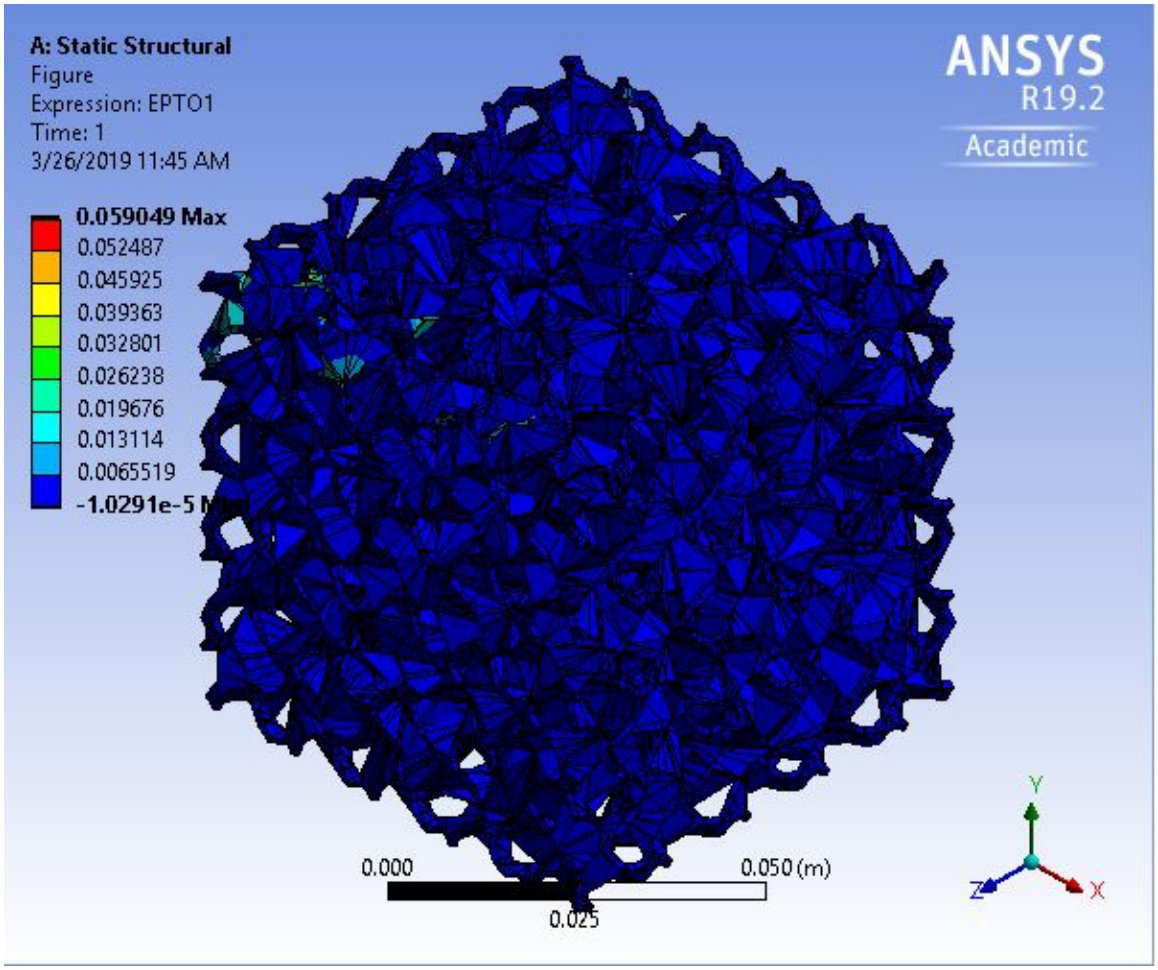

Figure B.3: The User Defined Result of EPTO as Explained in **??** of the Gyroid (10 Unit Cell) of 1 mm Wall Thickness under 100 kN of Load as Obtained from ANSYS 19.2.

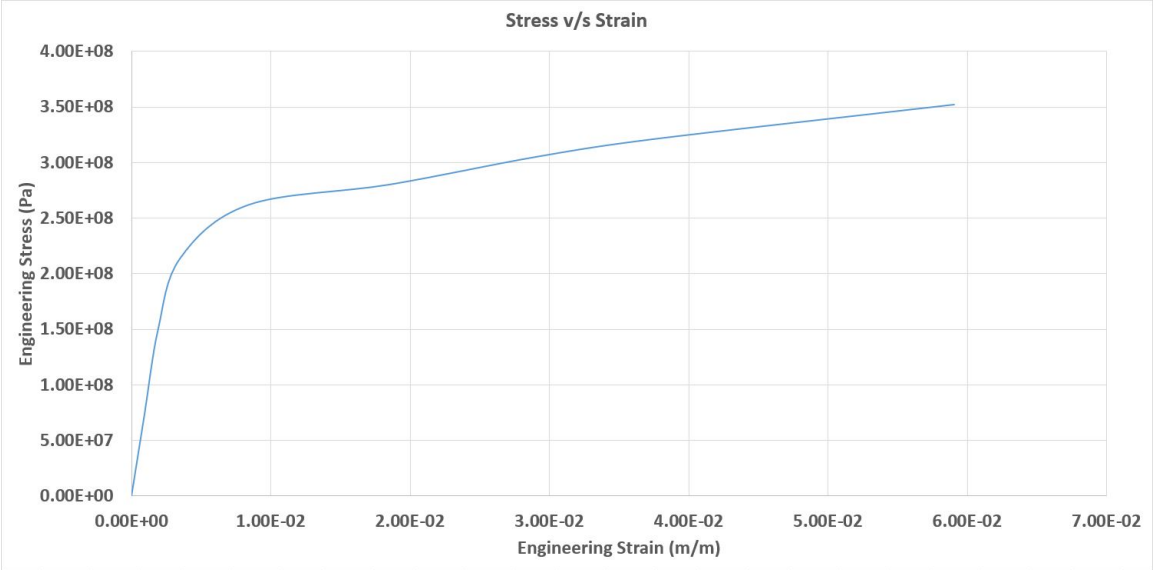

Figure B.4: The Engineering Stress V/S Engineering Strain of the Gyroid (10 Unit Cell) of 1 mm Wall Thickness under 100 kN of Load as Obtained from ANSYS 19.2.

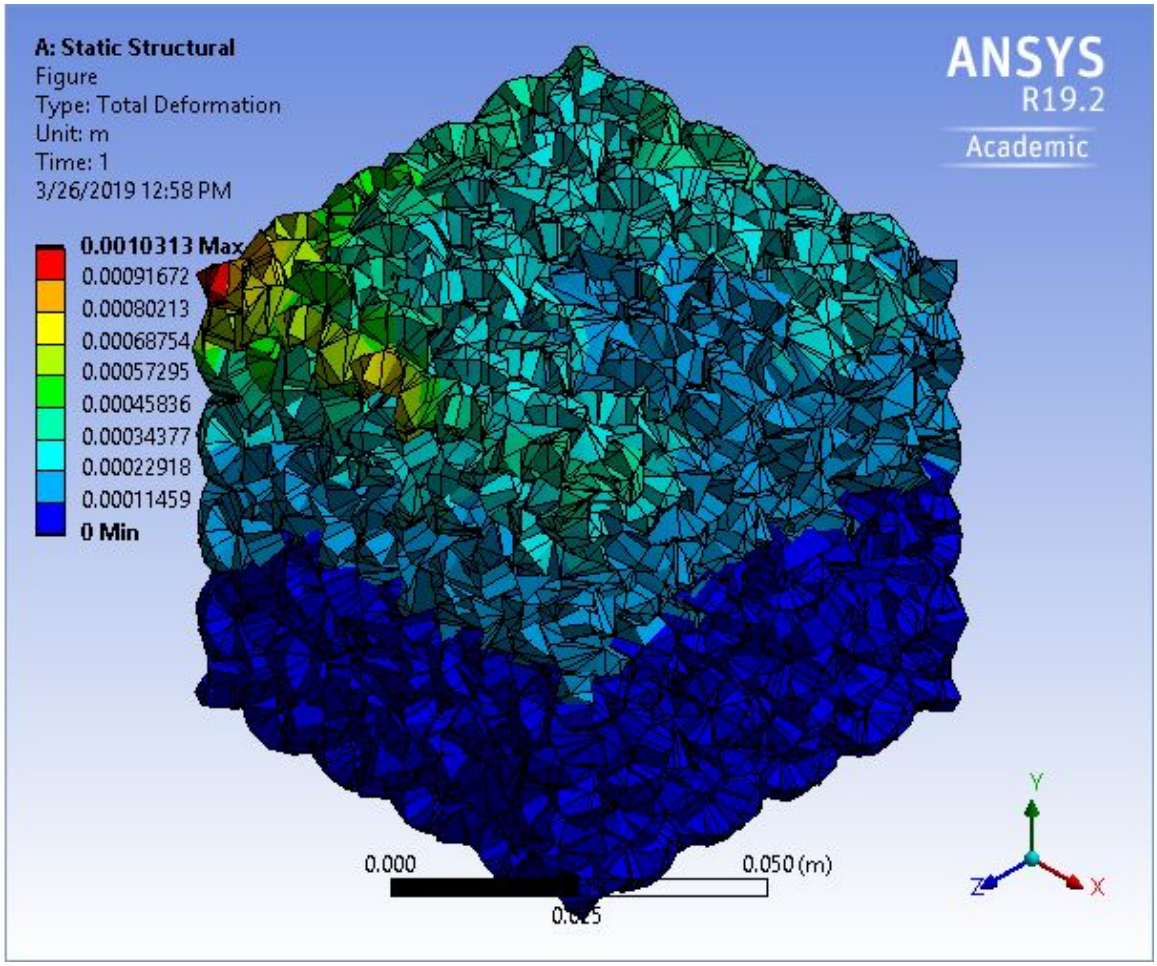

Figure B.5: Total Deformation of the Gyroid (10 Unit Cell) of 5 mm Wall Thickness under 1 MN of Load as Obtained from ANSYS 19.2.

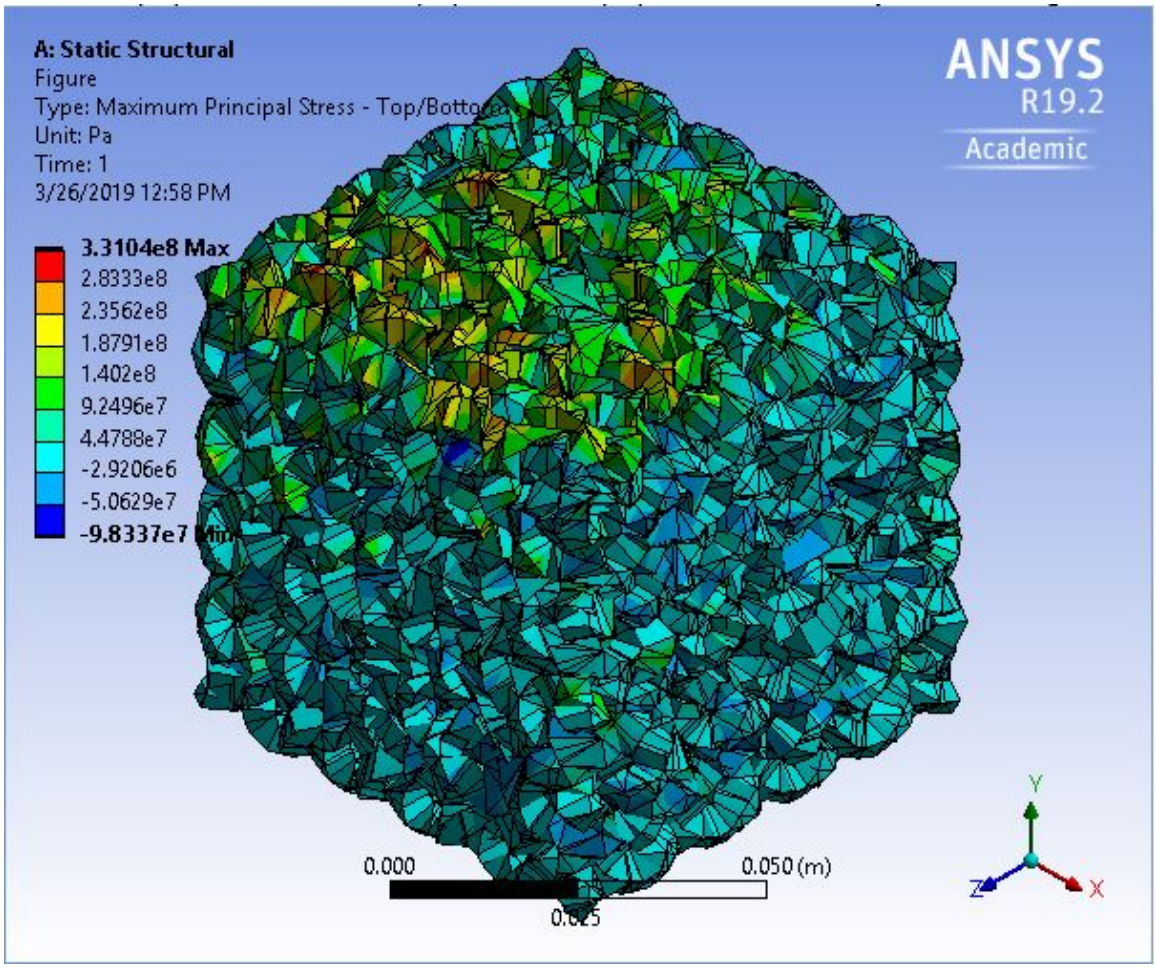

Figure B.6: Maximum Principal Stress of the Gyroid (10 Unit Cell) of 5 mm Wall Thickness under 1 MN of Load as Obtained from ANSYS 19.2.

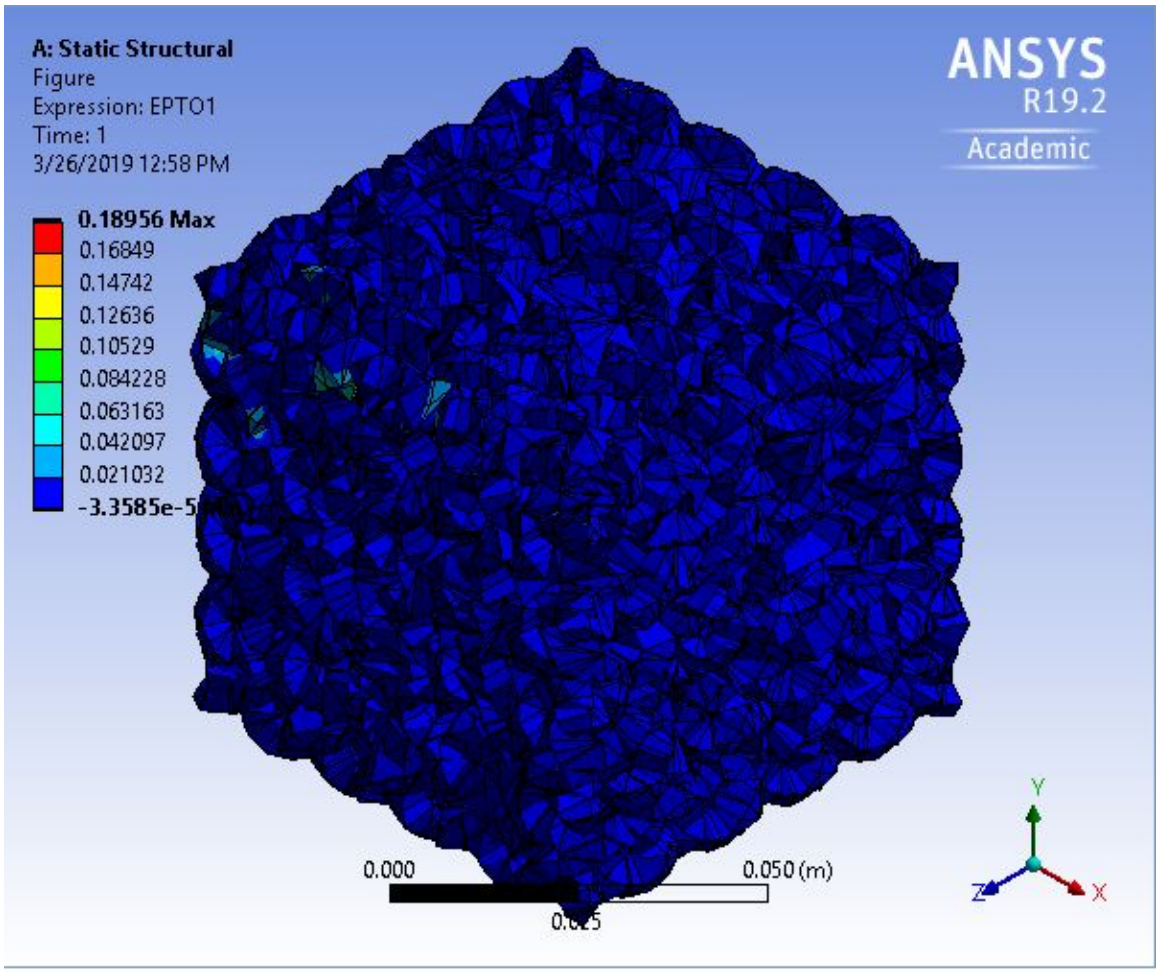

Figure B.7: The User Defined Result of EPTO as Explained in Section 3.3.1 of the Gyroid (10 Unit Cell) of 5 mm Wall Thickness under 1 MN of Load as Obtained from ANSYS 19.2.

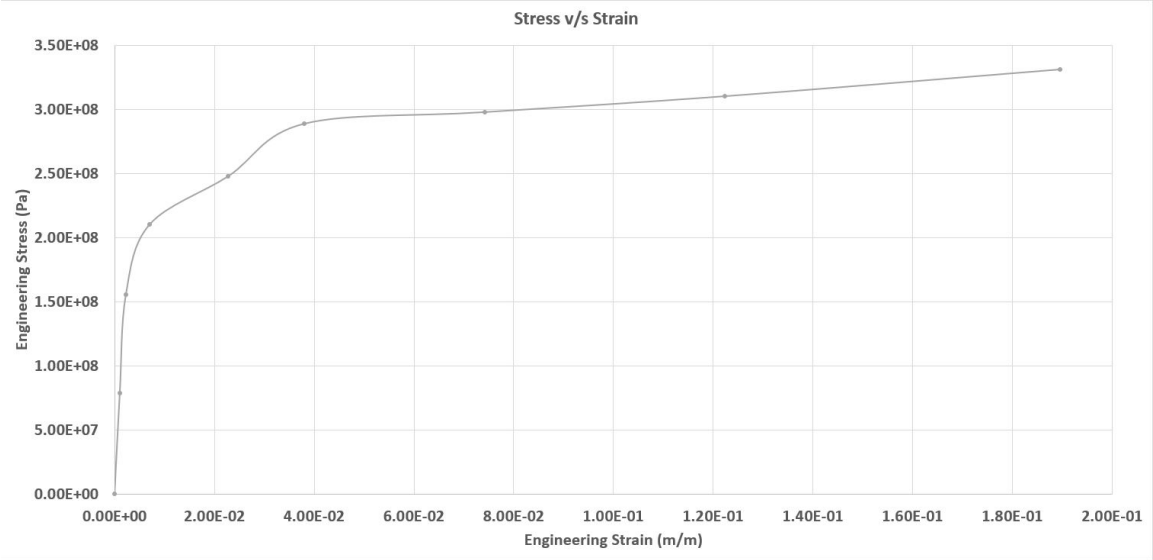

Figure B.8: The Engineering Stress v/s Engineering Strain of the Gyroid (10 Unit Cell) of 5 mm Wall Thickness under 1 MN of Load as Obtained from ANSYS 19.2.

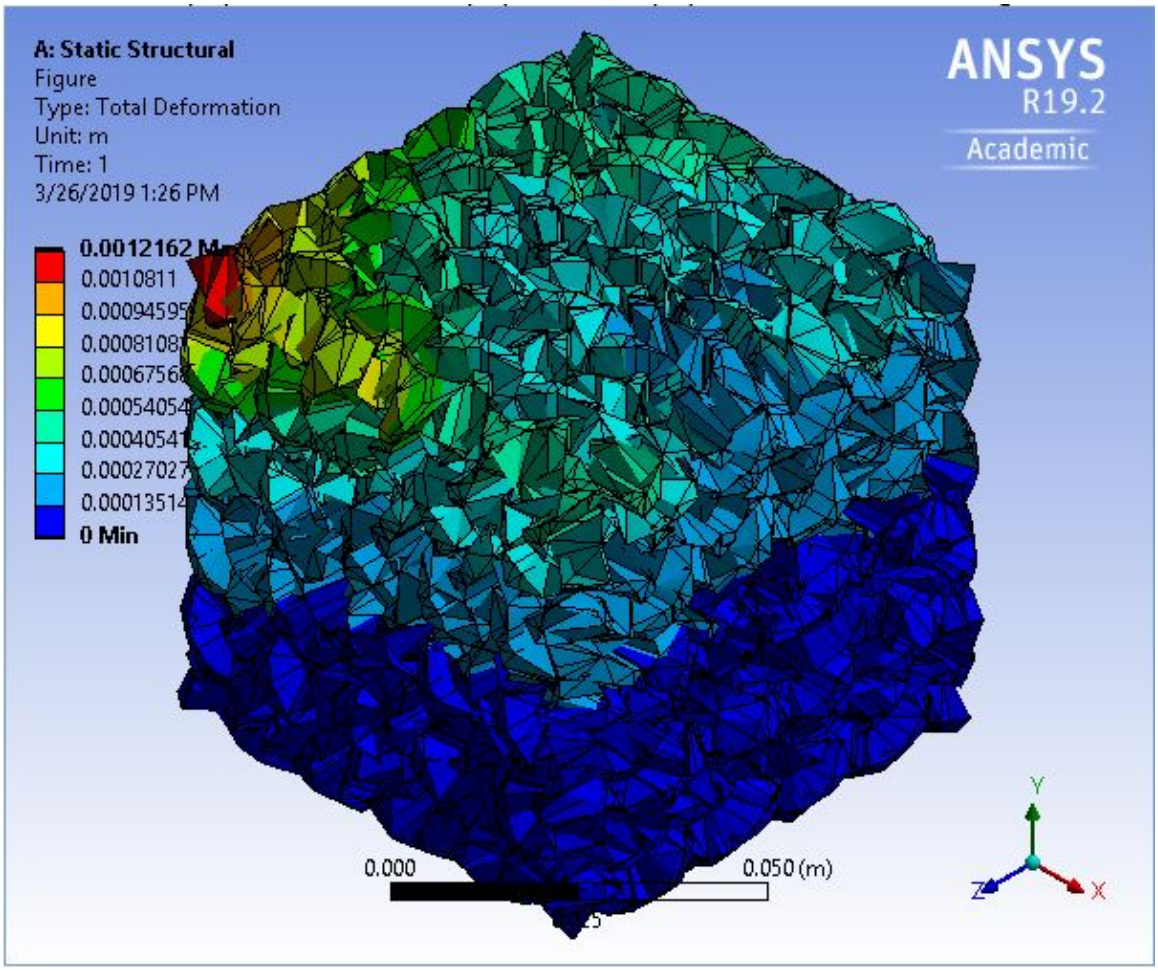

Figure B.9: Total Deformation of the Gyroid (10 Unit Cell) of 1 cm Wall Thickness under 2.5 MN of Load as Obtained from ANSYS 19.2.

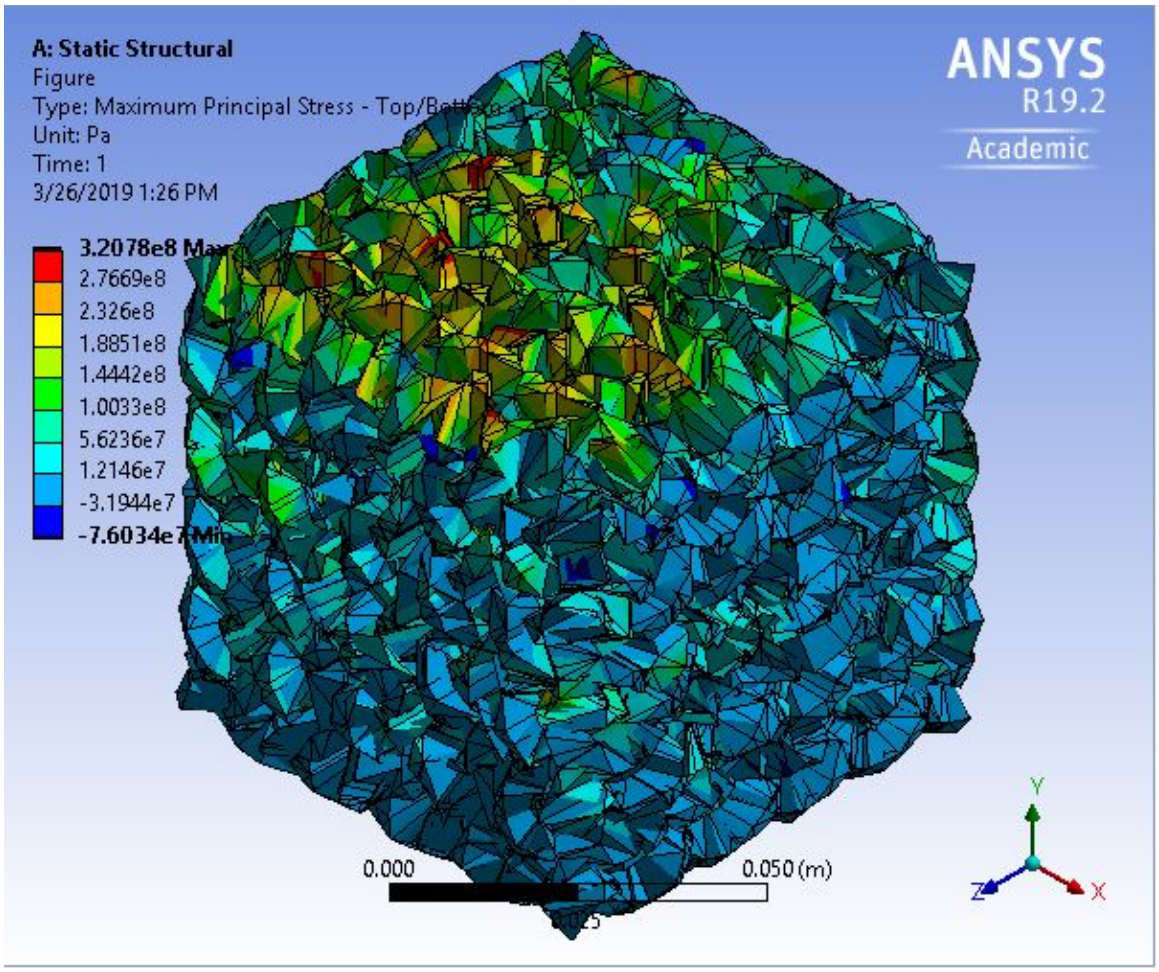

Figure B.10: Maximum Principal Stress of the Gyroid (10 Unit Cell) of 1 cm Wall Thickness under 2.5 MN of Load as Obtained from ANSYS 19.2.

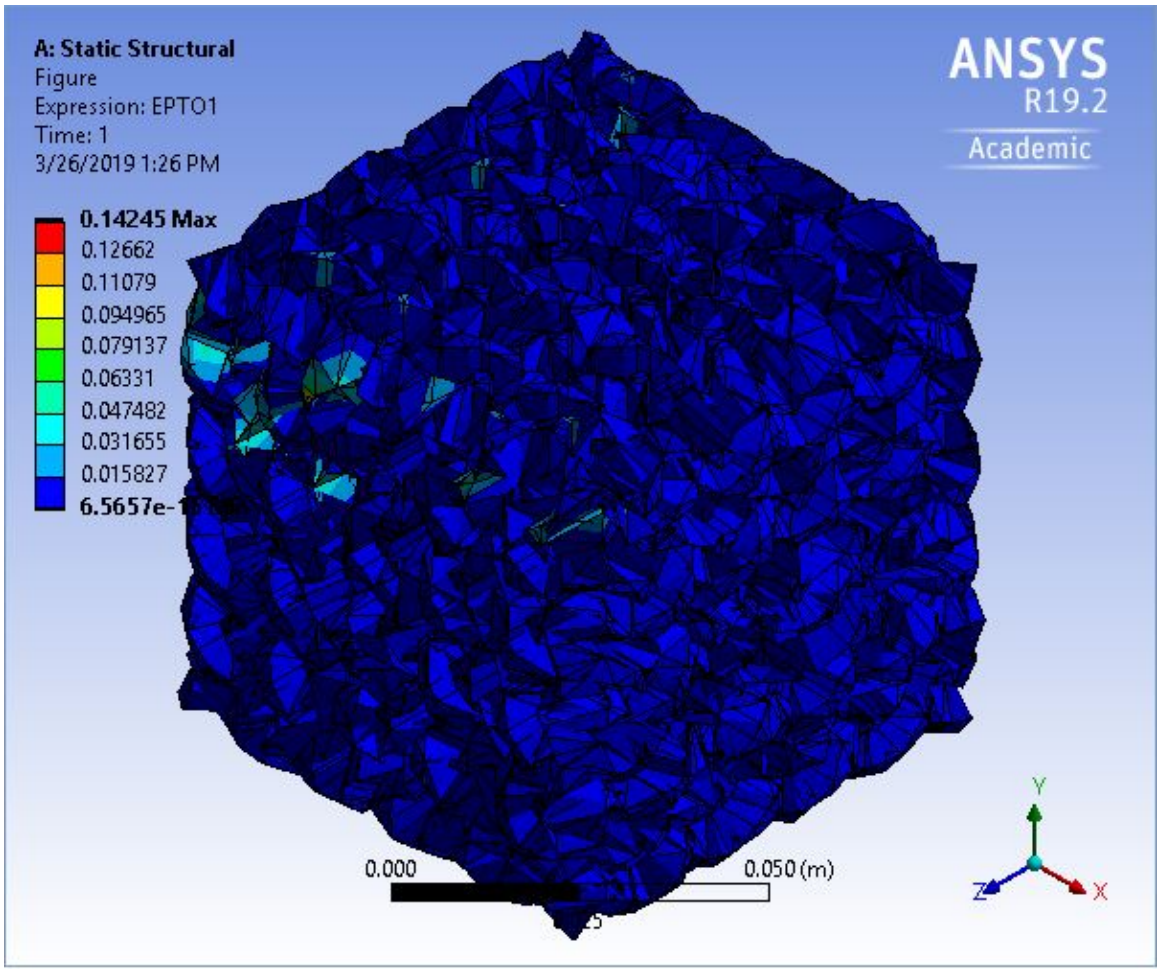

Figure B.11: The User Defined Result of EPTO as Explained in Section 3.3.1 of the Gyroid (10 Unit Cell) of 1 cm Wall Thickness under 2.5 MN of Load as Obtained from ANSYS 19.2.

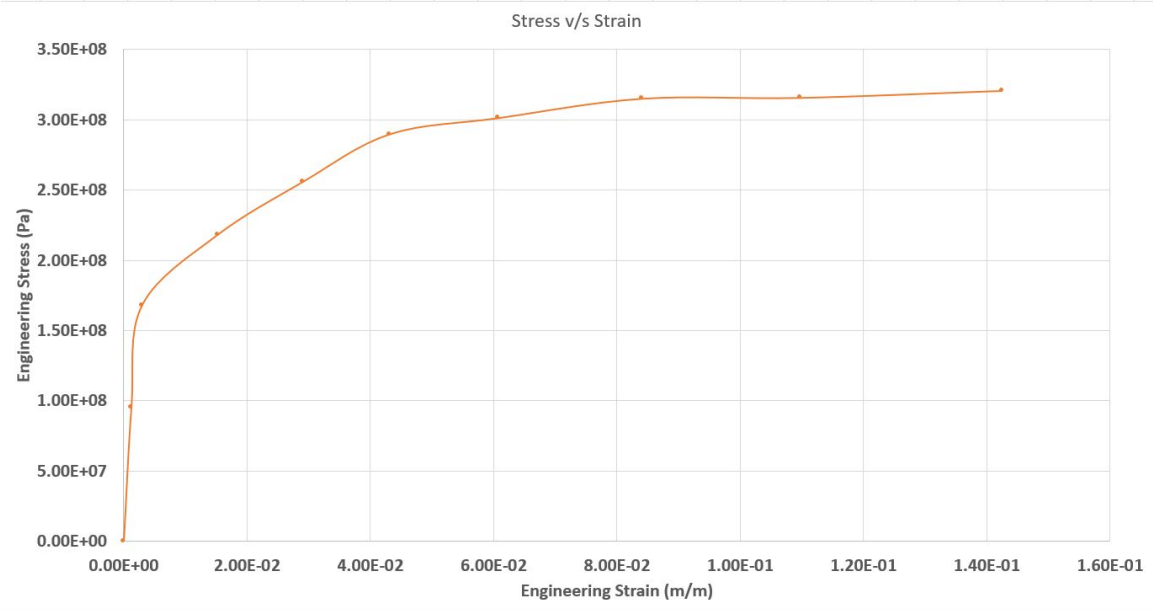

Figure B.12: The Engineering Stress v/s Engineering Strain of the Gyroid (10 Unit Cell) of 1 cm Wall Thickness under 2.5 MN of Load as Obtained from ANSYS 19.2.

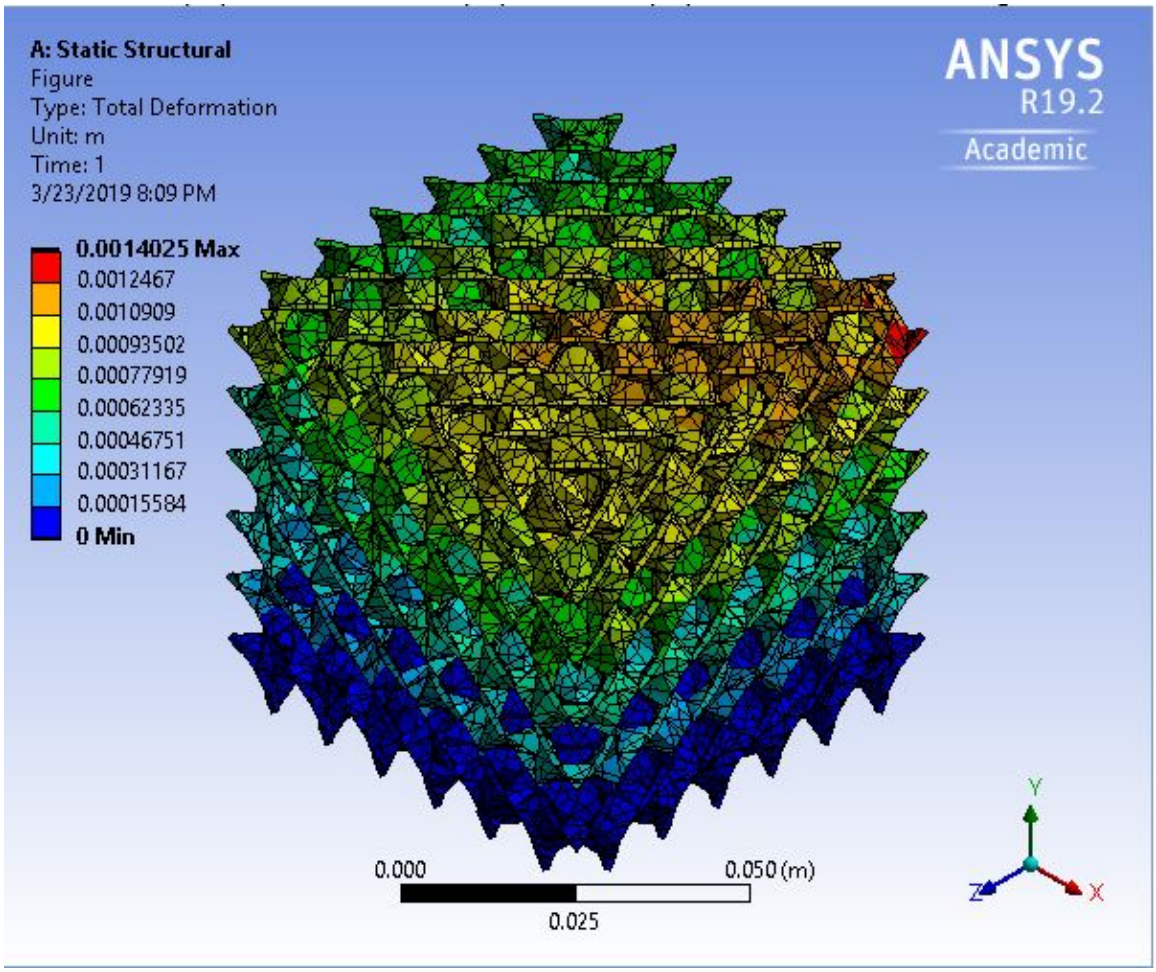

Figure B.13: Total Deformation of the Schwarz D (10 Unit Cell) of 1 mm Wall Thickness under 135 kN of Load as Obtained from ANSYS 19.2.

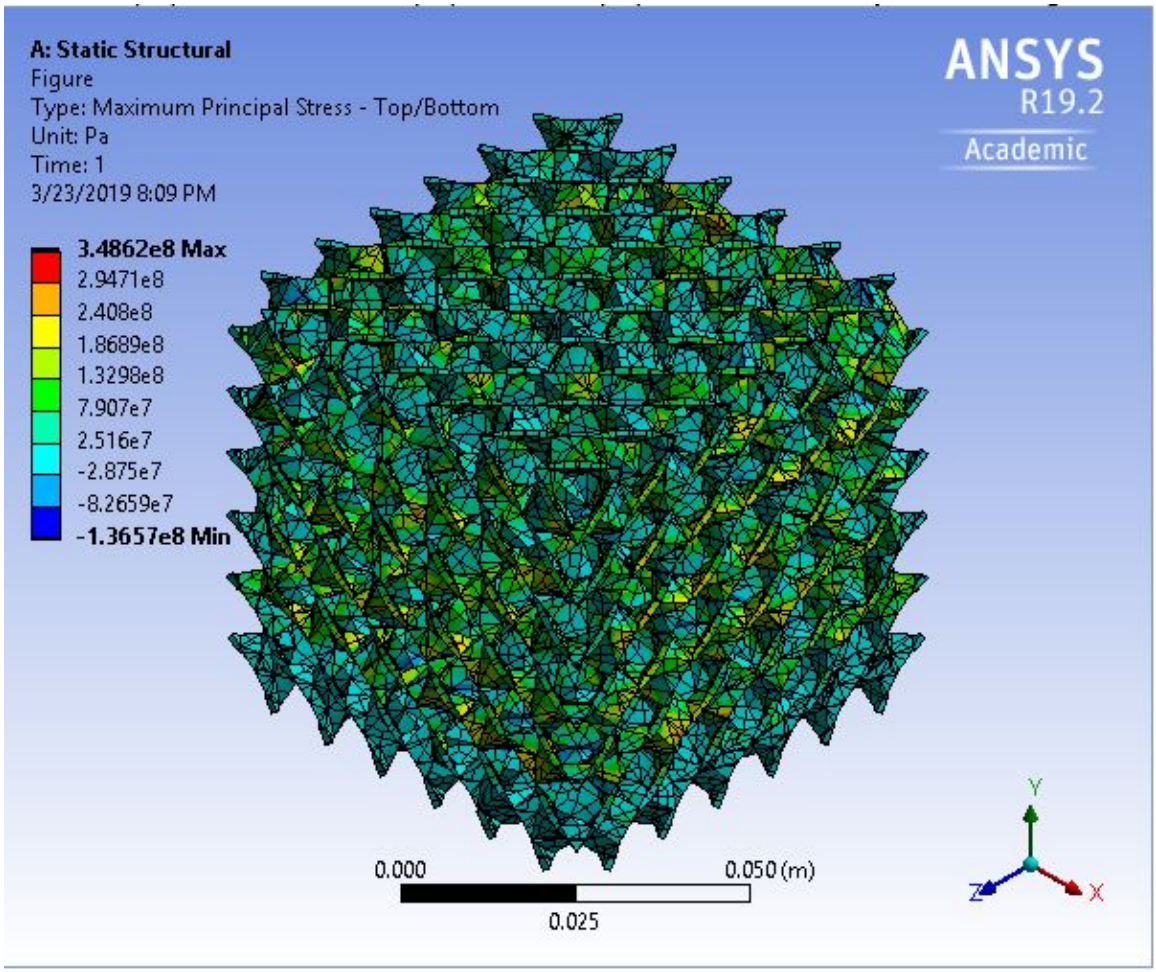

Figure B.14: Maximum Principal Stress of the Schwarz D (10 Unit Cell) of 1 mm Wall Thickness under 135 kN of Load as Obtained from ANSYS 19.2.

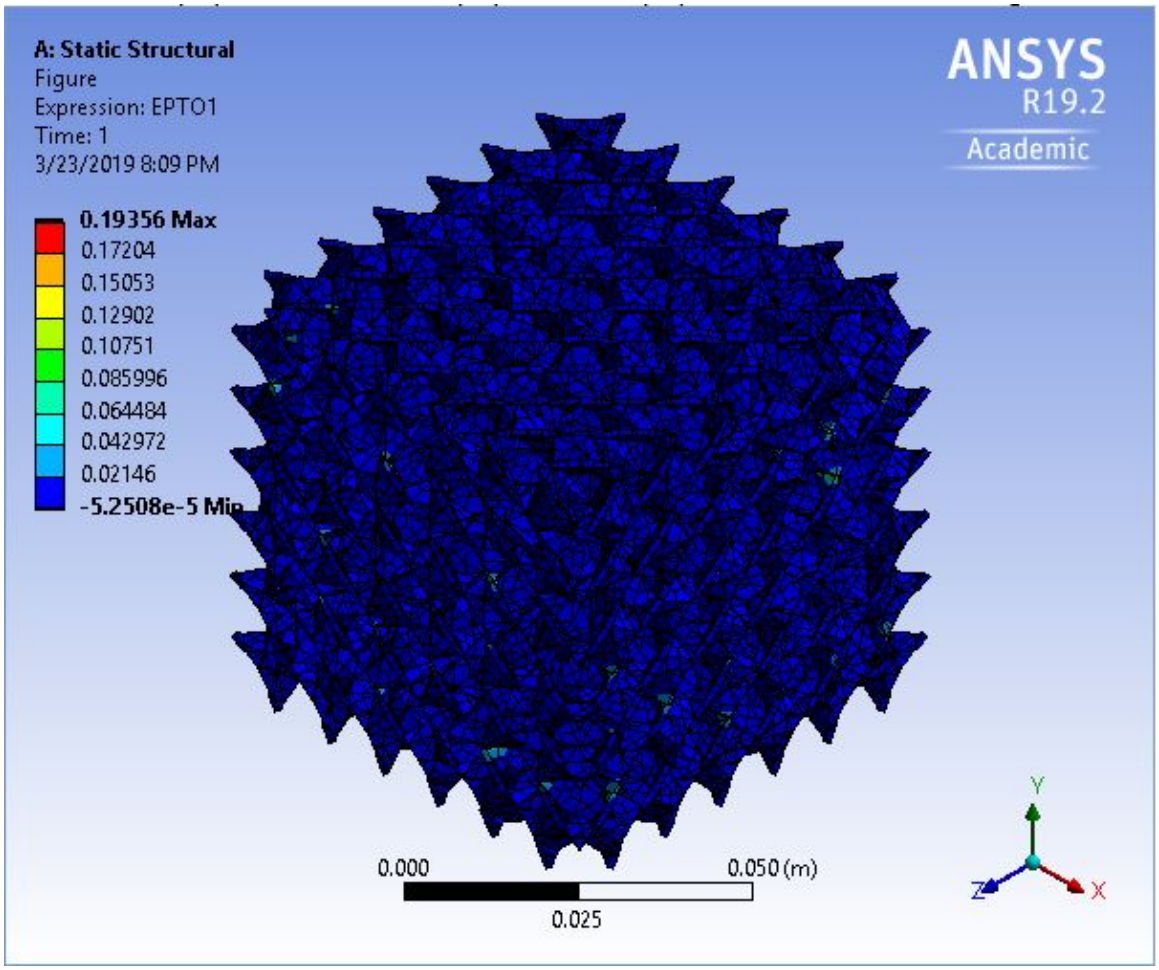

Figure B.15: The User Defined Result of EPTO as Explained in Section 3.3.1 of the Schwarz D (10 Unit Cell) of 1 mm Wall Thickness under 135 kN of Load as Obtained from ANSYS 19.2.

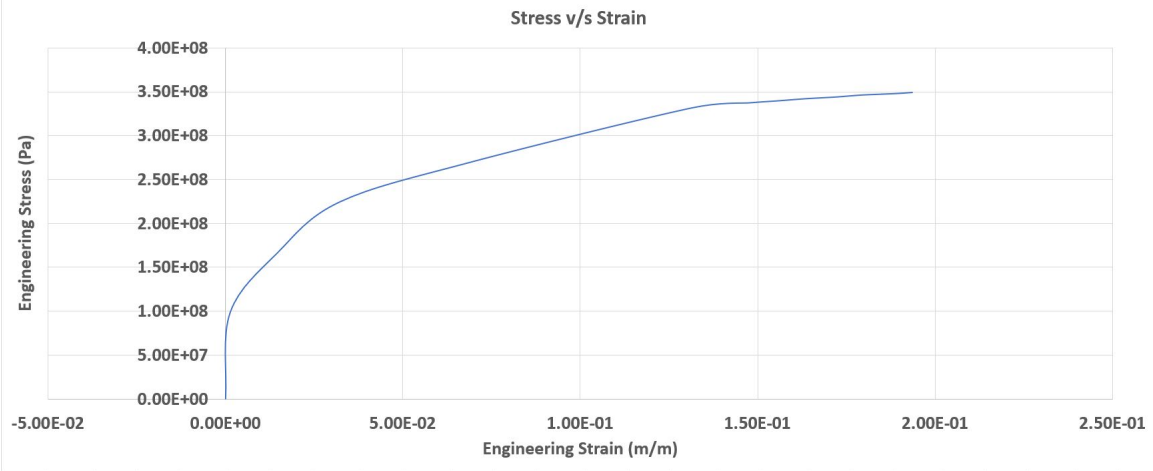

Figure B.16: The Engineering Stress v/s Engineering Strain of the Schwarz D (10 Unit Cell) of 1 mm Wall Thickness under 135 kN of Load as Obtained from ANSYS 19.2.

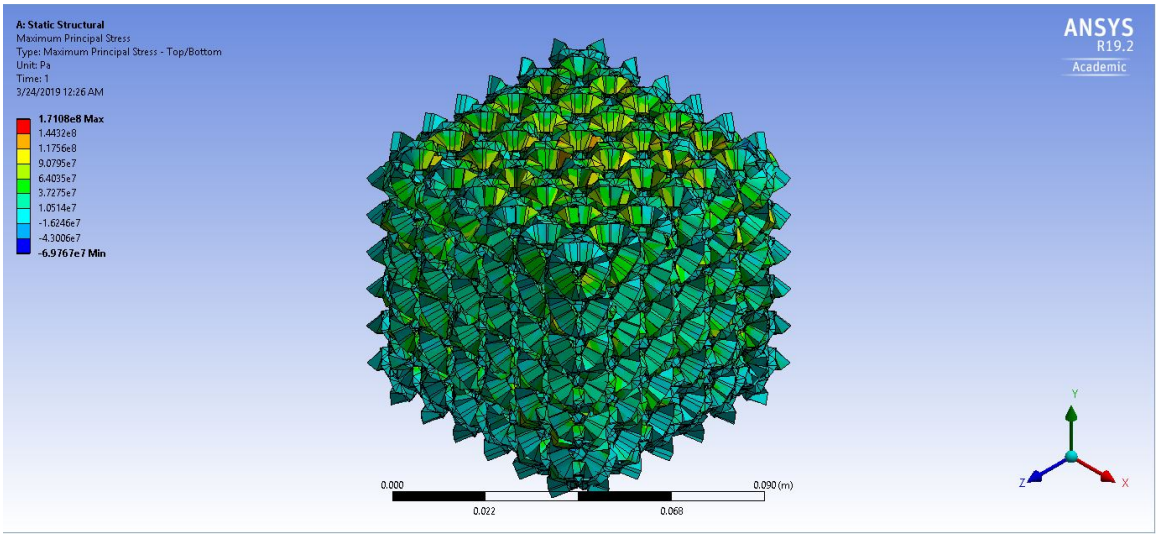

Figure B.17: Maximum Principal Stress of the Schwarz D (10 Unit Cell) of 5 mm Wall Thickness under 500 kN of Load as Obtained from ANSYS 19.2.

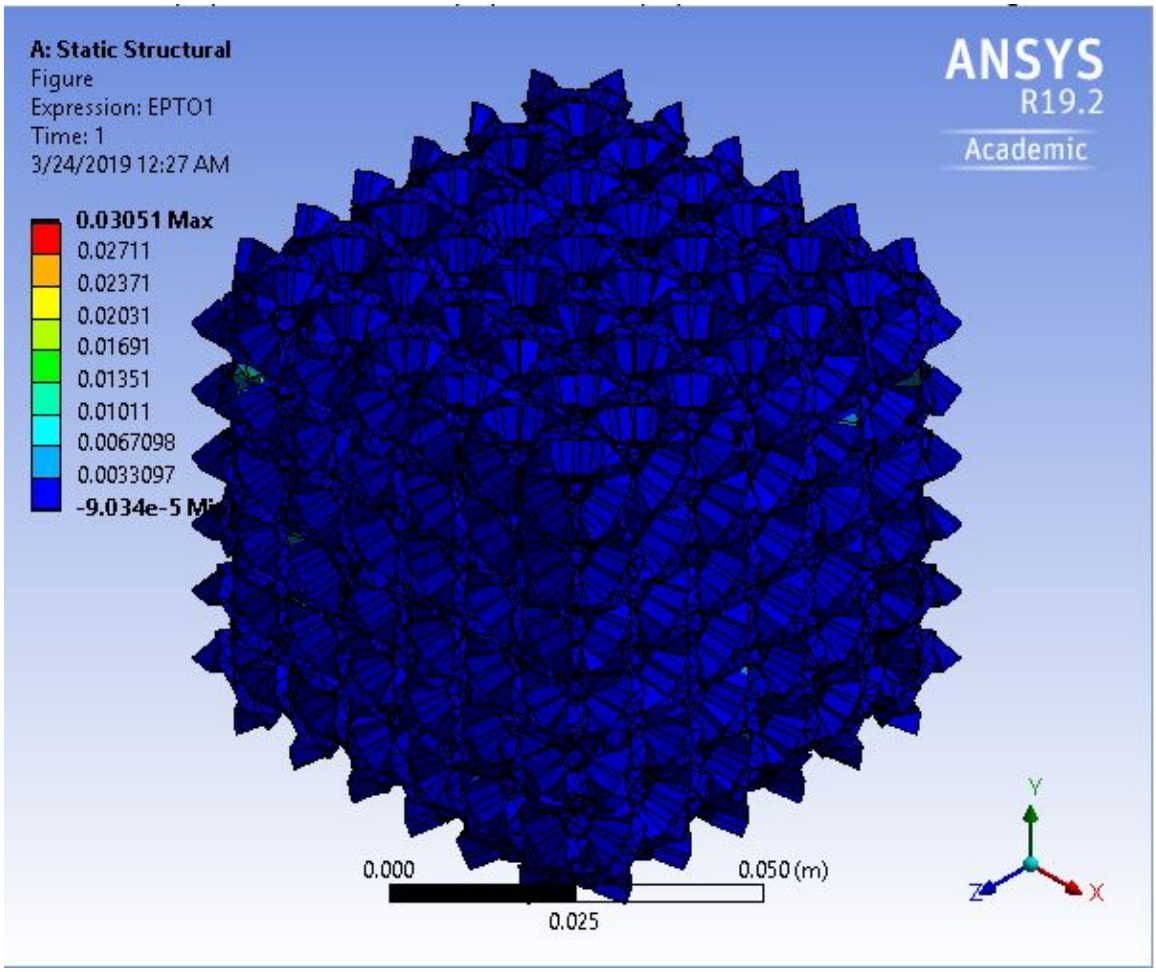

Figure B.18: The User Defined Result of EPTO as Explained in Section 3.3.1 of the Schwarz D (10 Unit Cell) of 5 mm Wall Thickness under 500 kN of Load as Obtained from ANSYS 19.2.

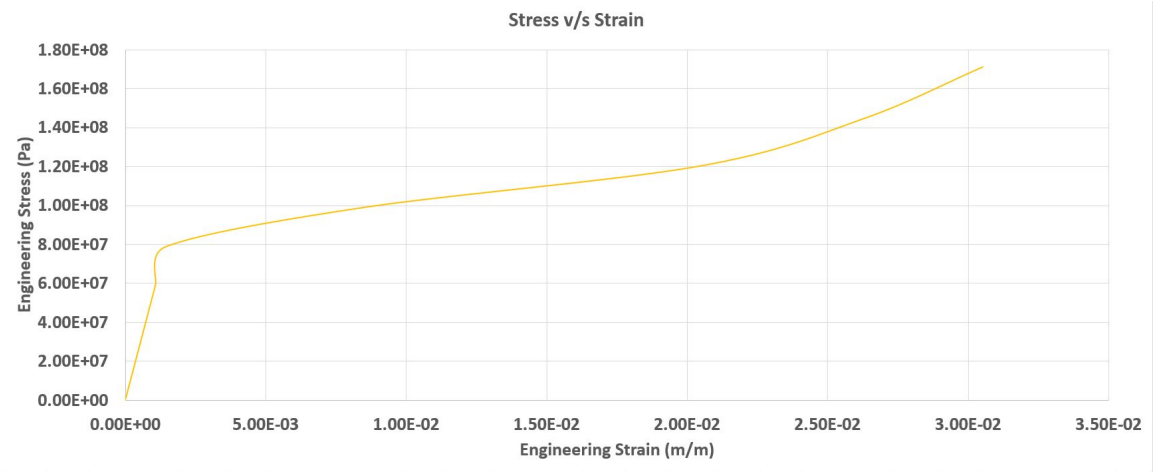

Figure B.19: The Engineering Stress v/s engineering Strain of the Schwarz D (10 Unit Cell) of 5 mm Wall Thickness under 500 kN of Load as Obtained from ANSYS 19.2.

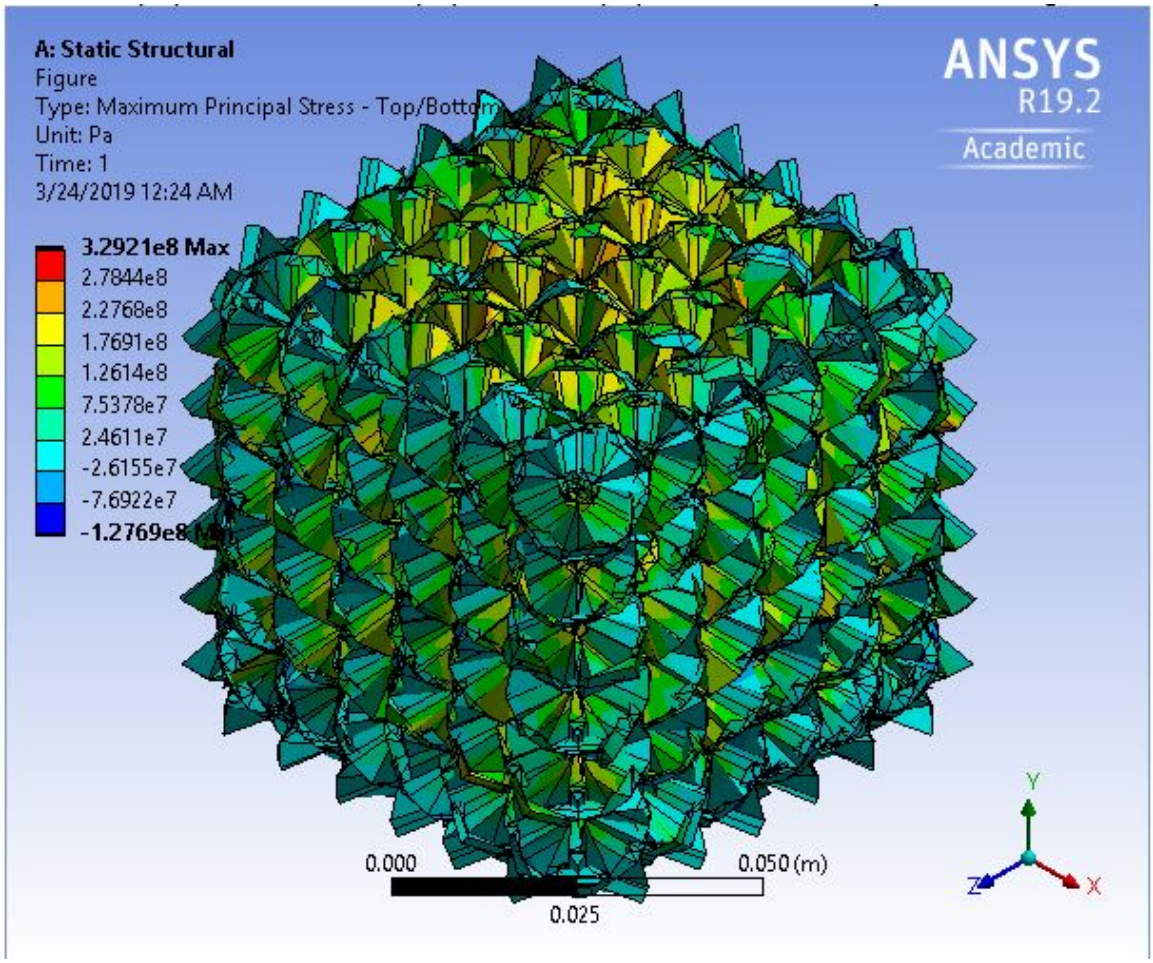

Figure B.20: Maximum Principal Stress of the Schwarz D (10 Unit Cell) of 1 cm Wall Thickness under 2 MN of Load as Obtained from ANSYS 19.2.

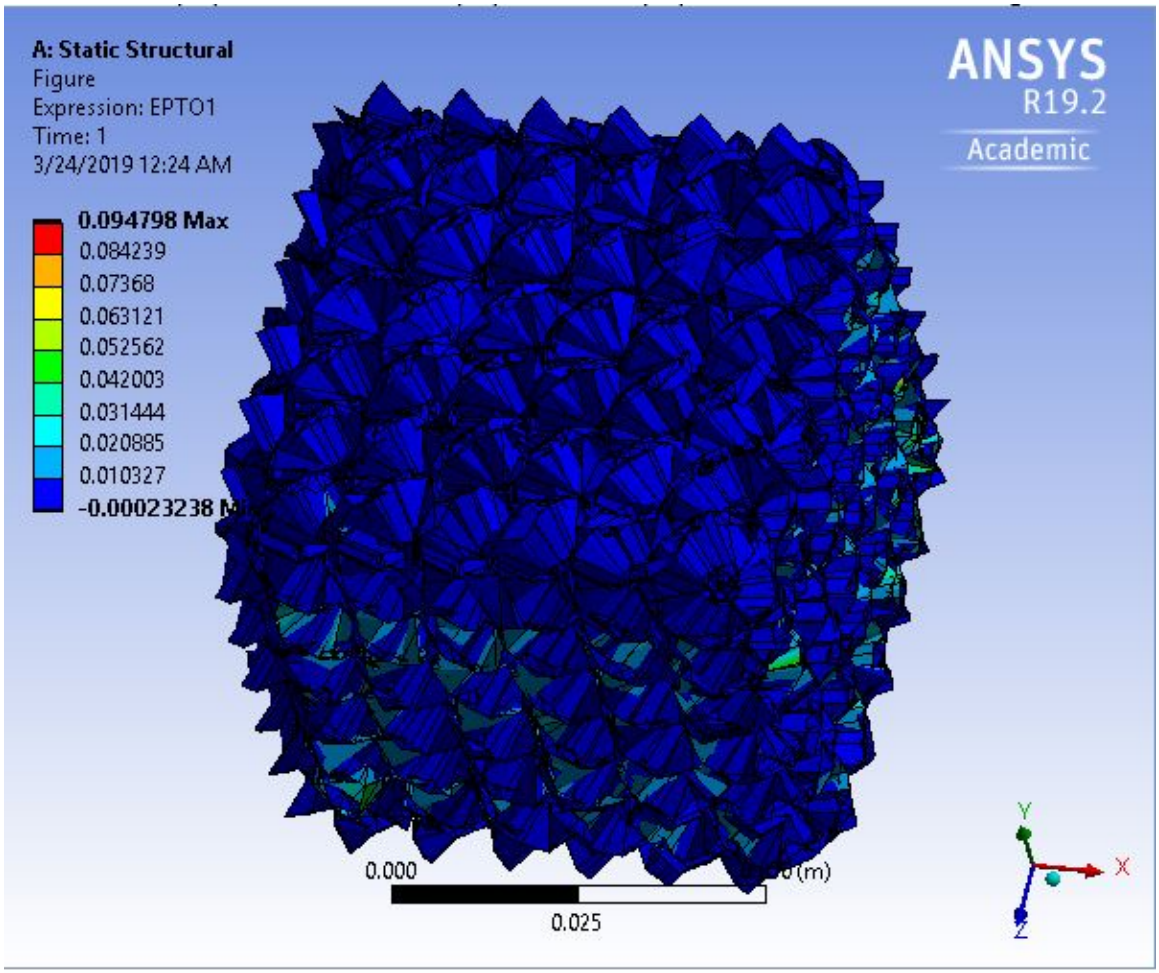

Figure B.21: The User Defined Result of EPTO as Explained in Section 3.3.1 of the Schwarz D (10 Unit Cell) of 1 cm Wall Thickness under 2 MN of Load as Obtained from ANSYS 19.2.

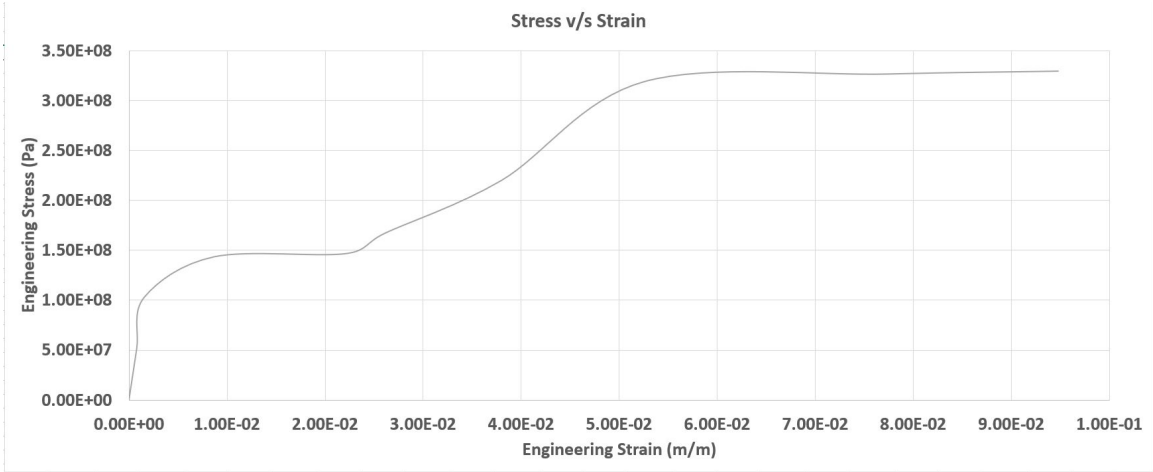

Figure B.22: The Engineering Stress v/s Engineering Strain of the Schwarz D (10 Unit Cell) of 1 cm Wall Thickness under 2 MN of Load as Obtained from ANSYS 19.2.

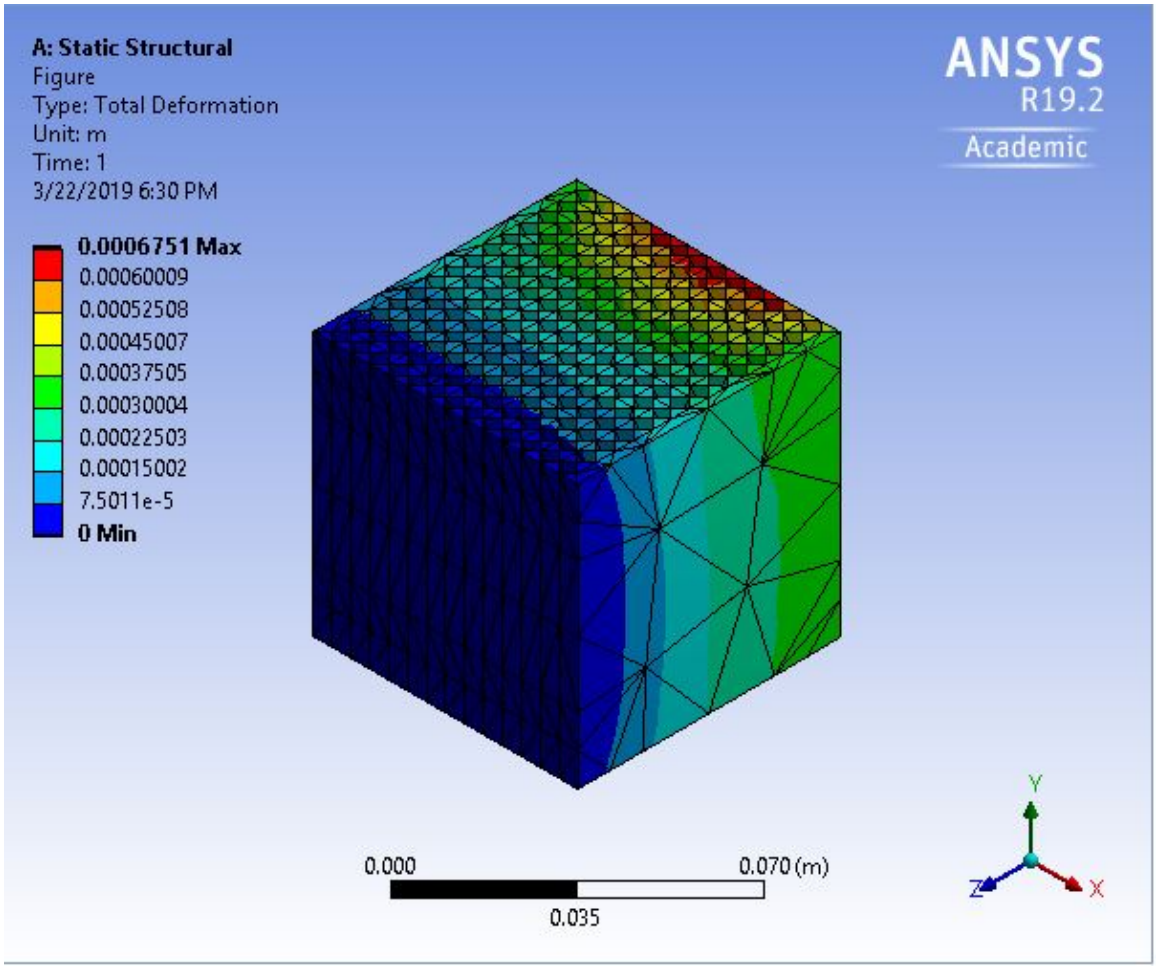

Figure B.23: Total Deformation of the Crosshatch Structure under 500 kN of Load Applied in the +Z Direction as Obtained from ANSYS 19.2.

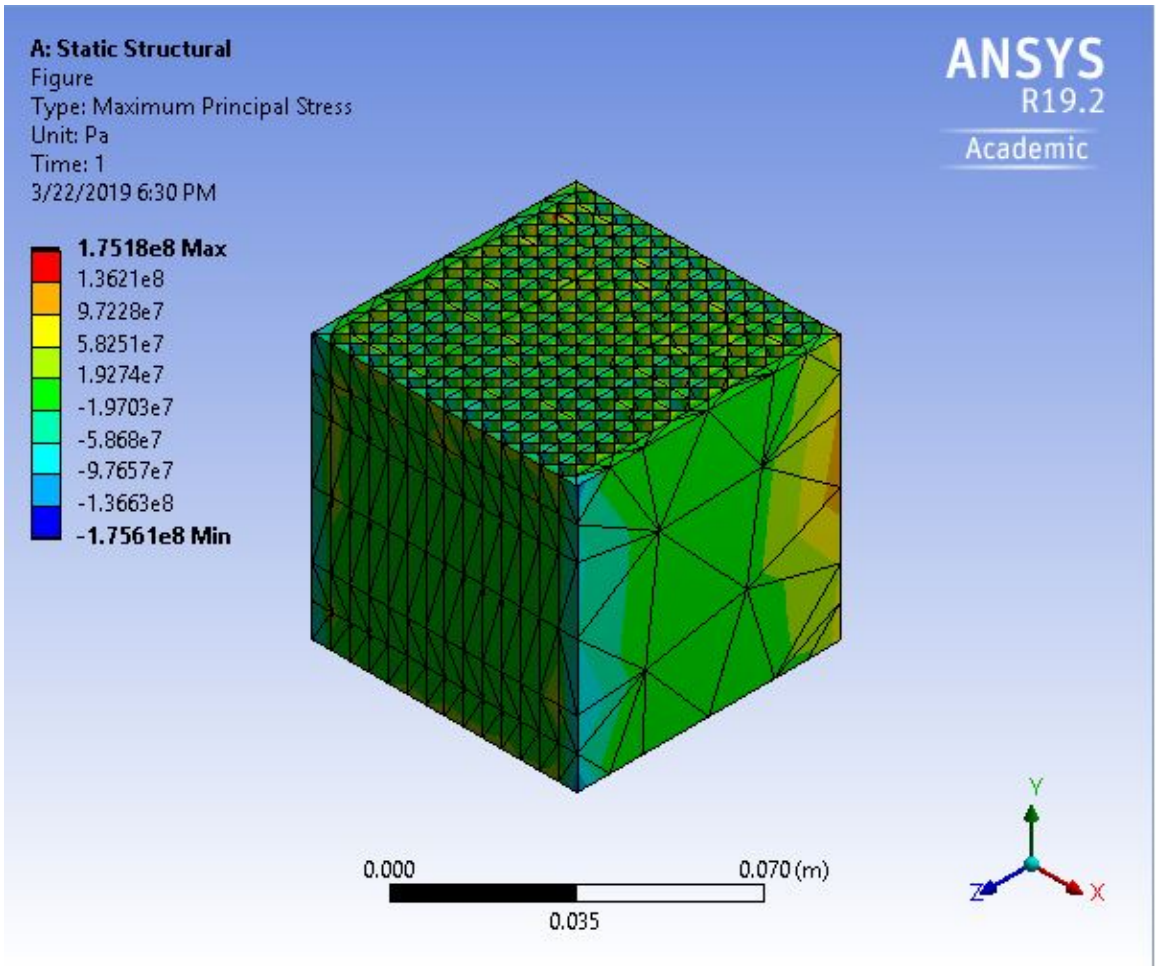

Figure B.24: Maximum Principal Stress of the Crosshatch Structure under 500 kN of Load Applied in the +Z Direction as Obtained from ANSYS 19.2.

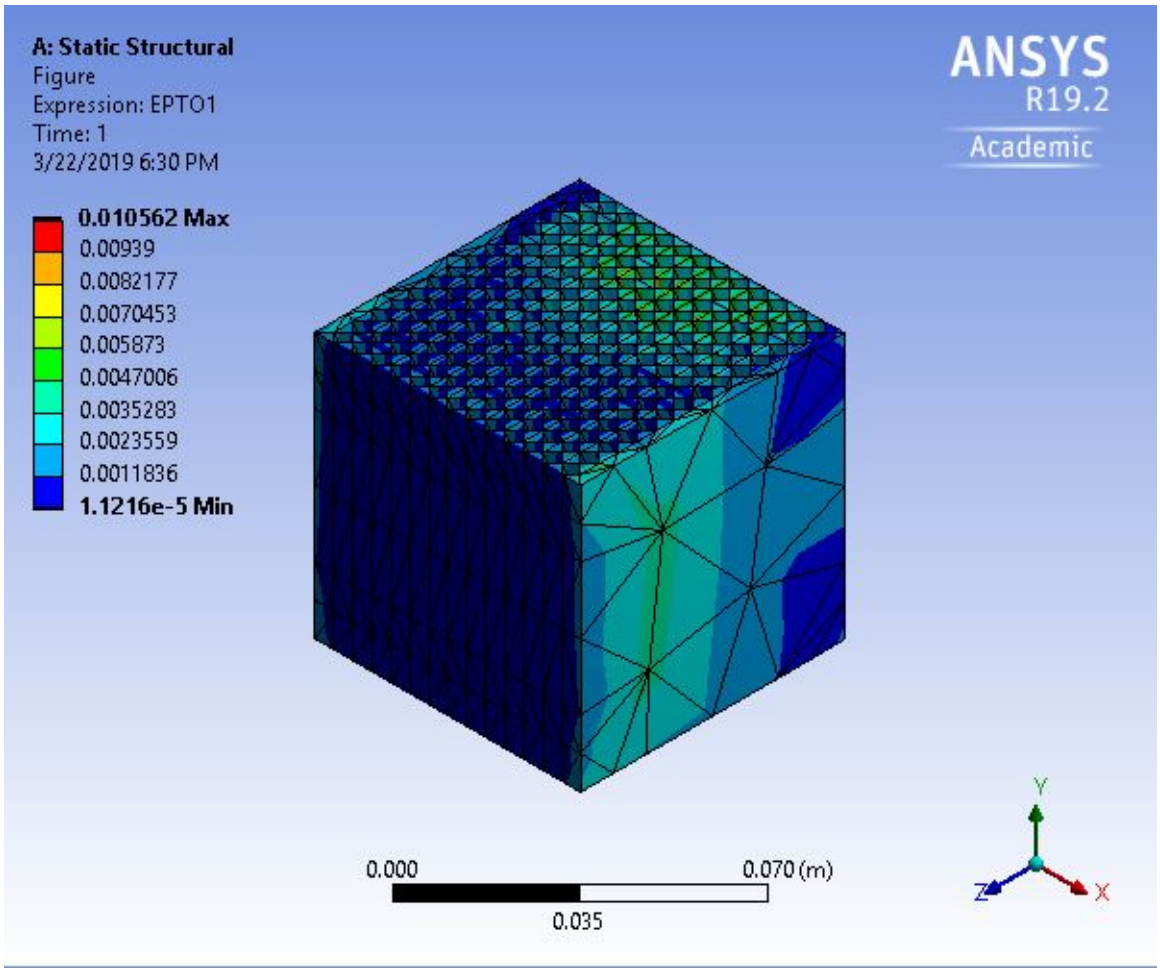

Figure B.25: The User Defined Result of EPTO as Explained in Section 3.3.1 Crosshatch Structure under 500 kN of Load Applied in the +Z Direction as Obtained from ANSYS 19.2.

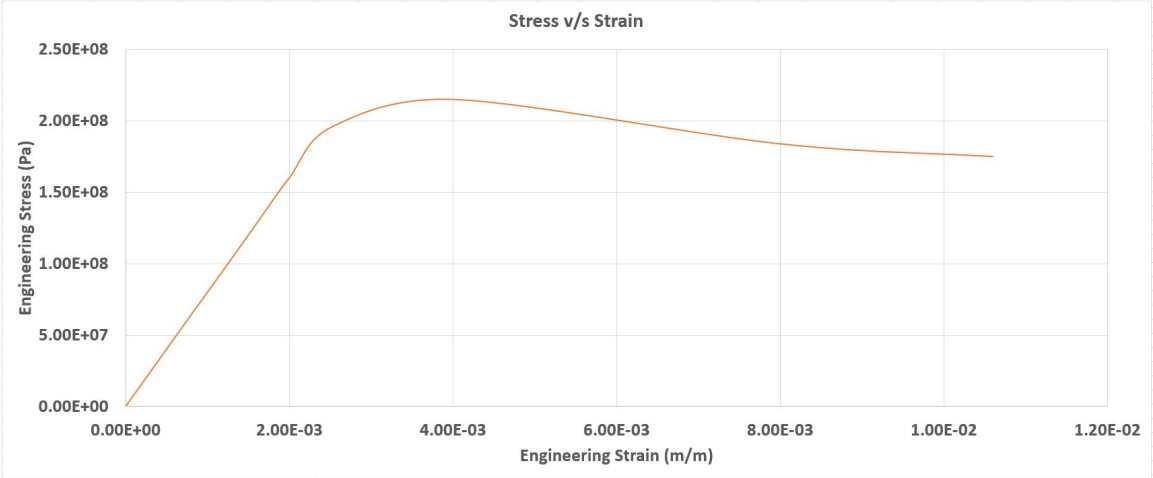

Figure B.26: The Engineering Stress v/s Engineering Strain of the Crosshatch Structure under 500 kN of Load Applied in the +Z Direction as Obtained from ANSYS 19.2.

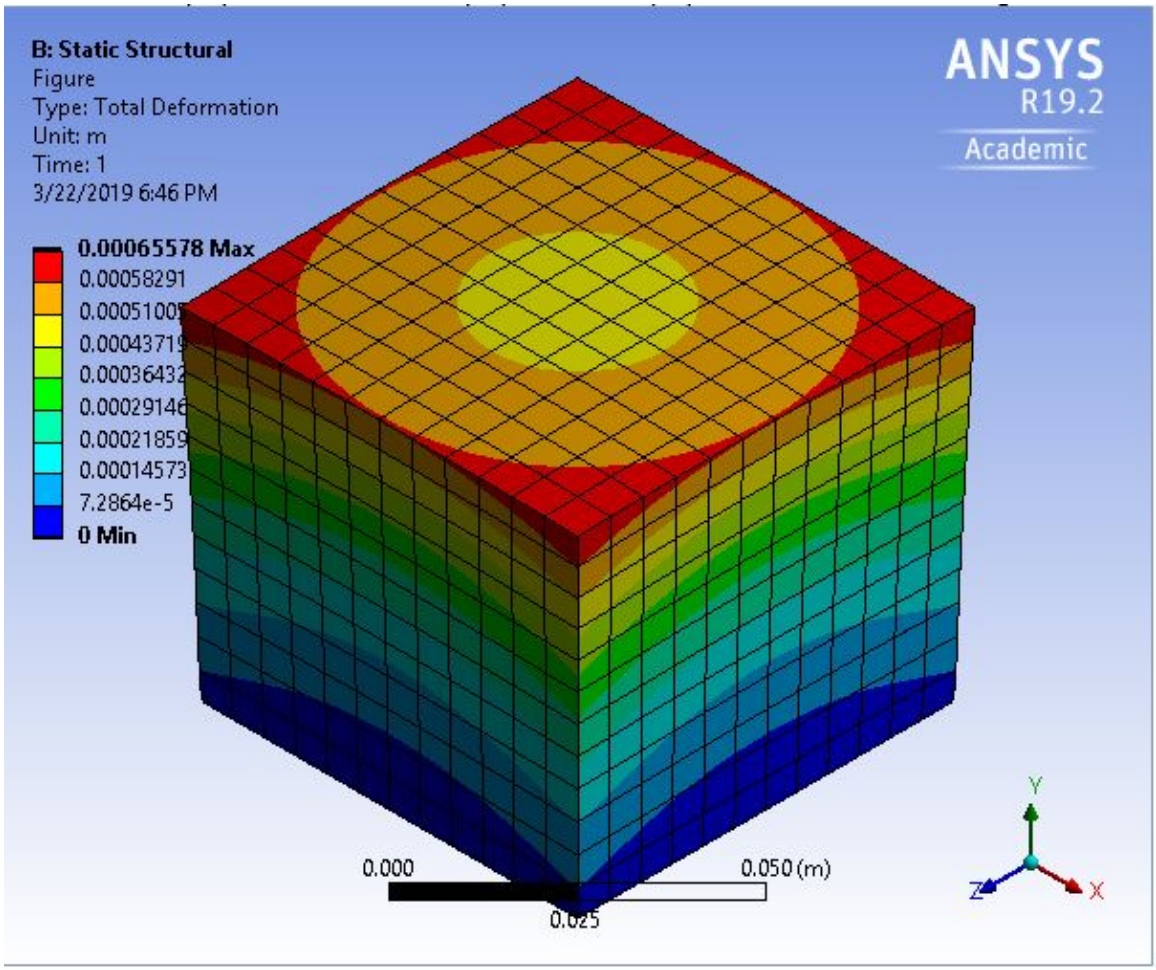

Figure B.27: Total Deformation of the Solid Cube Structure under 1.4 MN of Load as Obtained from ANSYS 19.2.

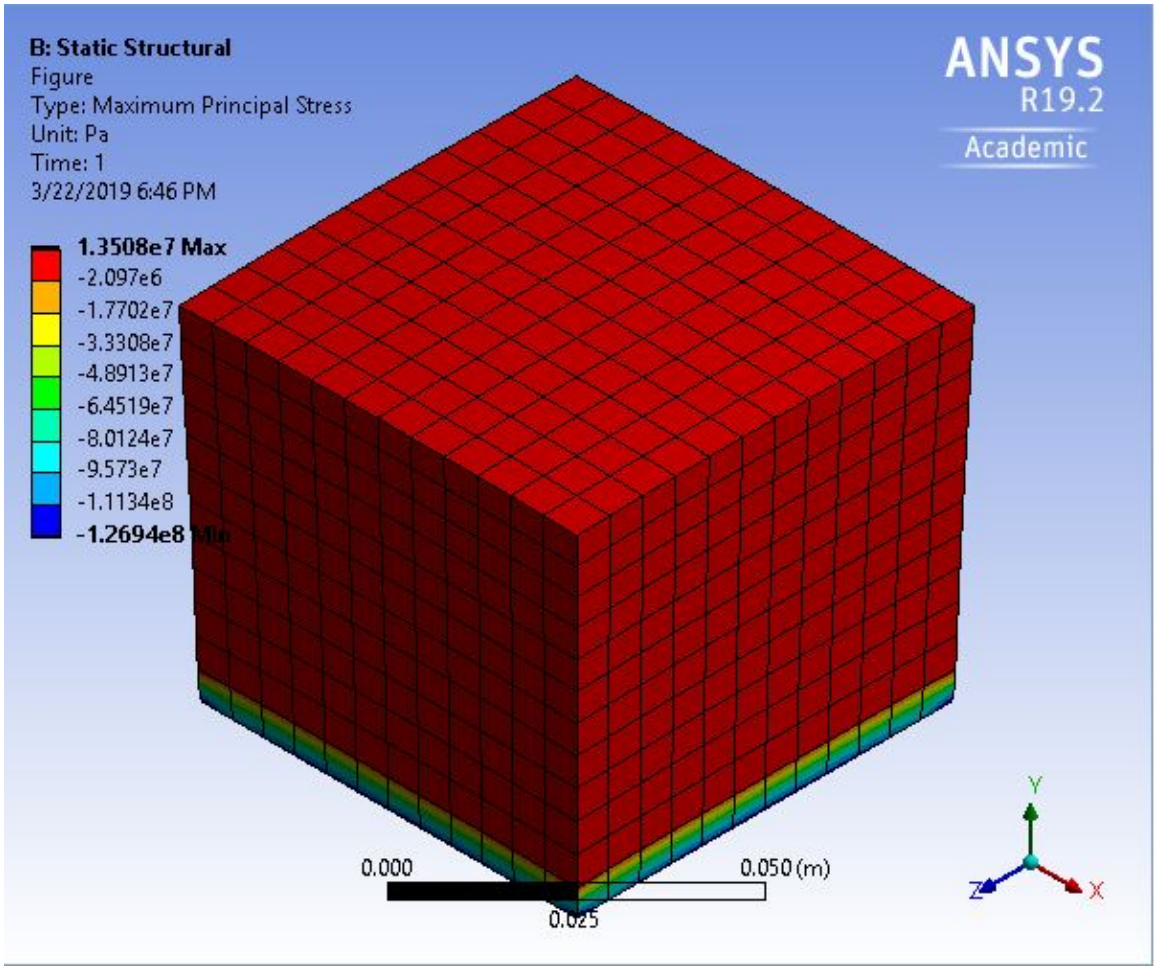

Figure B.28: Maximum Principal Stress of the Solid Cube Structure under 1.4 MN of Load as Obtained from ANSYS 19.2.

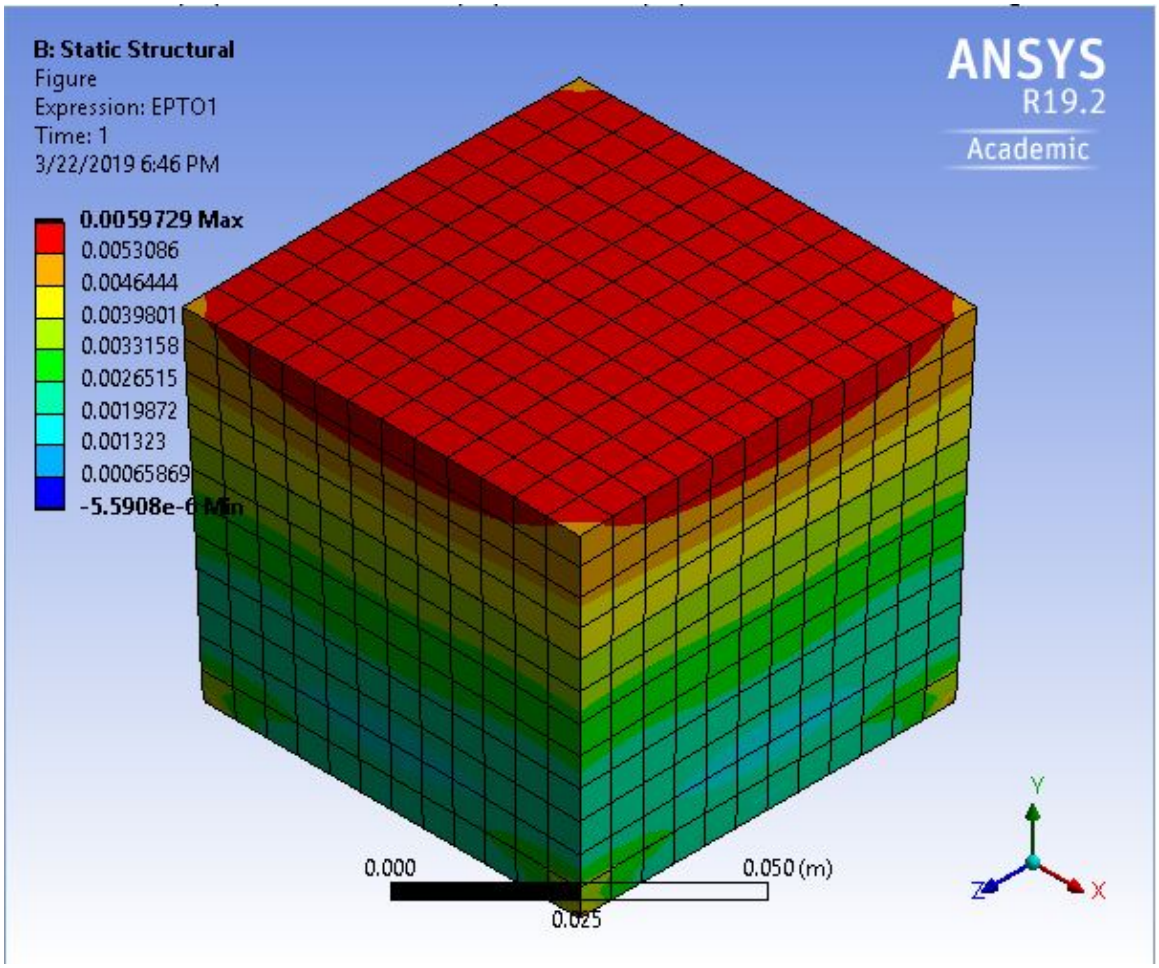

Figure B.29: The User Defined Result of EPTO as Explained in Section 3.3.1 Solid Cube Structure under 1.4 MN of Load as Obtained from ANSYS 19.2.

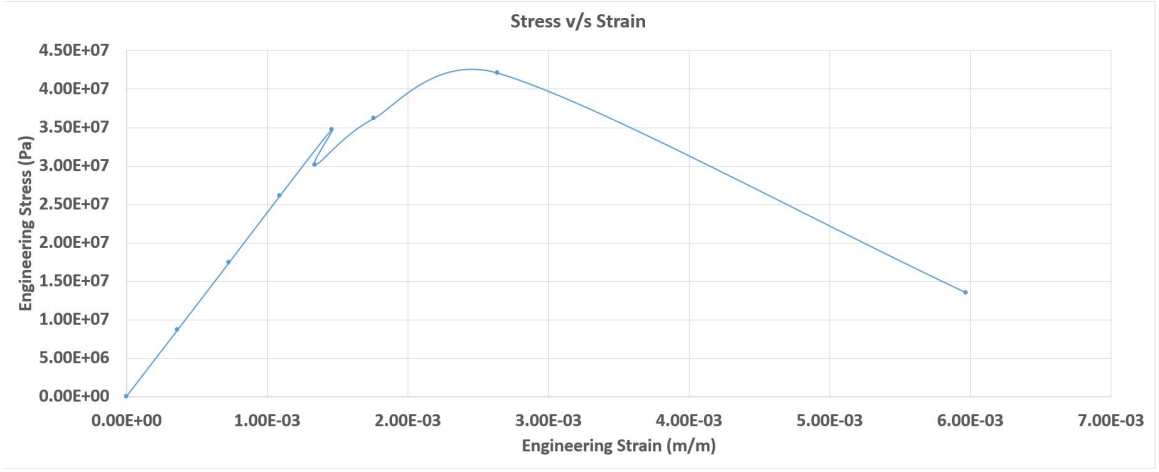

Figure B.30: The Engineering Stress v/s Engineering Strain of the Solid Cube Structure under 1.4 MN of Load as Obtained from ANSYS 19.2.

APPENDIX C

COMPLETE RESULTS OF THE THERMAL ANALYSIS ANALYSIS OF THE TPMS MODELS PERFORMED USING ANSYS 19.2.

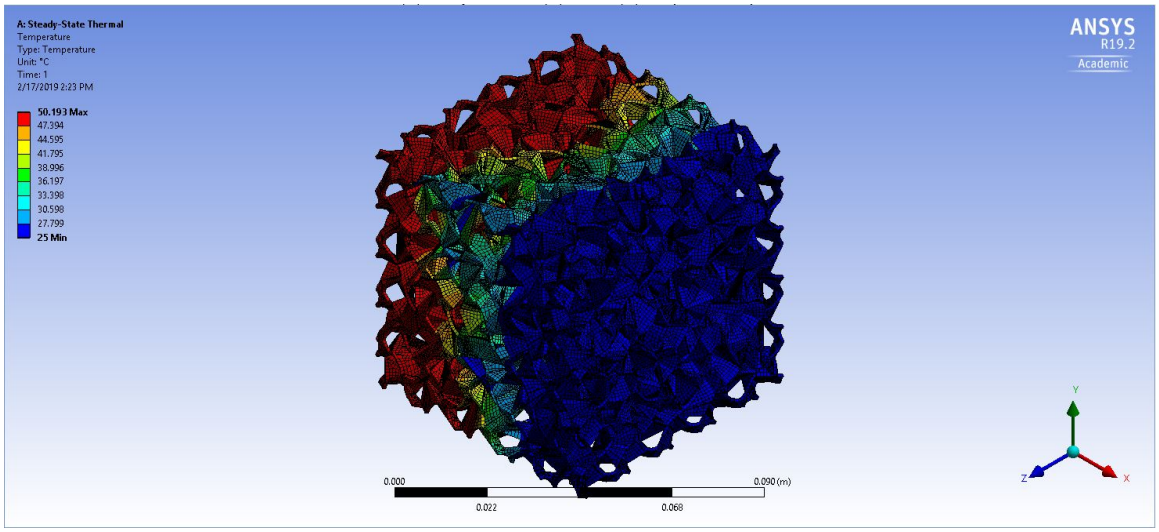

Figure C.1: Temperature Distribution in the Gyroid (10 Unit Cell) TPMS Model of 0.8 mm Wall Thickness with a ΔT of 25°C and ABS Plastic Material Properties Applied as Obtained from ANSYS 19.2.

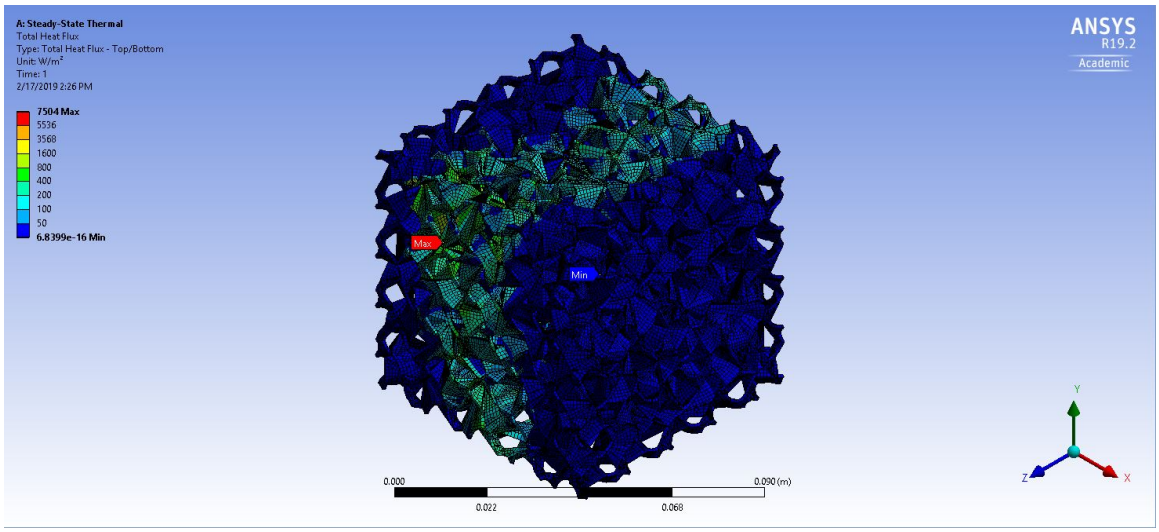

Figure C.2: Heat Flux Distribution in the Gyroid (10 Unit Cell) TPMS Model of 0.8 mm Wall Thickness with a ΔT of 25°C and ABS Plastic Material Properties Applied as Obtained from ANSYS 19.2.

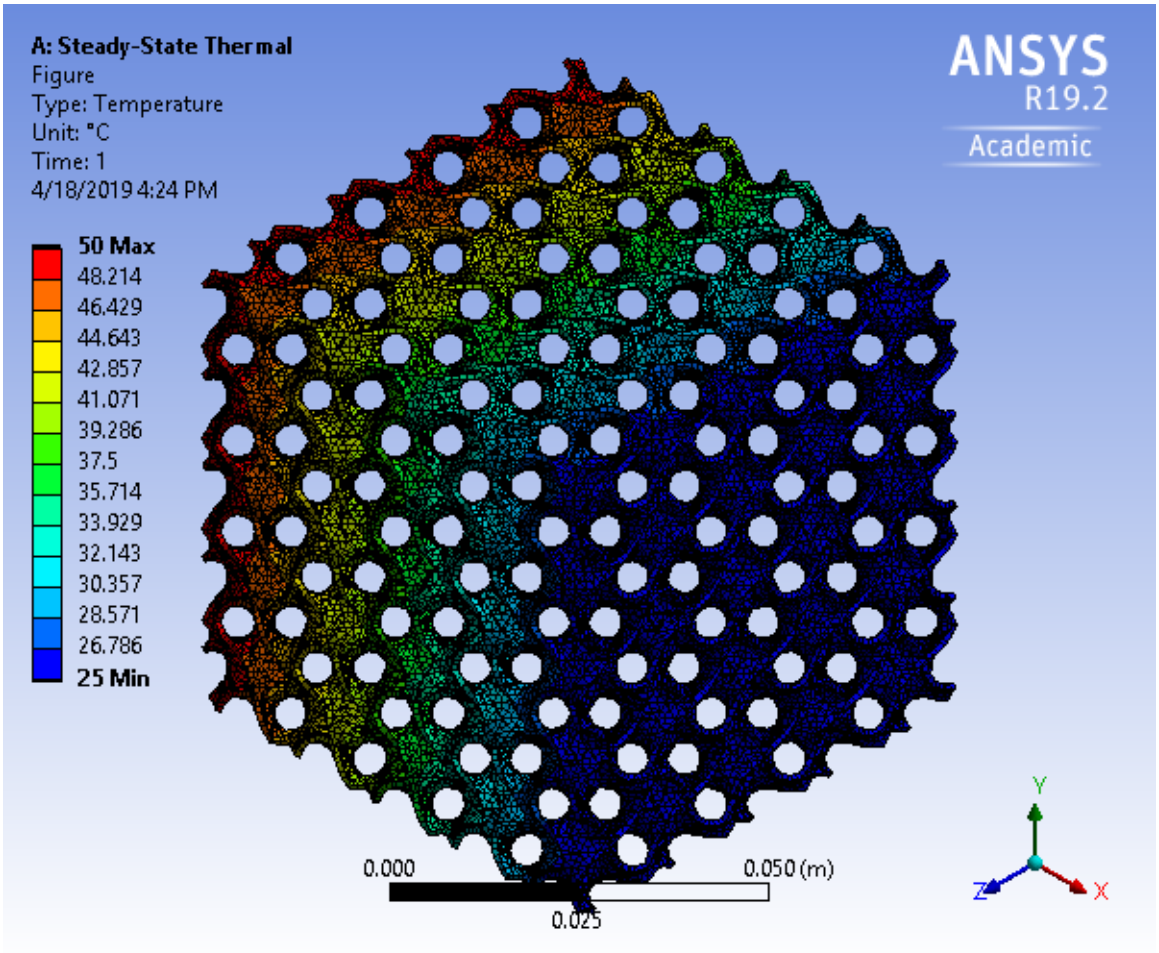

Figure C.3: Temperature Distribution in the Gyroid (15 Unit Cell) TPMS Model of 0.8 mm Wall Thickness with a ΔT of 25°C and ABS Plastic Material Properties Applied as Obtained from ANSYS 19.2.

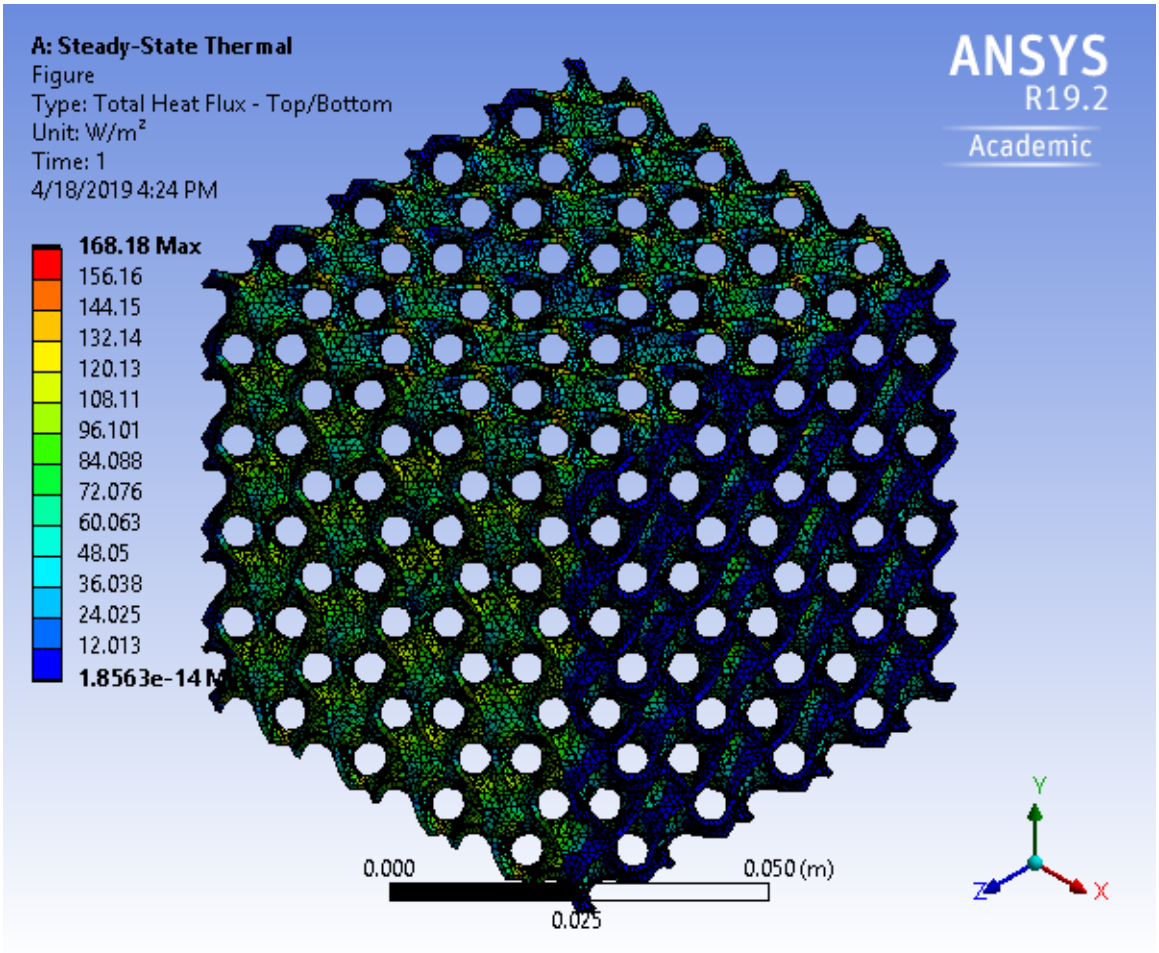

Figure C.4: Heat Flux Distribution in the Gyroid (15 Unit Cell) TPMS Model of 0.8 mm Wall Thickness with a ΔT of 25°C and ABS Plastic Material Properties Applied as Obtained from ANSYS 19.2.

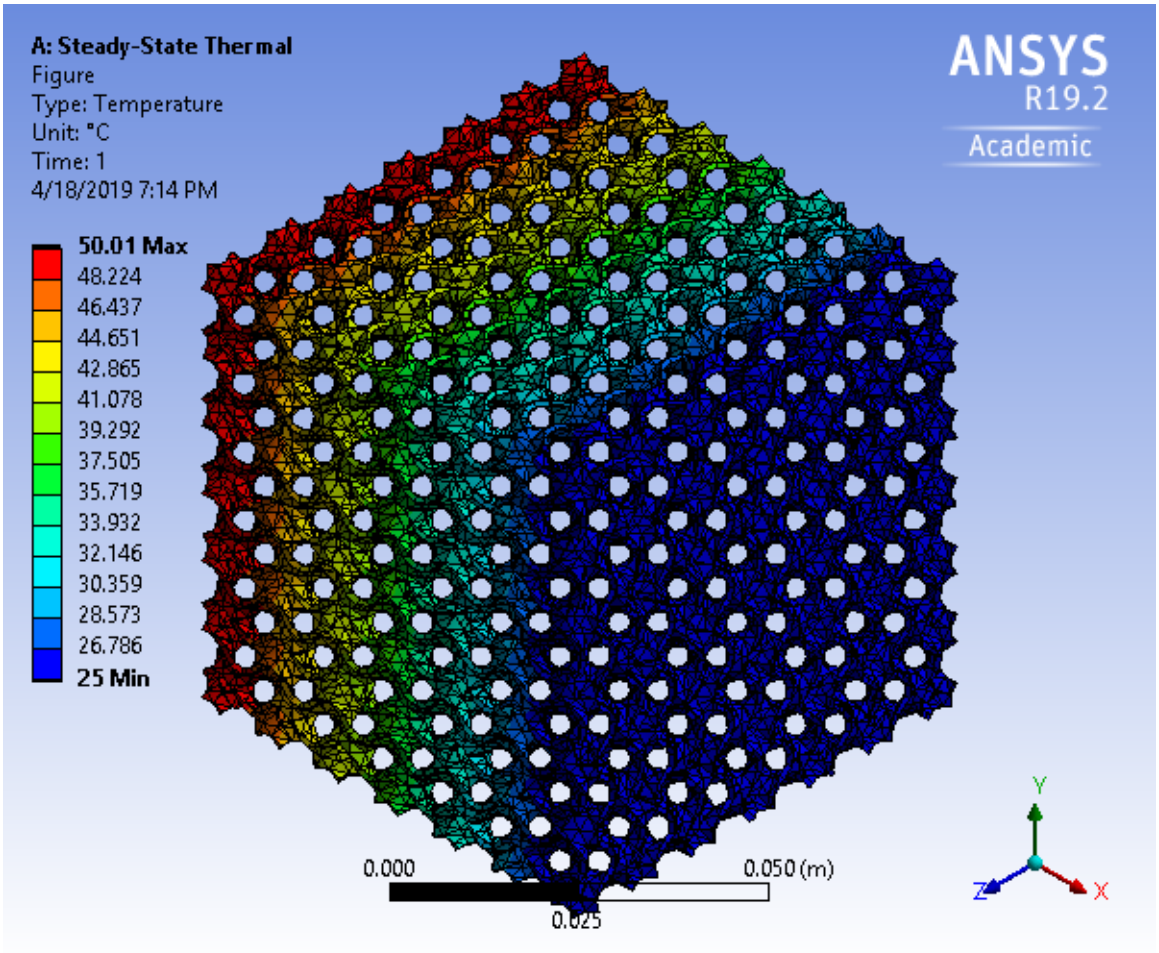

Figure C.5: Temperature Distribution in the Gyroid (20 Unit Cell) TPMS Model of 0.8 mm Wall Thickness with a ΔT of 25°C and ABS Plastic Material Properties Applied as Obtained from ANSYS 19.2.

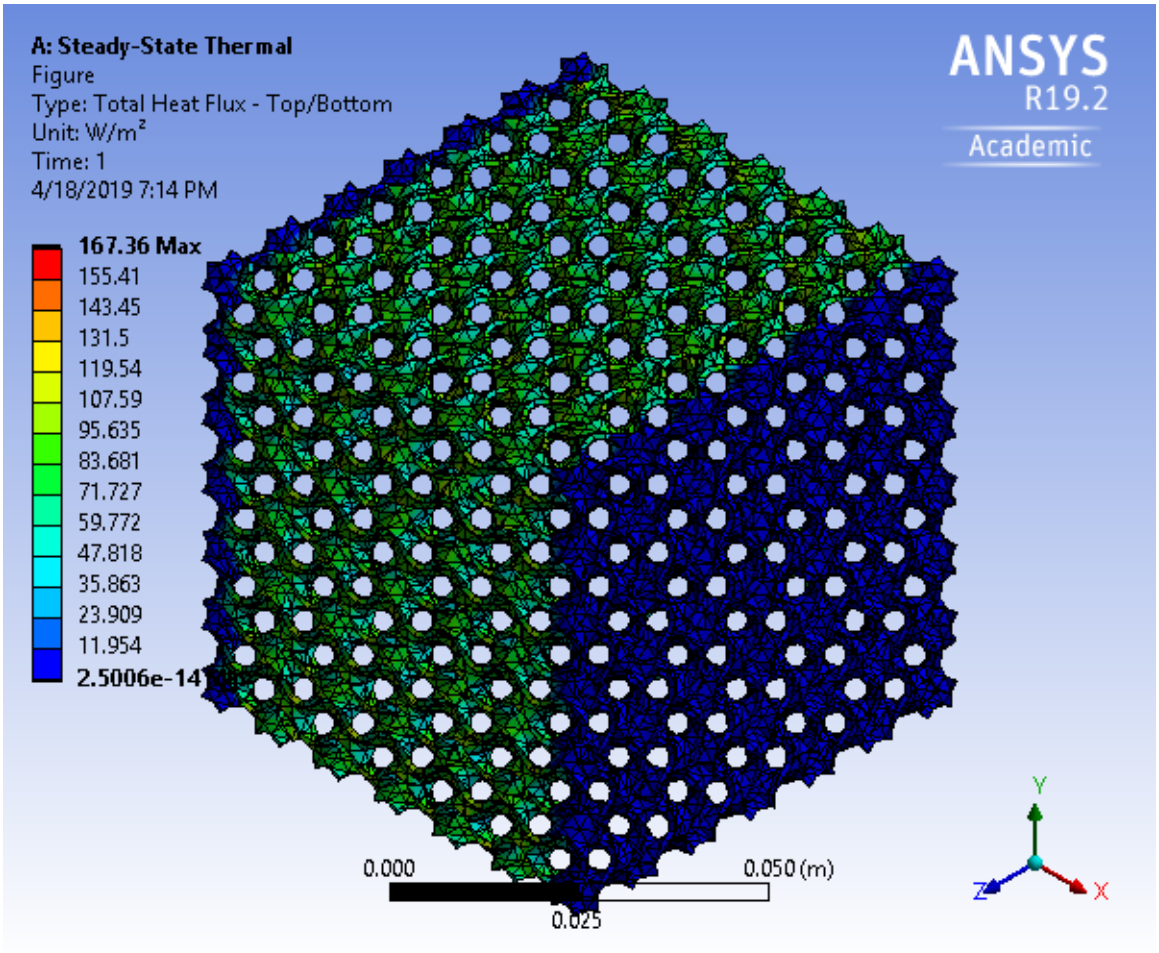

Figure C.6: Heat Flux Distribution in the Gyroid (20 Unit Cell) TPMS Model of 0.8 mm Wall Thickness with a ΔT of 25°C and ABS Plastic Material Properties Applied as Obtained from ANSYS 19.2.

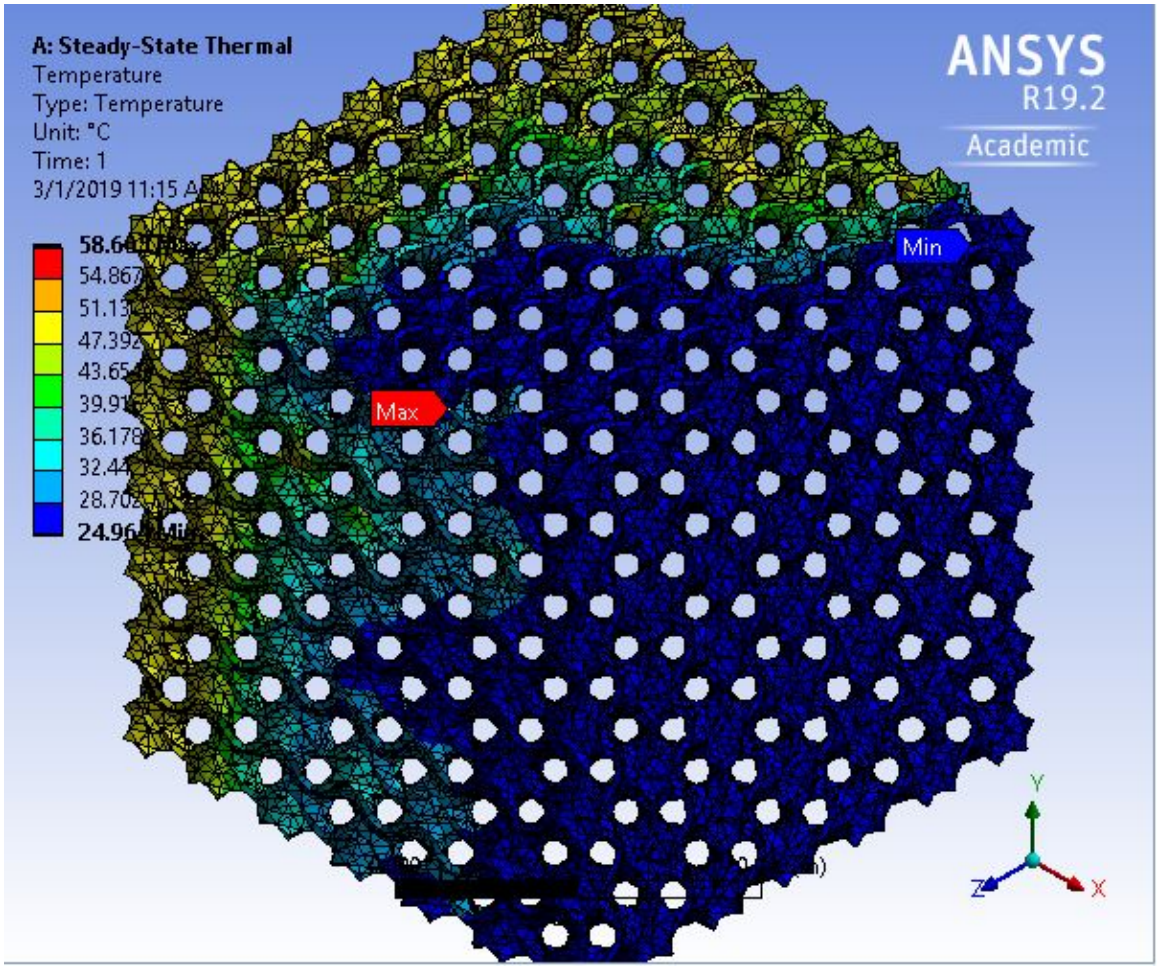

Figure C.7: Temperature Distribution in the Gyroid (25 unit cell) TPMS Model of 0.8 mm Wall Thickness with a ΔT of 25°C and ABS Plastic Material Properties Applied as Obtained from ANSYS 19.2.

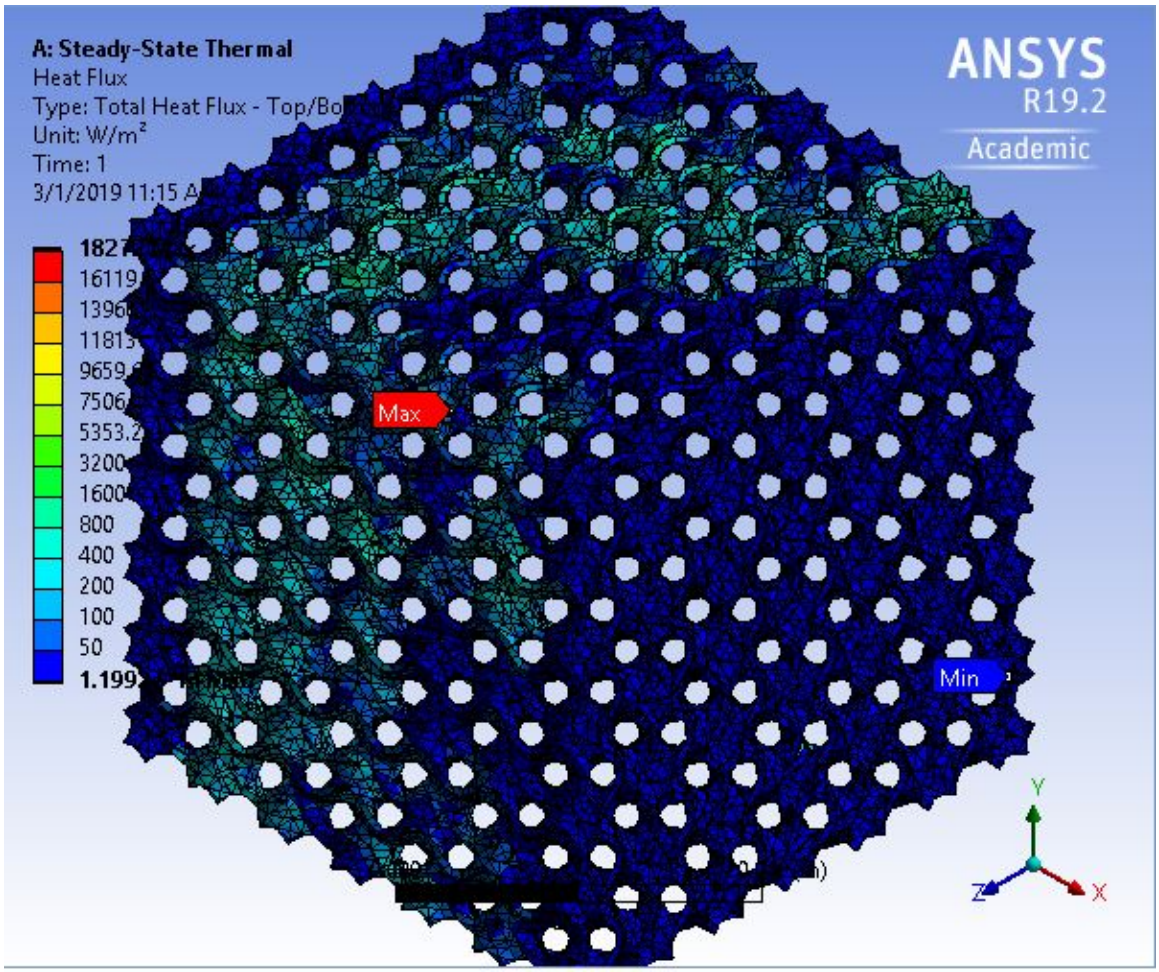

Figure C.8: Heat Flux Distribution in the Gyroid (25 unit cell) TPMS Model of 0.8 mm Wall Thickness with a ΔT of 25°C and ABS Plastic Material Properties Applied as Obtained from ANSYS 19.2.

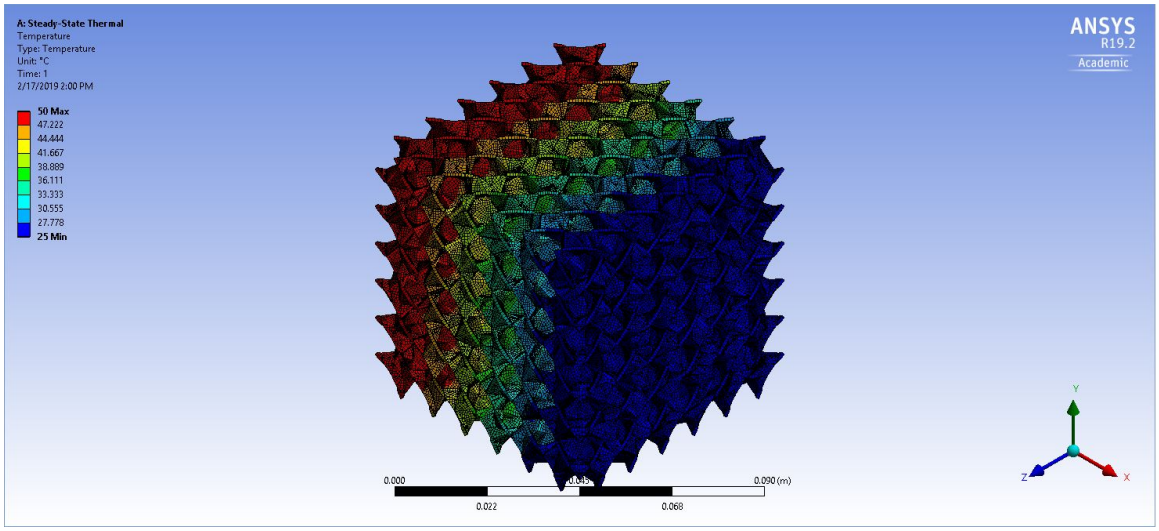

Figure C.9: Temperature Distribution in the Schwarz D (10 Unit Cell) TPMS Model of 0.8 mm Wall Thickness with a ΔT of 25°C and ABS Plastic Material Properties Applied as Obtained from ANSYS 19.2.

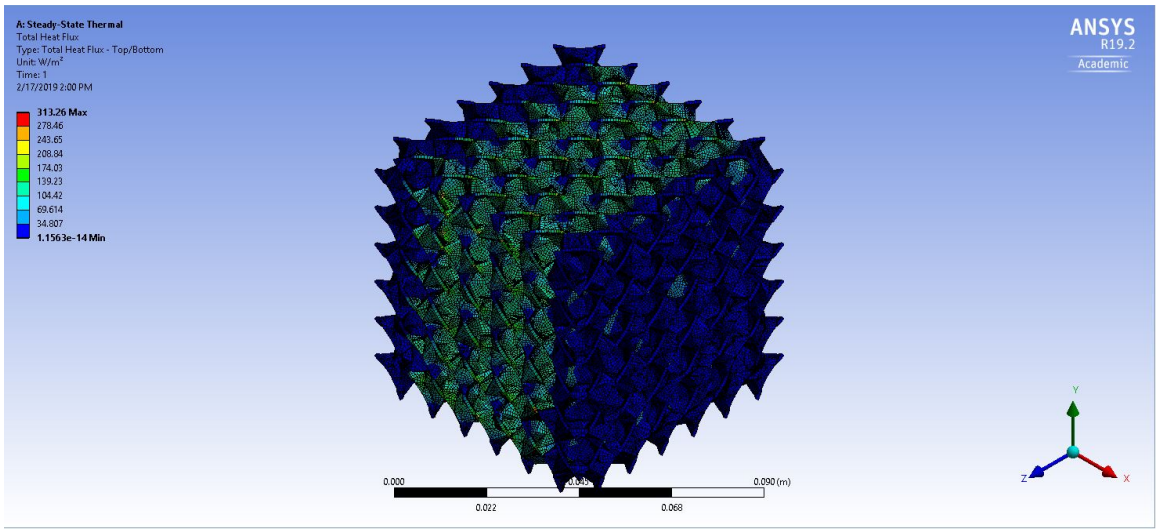

Figure C.10: Heat Flux Distribution in the Schwarz D (10 Unit Cell) TPMS Model of 0.8 mm Wall Thickness with a ΔT of 25°C and ABS Plastic Material Properties Applied as Obtained from ANSYS 19.2.

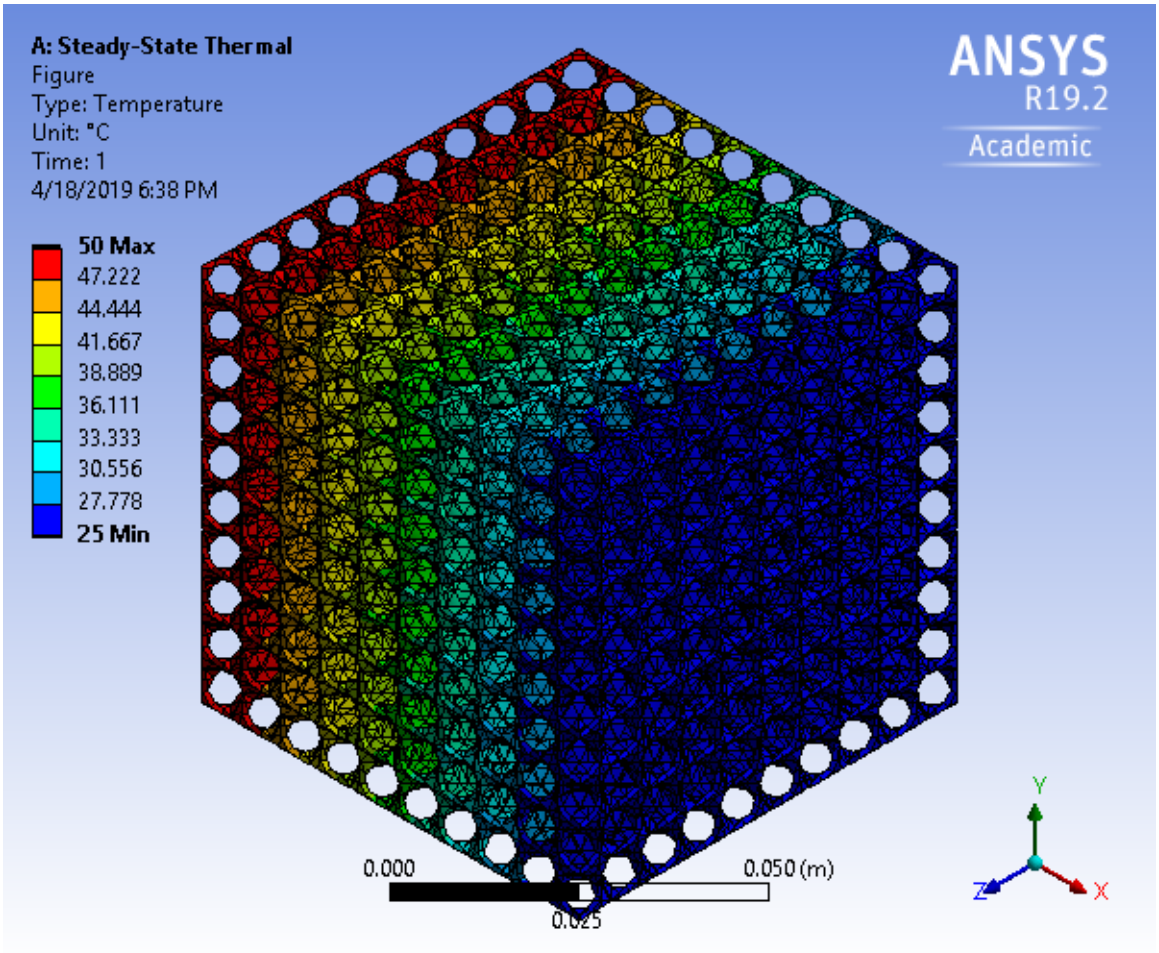

Figure C.11: Temperature Distribution in the Schwarz D (15 Unit Cell) TPMS Model of 0.8 mm Wall Thickness with a ΔT of 25°C and ABS Plastic Material Properties Applied as Obtained from ANSYS 19.2.

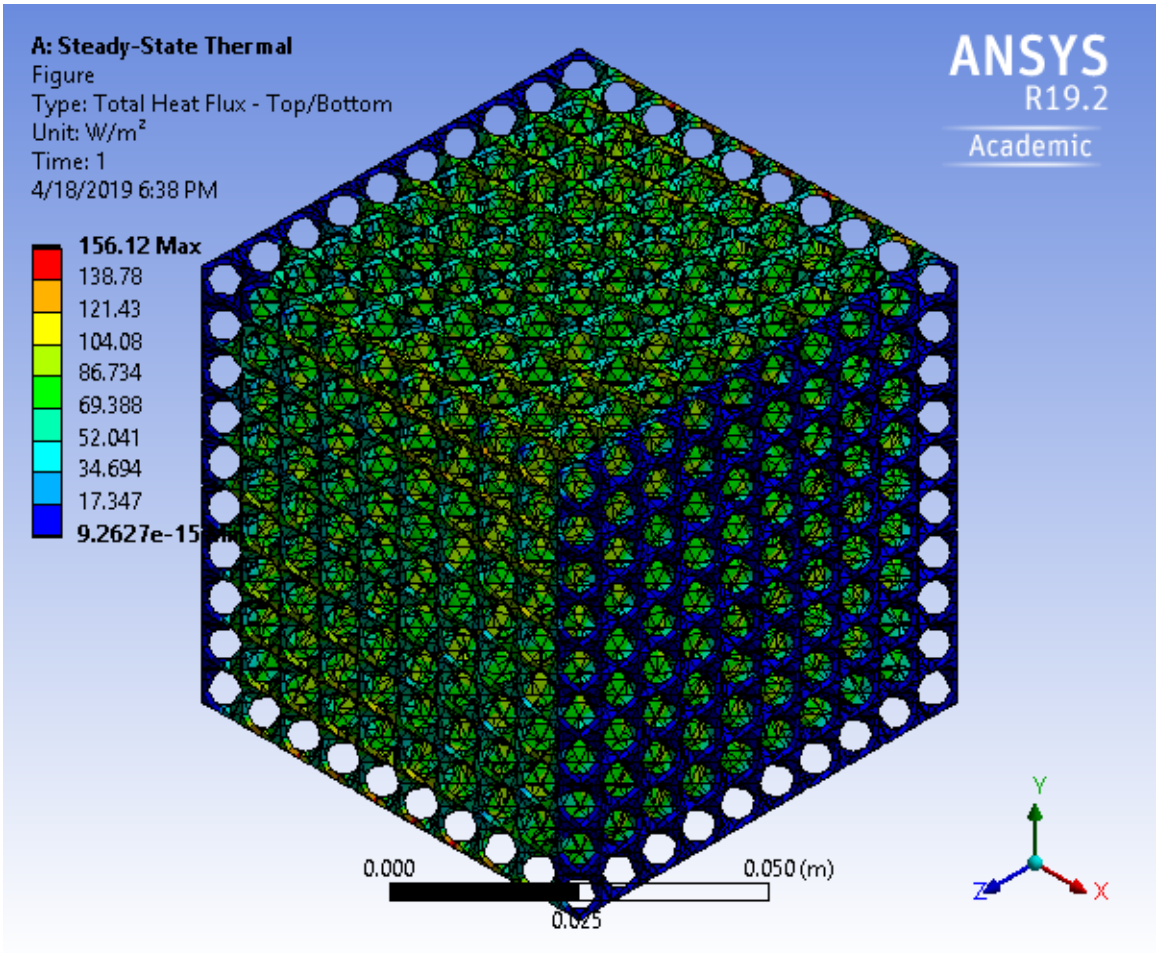

Figure C.12: Heat Flux Distribution in the Schwarz D (15 Unit Cell) TPMS Model of 0.8 mm Wall Thickness with a ΔT of 25°C and ABS Plastic Material Properties Applied as Obtained from ANSYS 19.2.

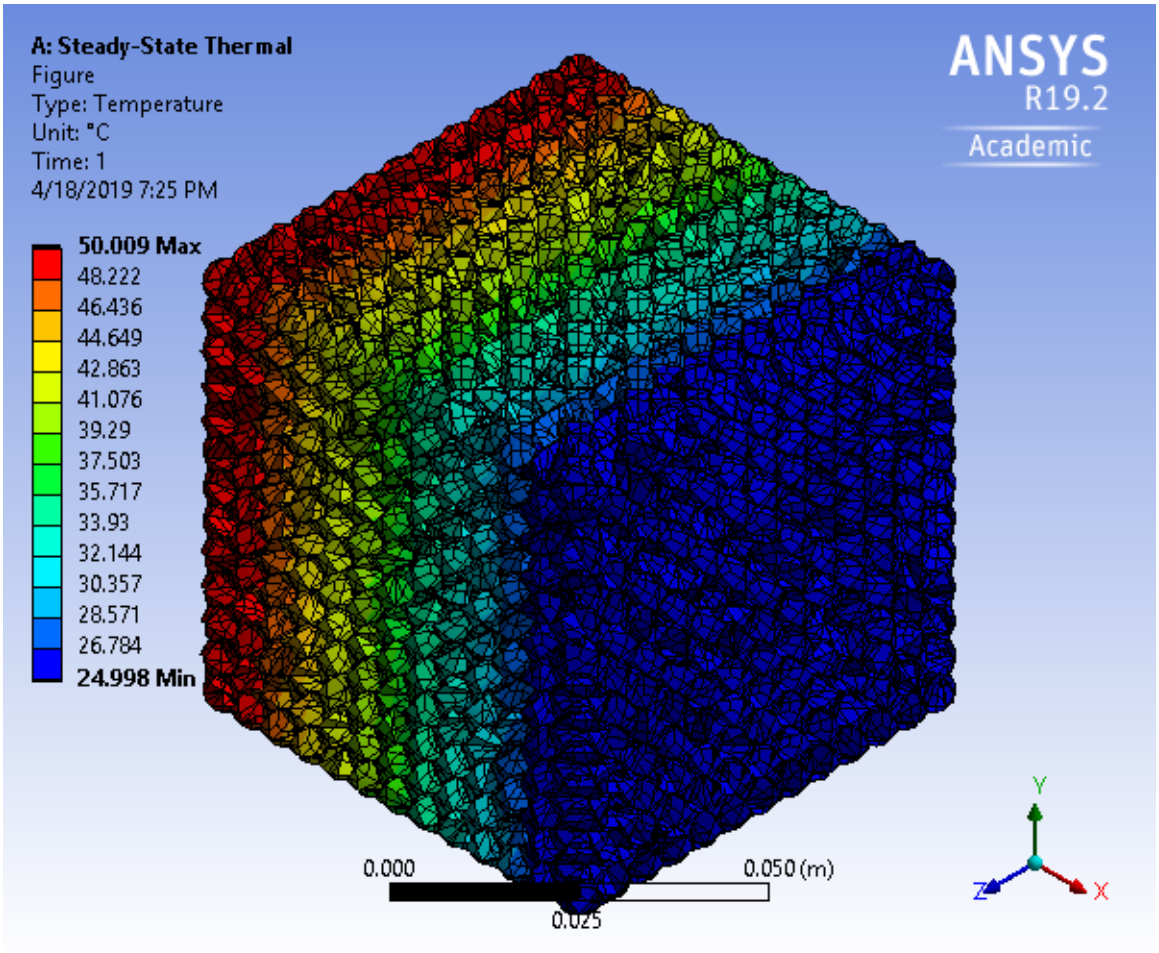

Figure C.13: Temperature Distribution in the Schwarz D (20 Unit Cell) TPMS Model of 0.8 mm Wall Thickness with a ΔT of 25°C and ABS Plastic Material Properties Applied as Obtained from ANSYS 19.2.

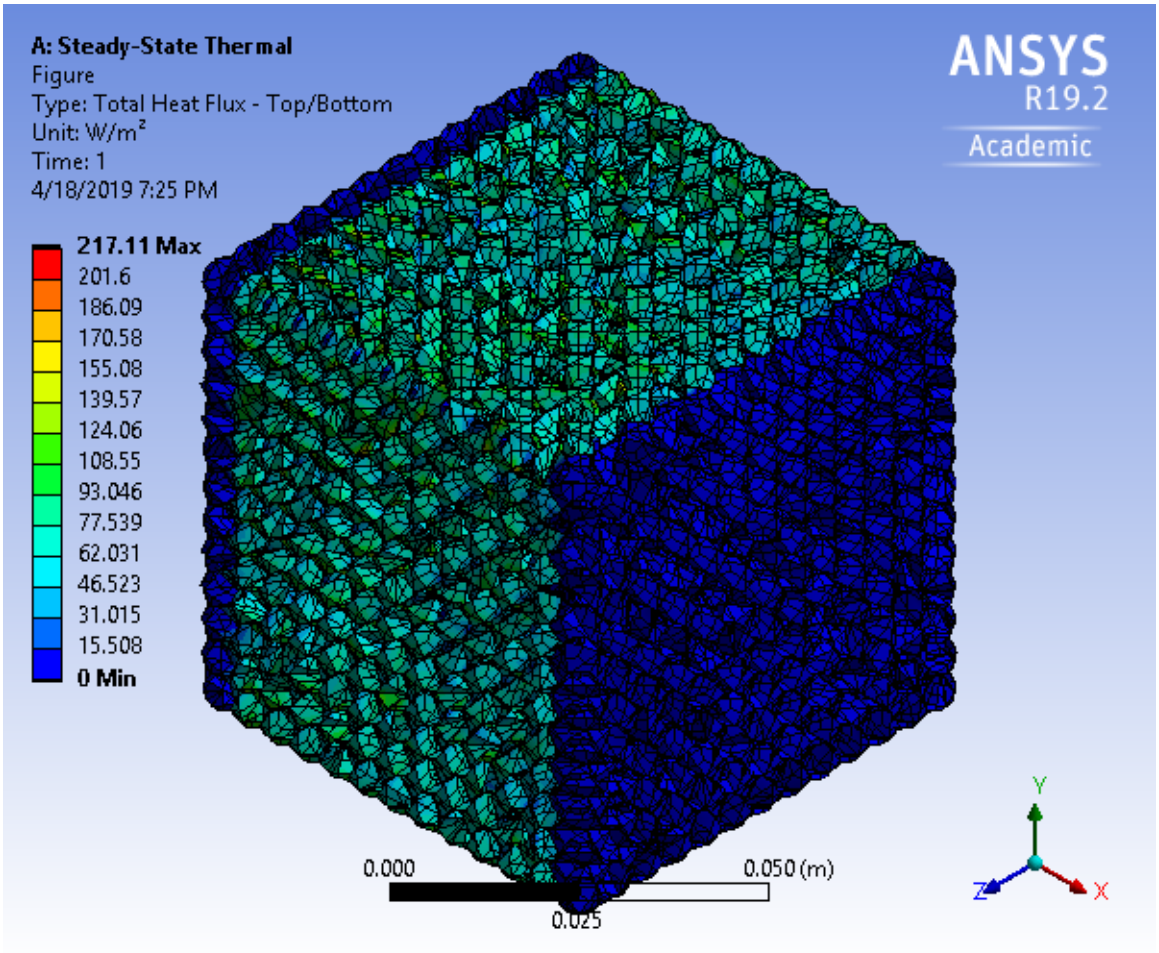

Figure C.14: Heat Flux Distribution in the Schwarz D (20 Unit Cell) TPMS Model of 0.8 mm Wall Thickness with a ΔT of 25°C and ABS Plastic Material Properties Applied as Obtained from ANSYS 19.2.

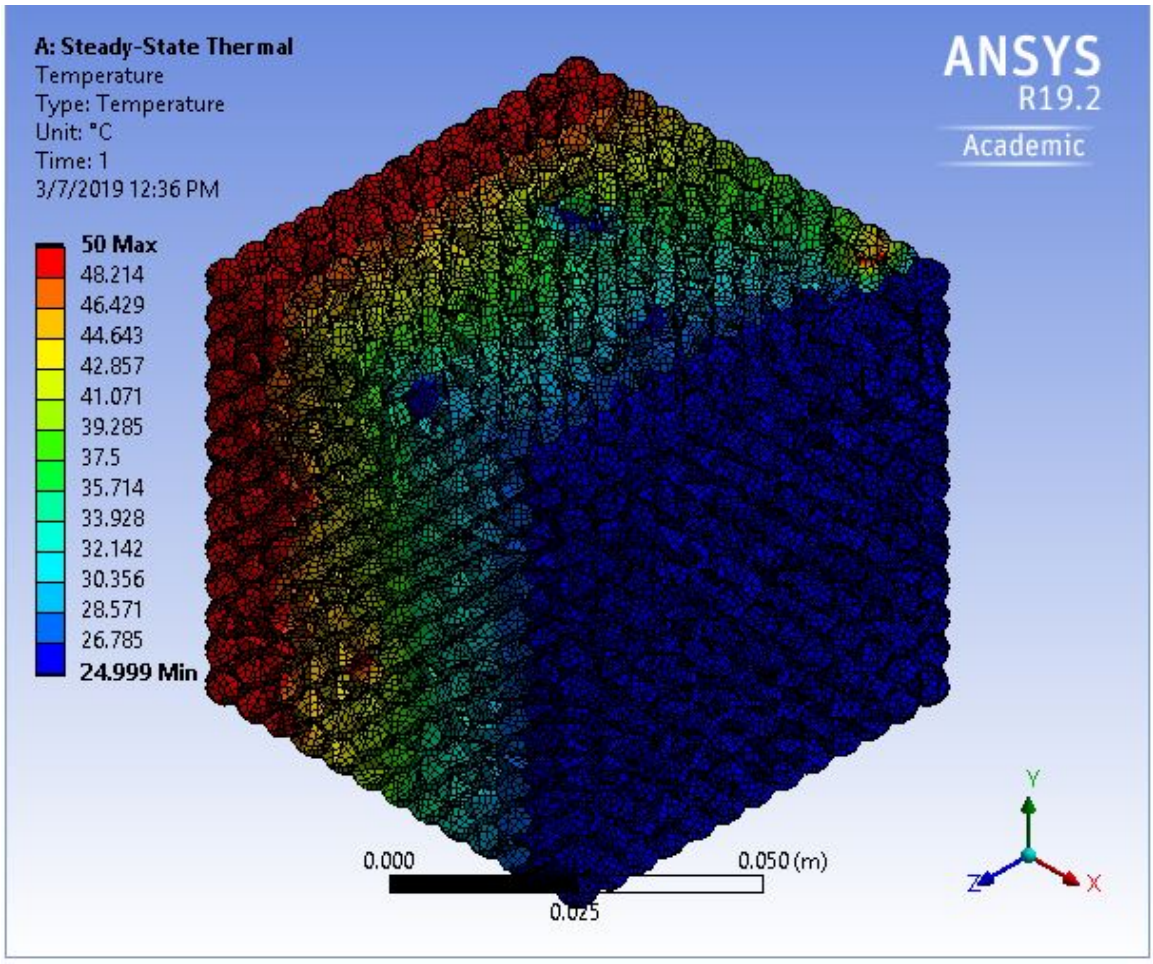

Figure C.15: Temperature Distribution in the Schwarz D (25 Unit Cell) TPMS Model of 0.8 mm Wall Thickness with a ΔT of 25°C and ABS Plastic Material Properties Applied as Obtained from ANSYS 19.2.

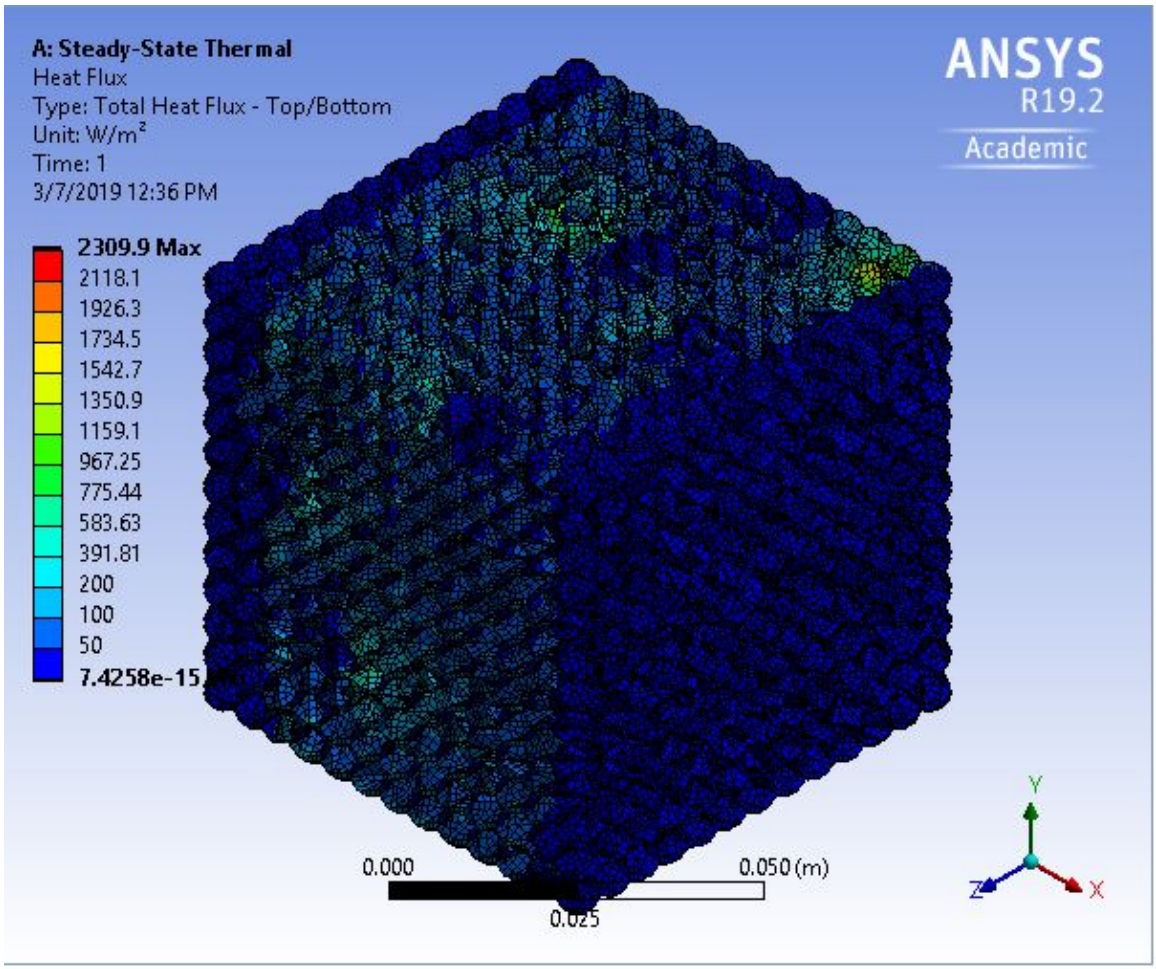

Figure C.16: Heat Flux Distribution in the Schwarz D (25 Unit Cell) TPMS Model of 0.8 mm Wall Thickness with a ΔT of 25°C and ABS Plastic Material Properties Applied as Obtained from ANSYS 19.2.

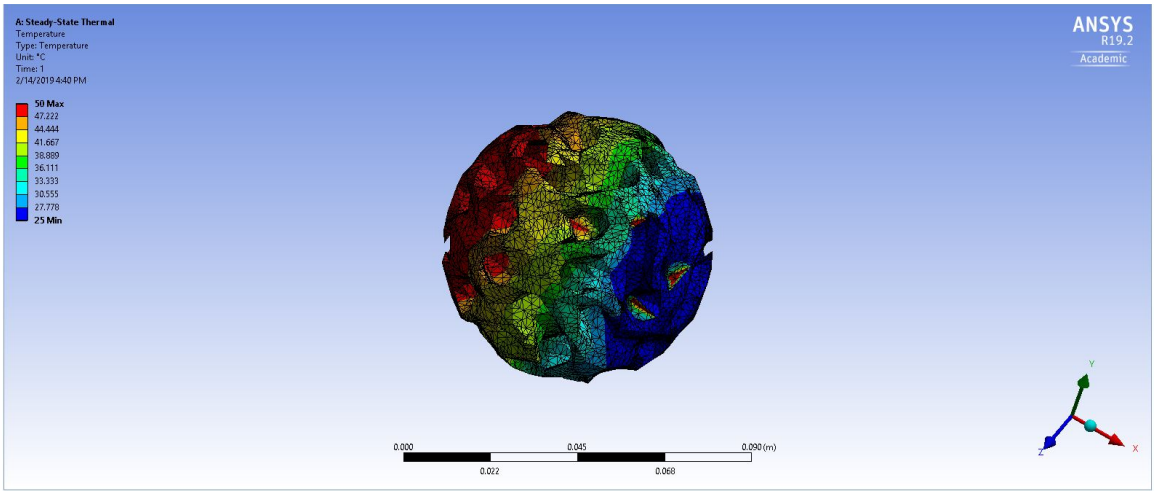

Figure C.17: Temperature Distribution in the Spherical Gyroid TPMS Model of 0.8 mm Wall Thickness with a ΔT of 25°C and ABS Plastic Material Properties Applied as Obtained from ANSYS 19.2.

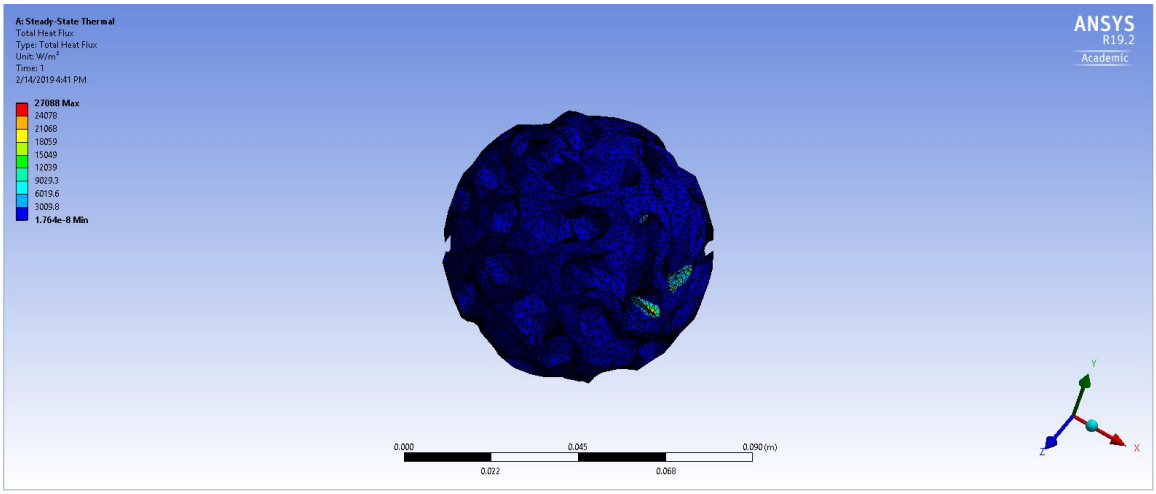

Figure C.18: Heat Flux Distribution in the Spherical Gyroid TPMS Model of 0.8 mm Wall Thickness with a ΔT of 25°C and ABS Plastic Material Properties Applied as Obtained from ANSYS 19.2.

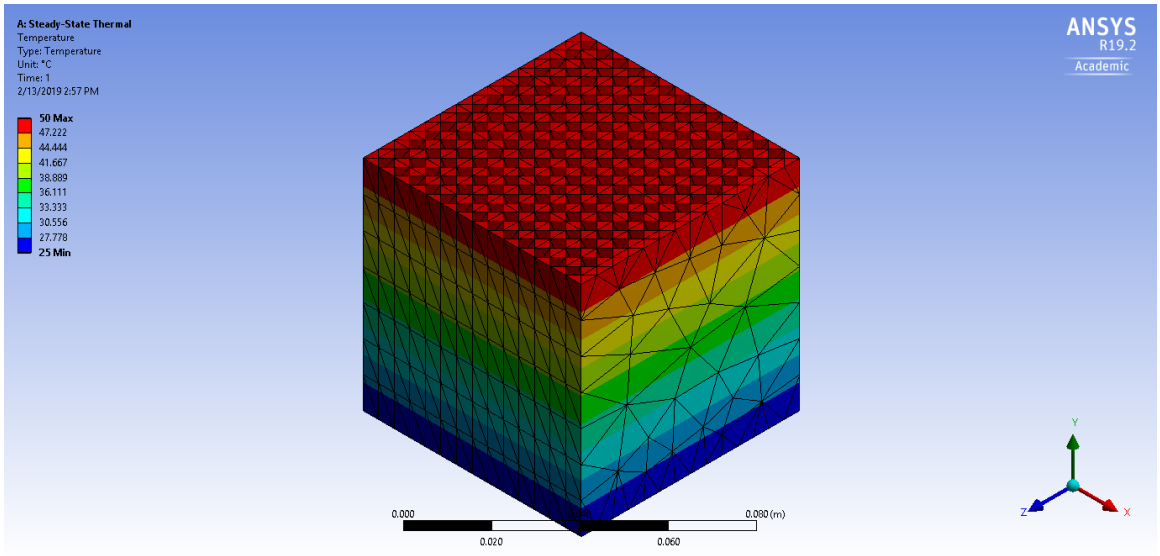

Figure C.19: Temperature Distribution in Crosshatch Model with a ΔT of 25°C and ABS Plastic Material Properties Applied as Obtained from ANSYS 19.2.

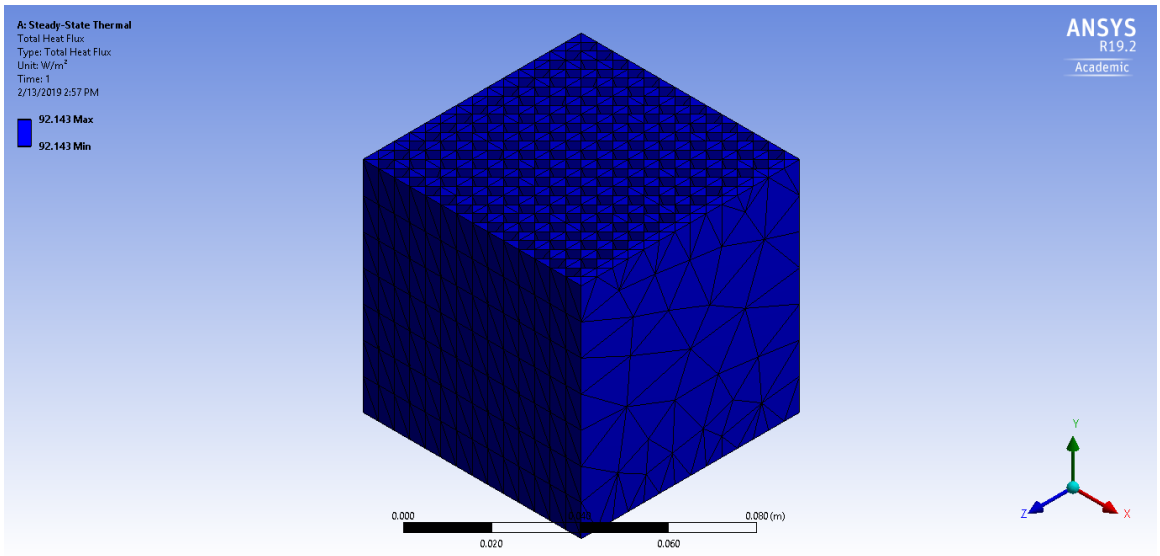

Figure C.20: Heat Flux Distribution in the Crosshatch Model with a ΔT of 25°C and ABS Plastic Material Properties Applied as Obtained from ANSYS 19.2.

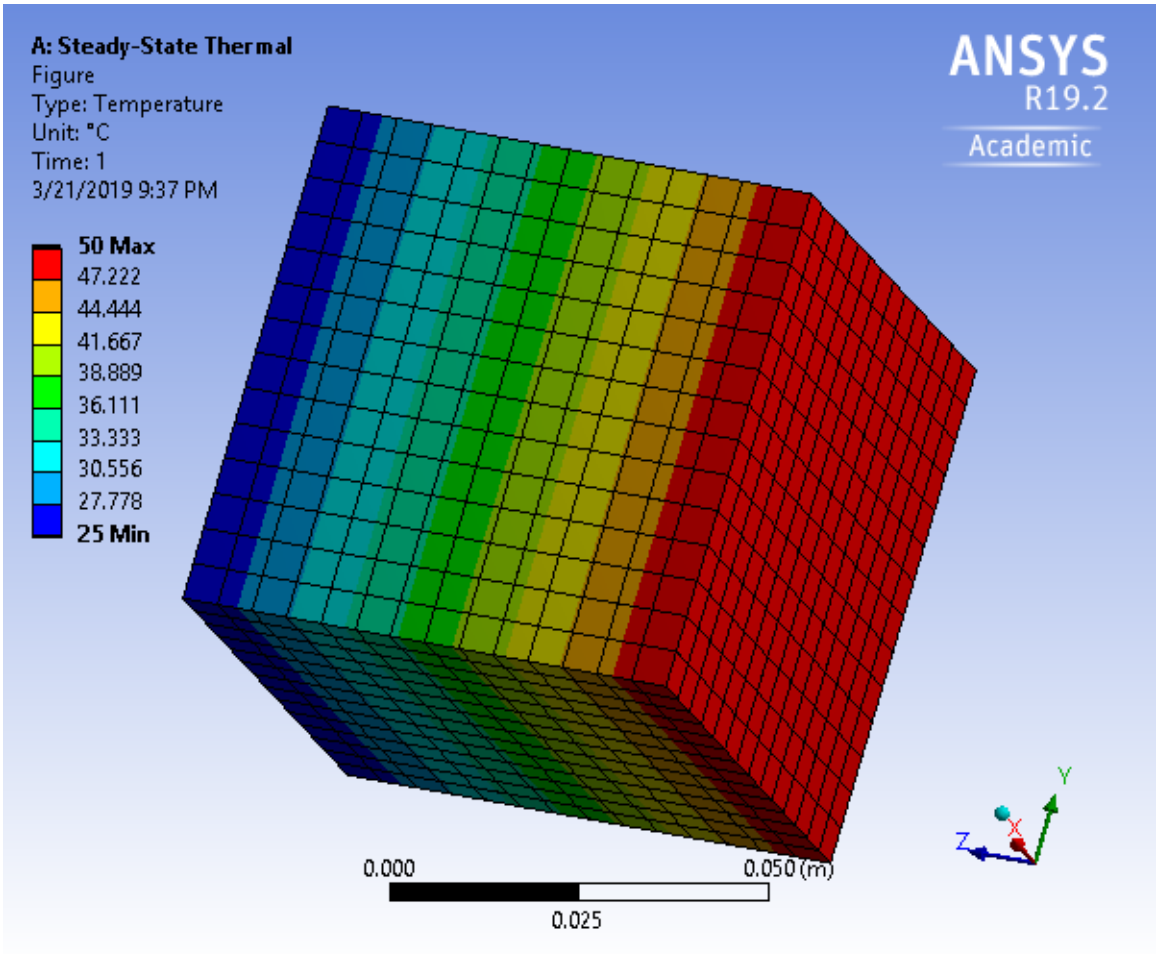

Figure C.21: Temperature Distribution in the Solid Cube Model with a ΔT of 25°C and ABS Plastic Material Properties Applied as Obtained from ANSYS 19.2.

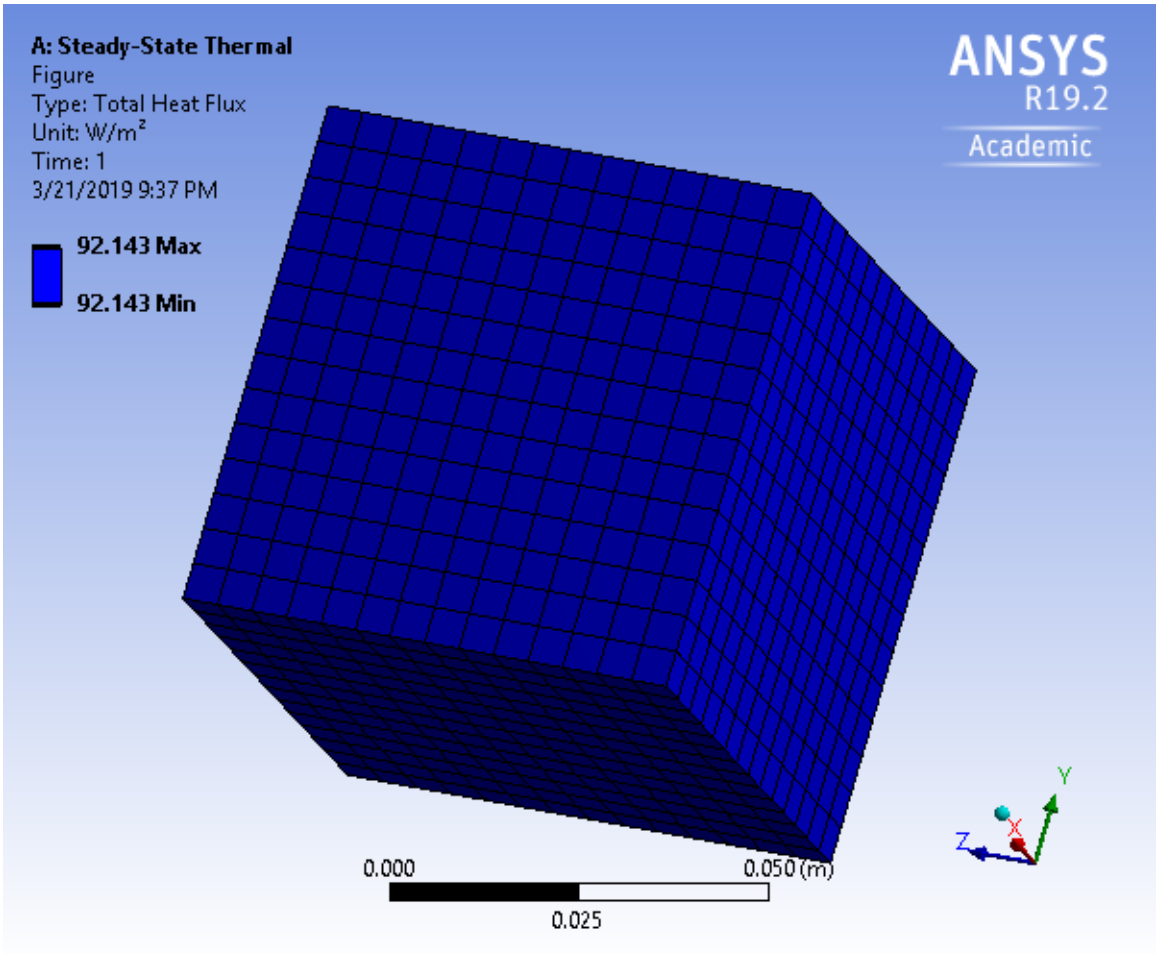

Figure C.22: Heat Flux Distribution in the Solid Cube Model with a ΔT of 25°C and ABS Plastic Material Properties Applied as Obtained from ANSYS 19.2.

APPENDIX D

COMPLETE RESULTS OF THE COMPUTATIONAL FLUID DYNAMIC ANALYSIS OF THE TPMS MODELS PERFORMED USING ANSYS FLUENT.

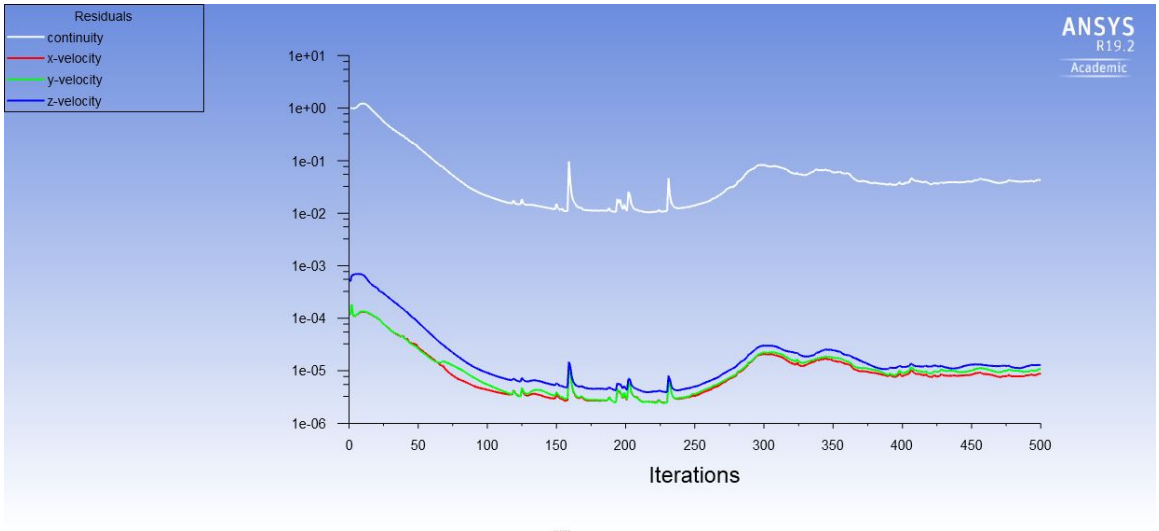

Figure D.1: Continuity and Velocity Convergence Curves for Cube with Pipes Model for a Velocity of 0.1 m/s and Air as Fluid, as Obtained from ANSYS Fluent.

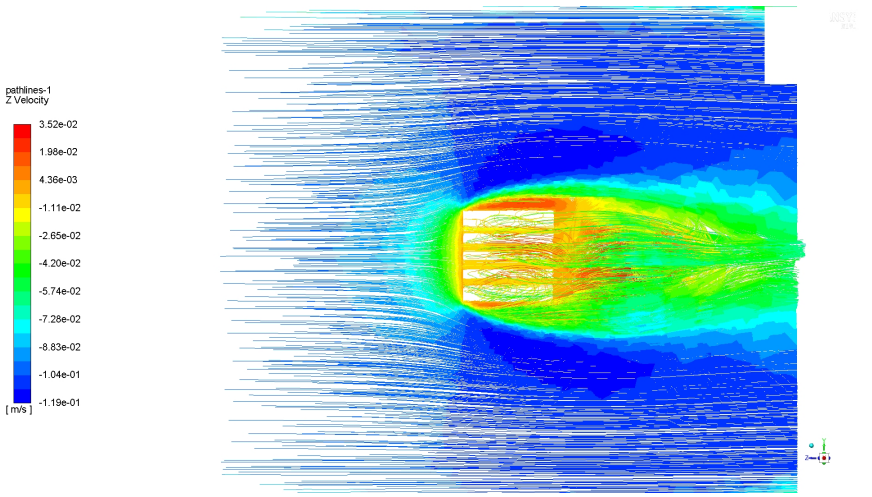

(a)

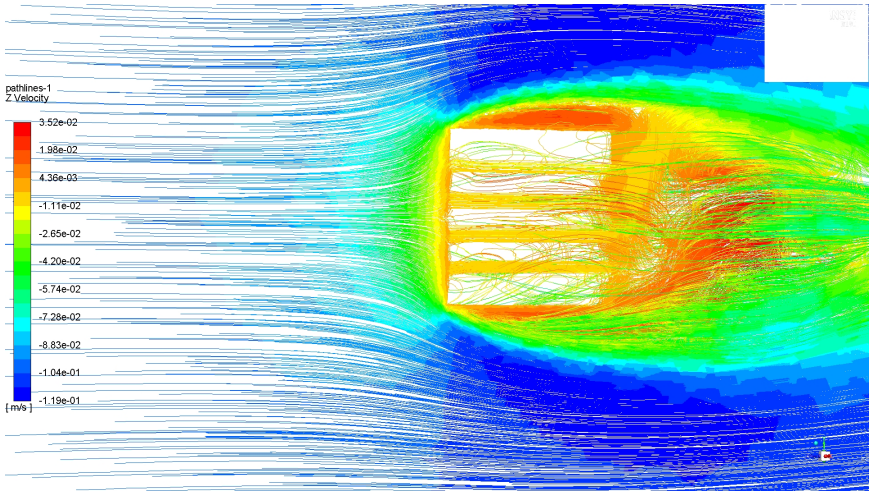

(b)

Figure D.2: Velocity Profile of the Air Flow of 0.1 m/s in the Cube with Pipes Model as Obtained from ANSYS Fluent.

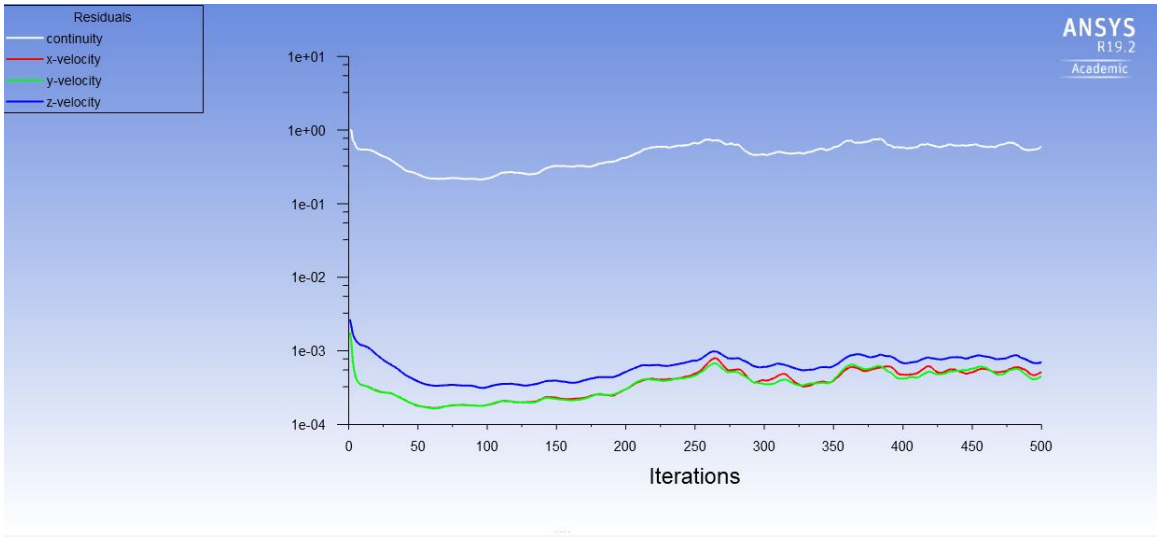

Figure D.3: Continuity and Velocity Convergence Curves for Cube with Pipes Model for a Velocity of 0.3 m/s and Air as Fluid, as Obtained from ANSYS Fluent.

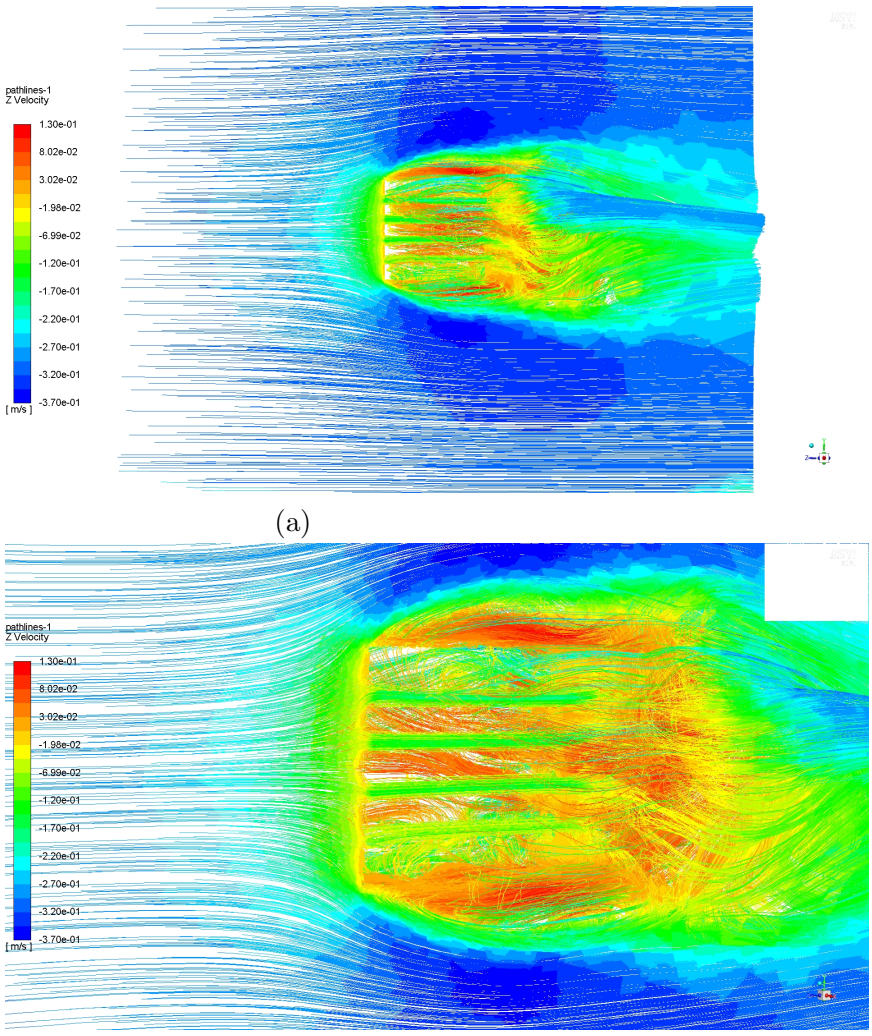

Figure D.4: Velocity Profile of the Air Flow of 0.3 m/s in the Cube with Pipes Model as Obtained from ANSYS Fluent.

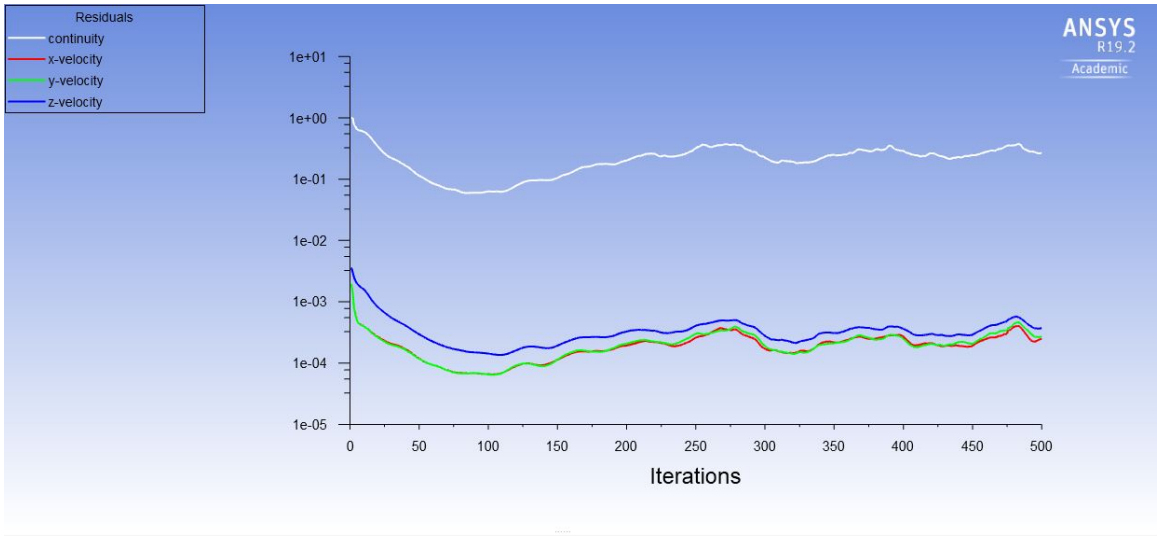

Figure D.5: Continuity and Velocity Convergence Curves for Cube with Pipes Model for a Velocity of 0.01 m/s and Water as Fluid, as Obtained from ANSYS Fluent.

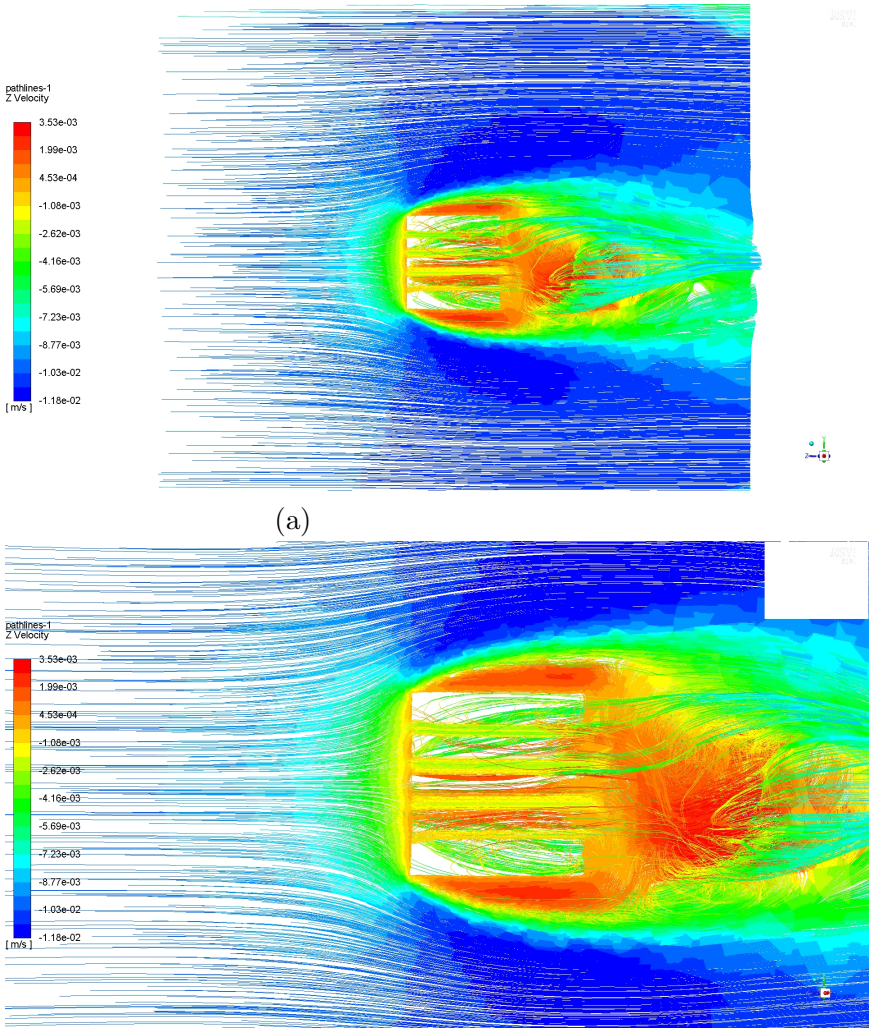

(a)

(b)

Figure D.6: Velocity Profile of the Water Flow of 0.01 m/s in the Cube with Pipes Model as Obtained from ANSYS Fluent.

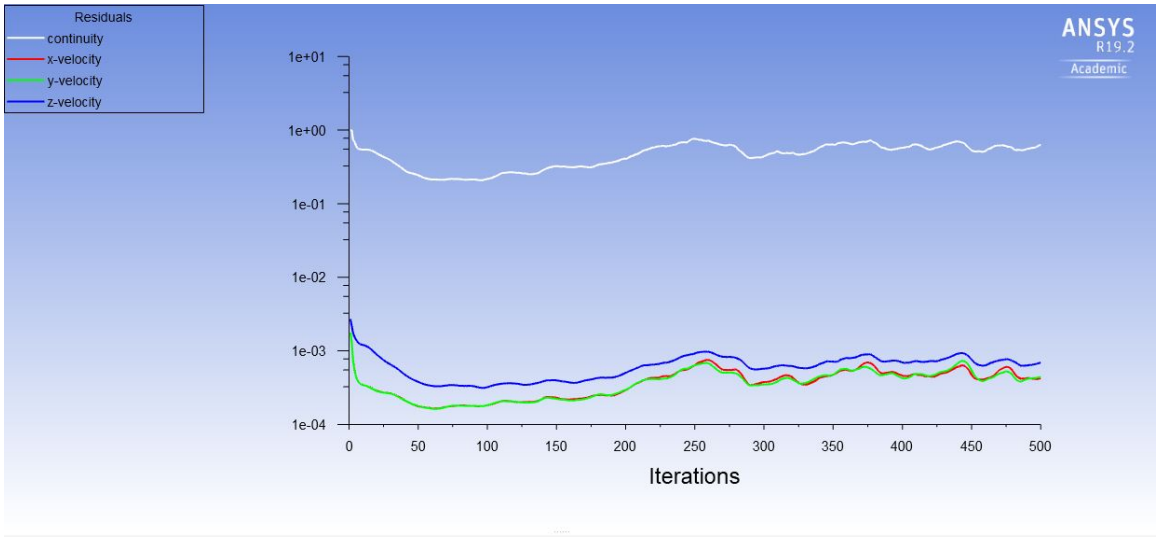

Figure D.7: Continuity and Velocity Convergence Curves for Cube with Pipes Model for a Velocity of 0.02 m/s and Water as Fluid, as Obtained from ANSYS Fluent.

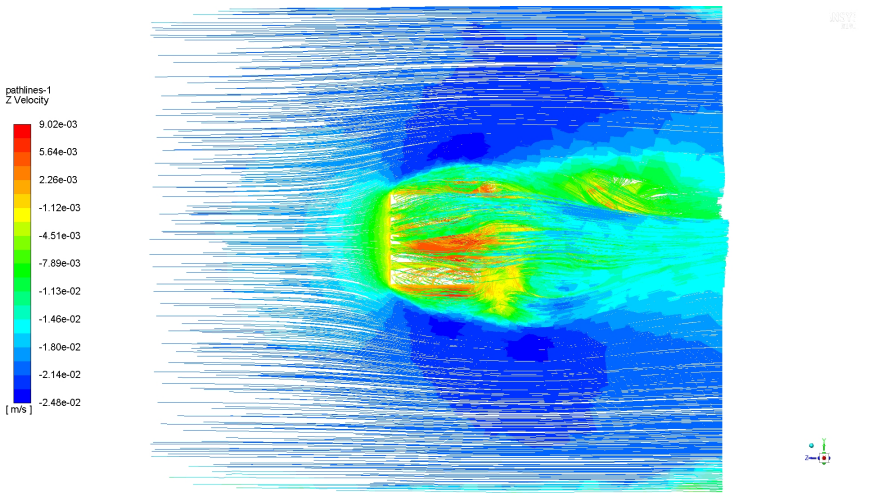

(a)

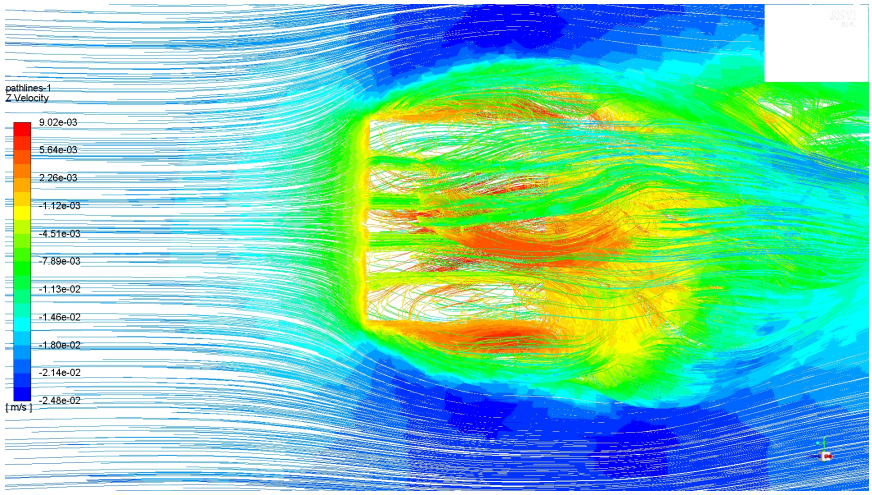

(b)

Figure D.8: Velocity Profile of the Water Flow of 0.02 m/s in the Cube with Pipes Model as Obtained from ANSYS Fluent.

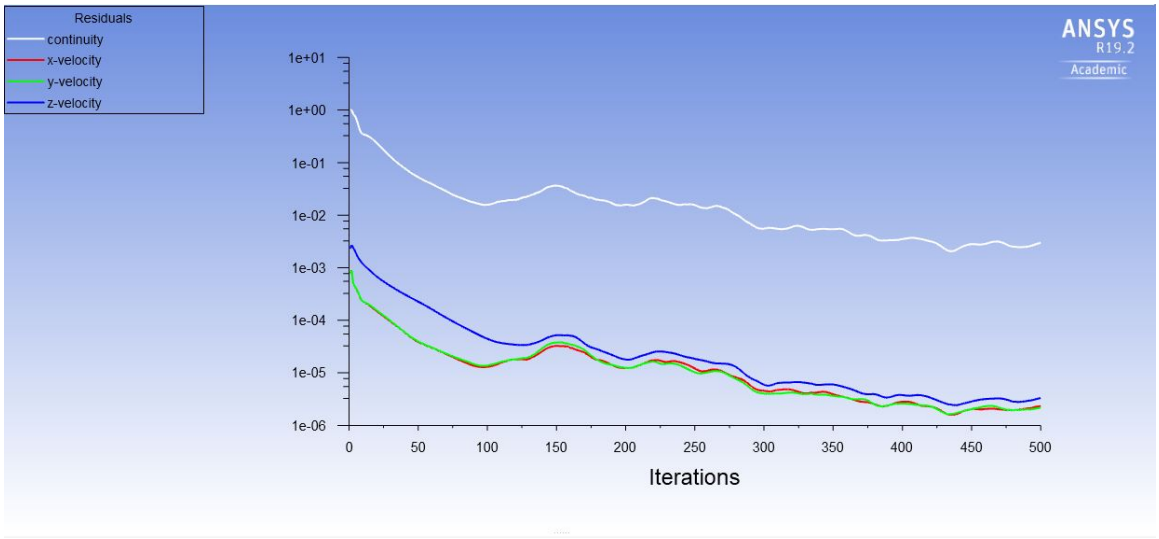

Figure D.9: Continuity and Velocity Convergence Curves for Spherical Gyroid TPMS Model for a Velocity of 0.1 m/s and Air as Fluid, as Obtained from ANSYS Fluent.

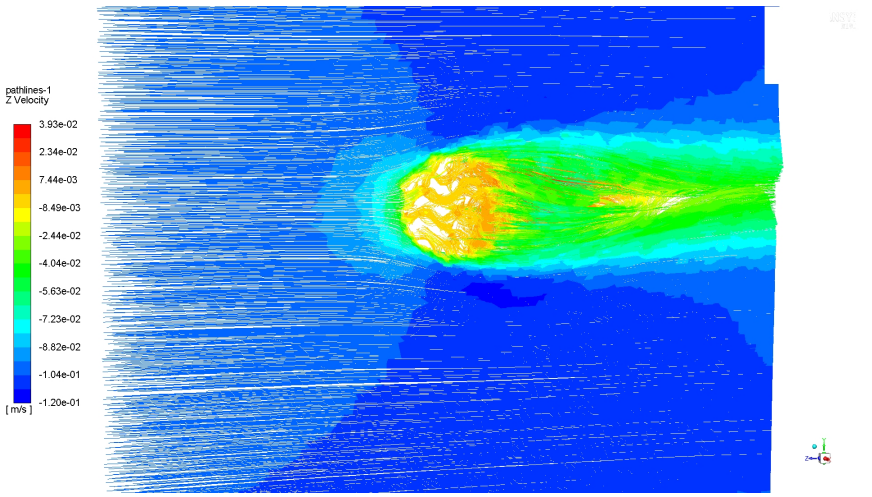

(a)

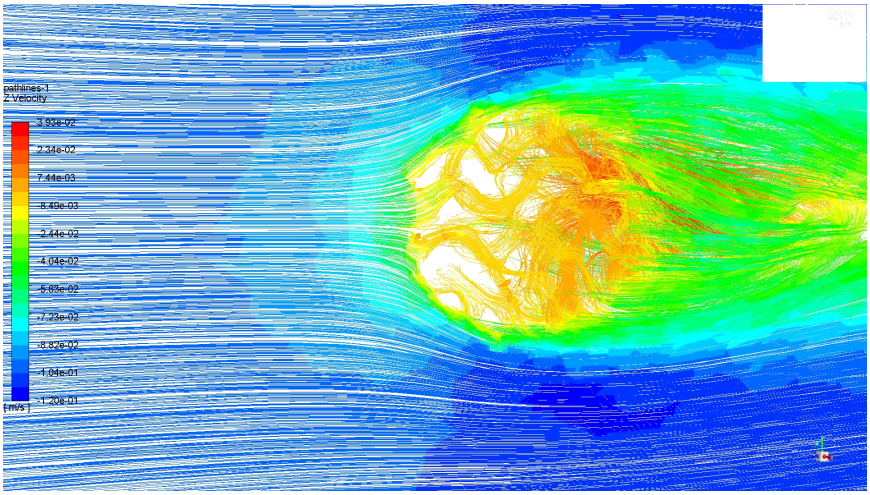

(b)

Figure D.10: Velocity Profile of the Air Flow of 0.1 m/s in the Spherical Gyroid TPMS Model as Obtained from ANSYS Fluent.

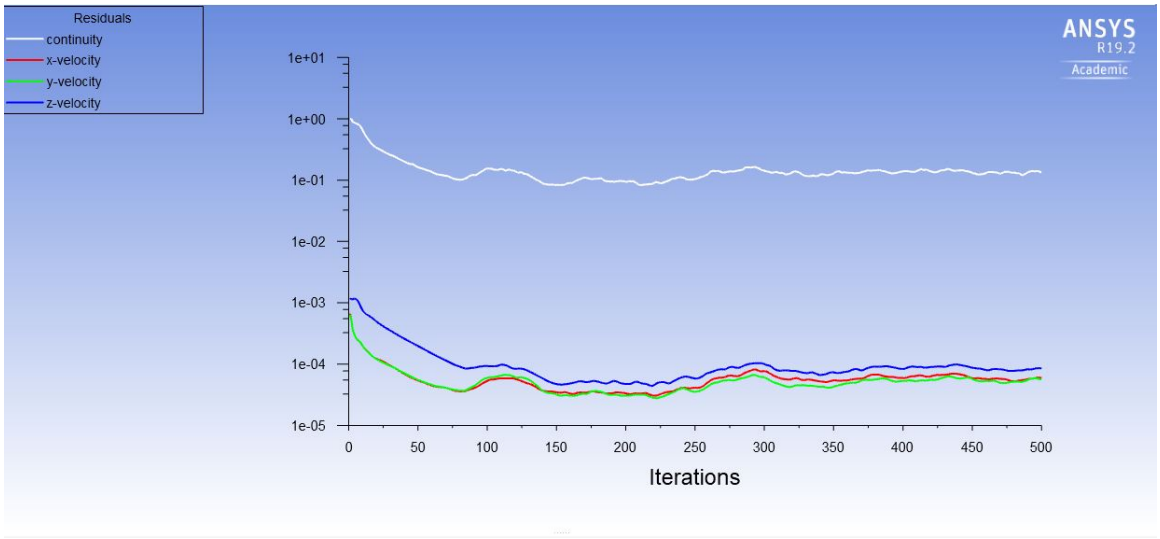

Figure D.11: Continuity and Velocity Convergence Curves for Spherical Gyroid TPMS Model for a Velocity of 0.3 m/s and Air as Fluid, as Obtained from ANSYS Fluent.

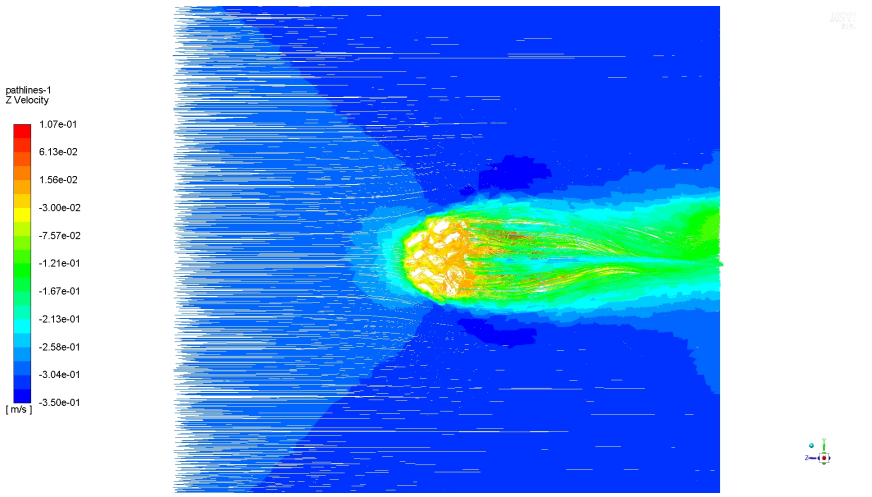

(a)

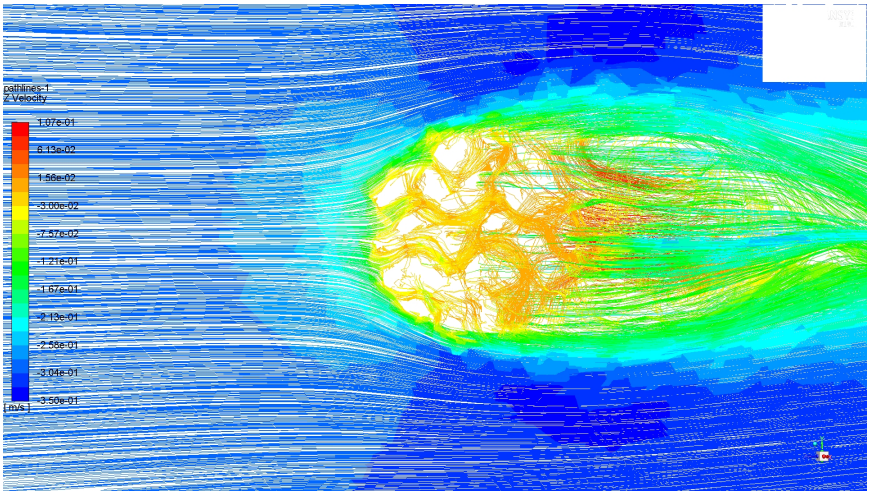

(b)

Figure D.12: Velocity Profile of the Air Flow of 0.3 m/s in the Spherical Gyroid TPMS Model as Obtained from ANSYS Fluent.

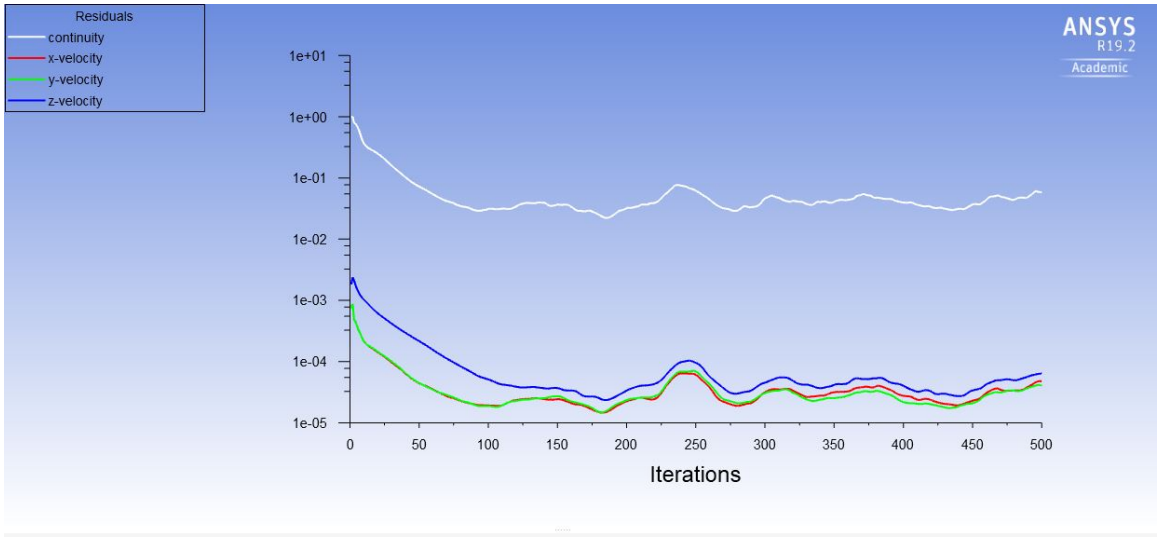

Figure D.13: Continuity and Velocity Convergence Curves for Spherical Gyroid TPMS Model for a Velocity of 0.01 m/s and Water as Fluid, as Obtained from ANSYS Fluent.

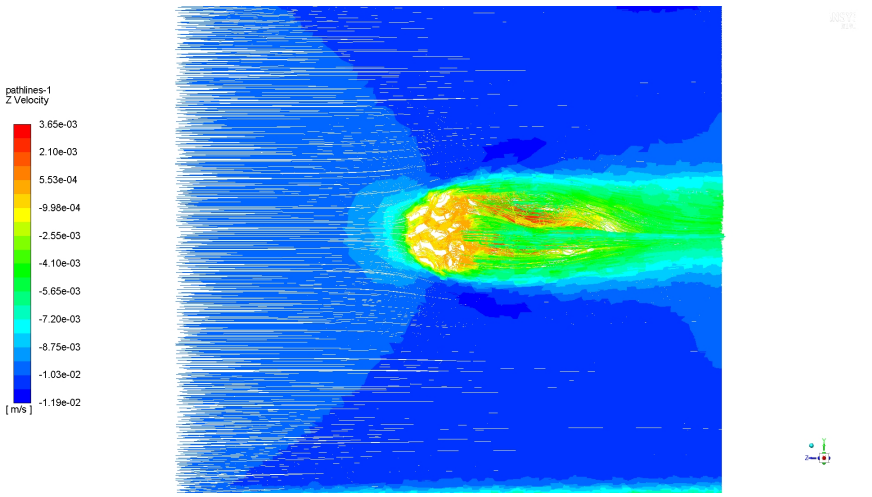

(a)

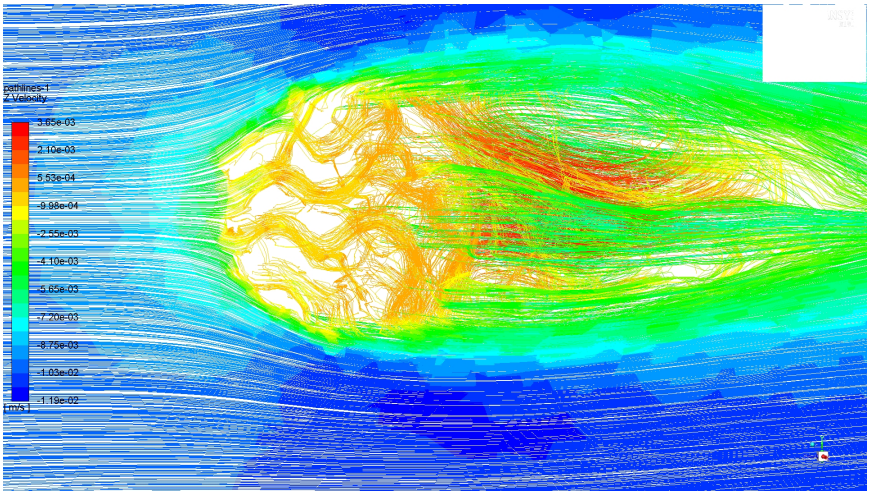

(b)

Figure D.14: Velocity Profile of the Water Flow of 0.01 m/s in the Spherical Gyroid TPMS Model as Obtained from ANSYS Fluent.

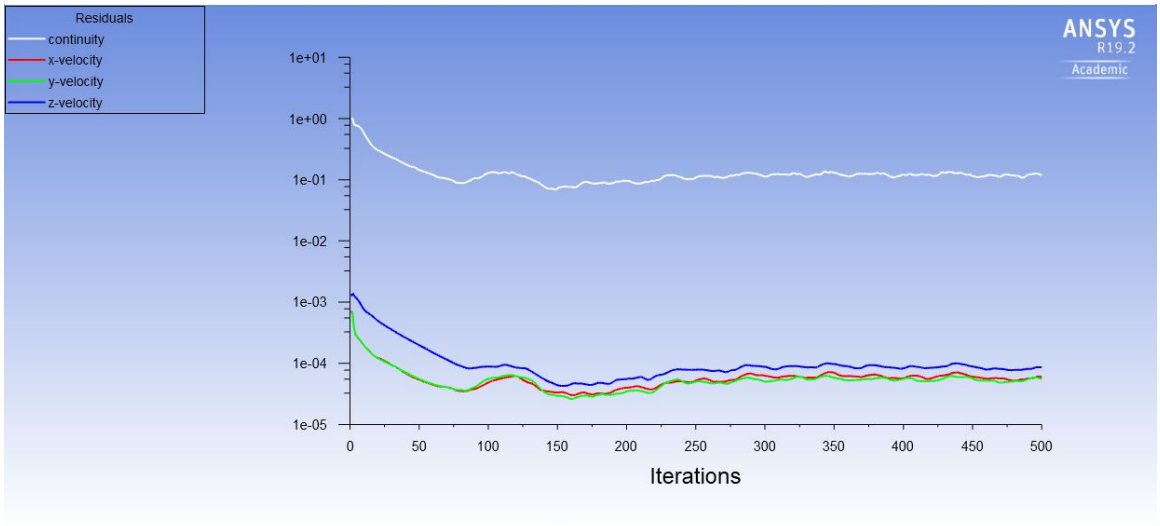

Figure D.15: Continuity and Velocity Convergence Curves for Spherical Gyroid TPMS Model for a Velocity of 0.02 m/s and Water as Fluid, as Obtained from ANSYS Fluent.

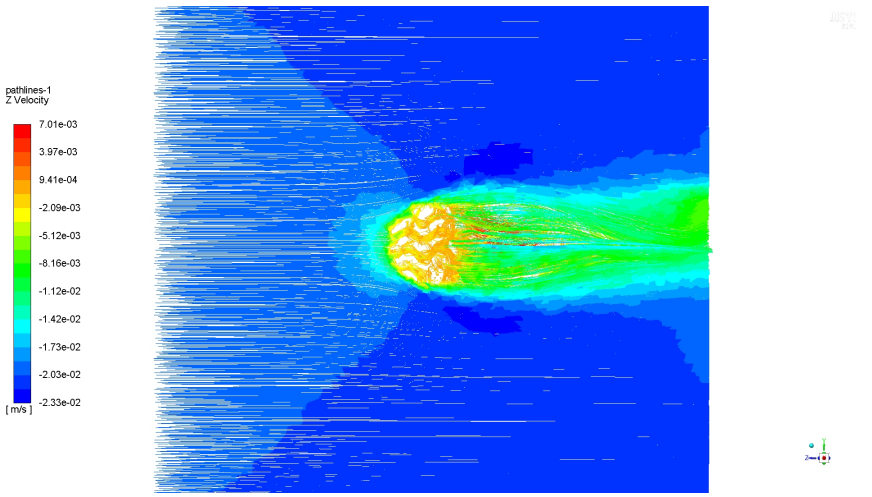

(a)

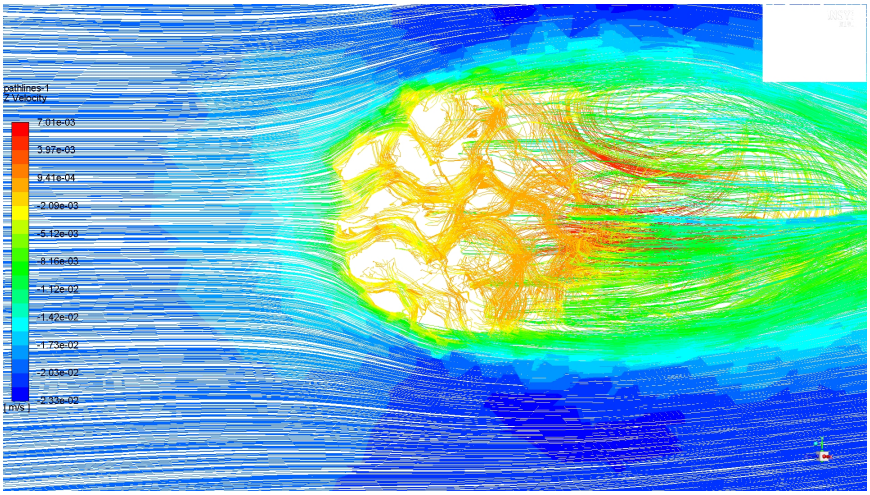

(b)

Figure D.16: Velocity Profile of the Water Flow of 0.02 m/s in the Spherical Gyroid TPMS Model as Obtained from ANSYS Fluent.